

Sand transport over a coarse and immobile bed

by

Paul E. Grams

A dissertation submitted to Johns Hopkins University in conformity with
the requirements for the degree of Doctor of Philosophy

Baltimore, Maryland

January 2006

ABSTRACT

Coarse-bedded rivers are often partially covered by fine sediment that occurs in patches or interstitial spaces. A series of flume experiments were conducted to develop and test a formulation for sand entrainment from a bed of coarse immobile grains. One set of experiments was conducted in equilibrium transport and a second set with a non-uniform transport field that resulted in spatially and temporally variable concentration profiles and sand-bed elevations. Both sets of experiments involved immobile grains much larger than the sediment in transport and bed shear stress, scaled by the grain size of the transported sediment, was consistent with transport in suspension. The experiments included different combinations of flow, sediment feed, and mobile sediment grain size.

Sand on a bed partially covered with fine sediment organizes into a predictable sequence of bed configurations. As the volume of fine sediment increases, there is a transition from sand stripes to barchan dunes to dunes. The transition between sand stripes and barchans is also a function of the near-bed hydraulic regime and can be captured in a bed state stability diagram based on the volume of mobile sediment and the boundary Reynolds number.

The equilibrium experiments produced partially sand-covered beds for a narrow range of sediment supply and flow combinations. The observations were used to develop a sand-elevation correction function that relates the entrainment rate for a bed partially covered with sand to the entrainment rate for a fully sand-covered bed. The experiments conducted under conditions of nonuniform transport were used to test the sand elevation correction function implemented in a numerical sand routing model that predicts profiles of suspended sediment concentration, the evolution of bed sediment storage, and bed sediment grain size. The sand-elevation correction function is shown to produce model output that is in good agreement with the experimental observations. These results indicate that while spatially-averaged entrainment from a bed with partial sand cover is less than the rate from a completely sand-covered bed, the local rate of entrainment must

exceed the expected sand-bed entrainment rate over a range of sand-bed elevations less than the height of the immobile grains.

Advisor: Peter R. Wilcock

ACKNOWLEDGEMENTS

This work was supported by funding from the U.S. Geological Survey's Grand Canyon Monitoring and Research Center. Additional financial and logistical support for the laboratory experiments was provided by the St. Anthony Falls Laboratory of the University of Minnesota and the STC program of the National Science Foundation via the National Center for Earth-surface Dynamics under the agreement Number EAR-0120914.

Many individual contributed to the success of this research. My advisor, Peter Wilcock, provided valuable ideas, advice, and encouragement. I also thank Reds Wolman for providing inspiration and many helpful suggestions. I would also like to thank Jack Schmidt for his interest and support in this work. The laboratory experiments would not have been at all possible without the very generous and capable help of the staff and students at the St. Anthony Falls Laboratory. Assistance with working out the details of numerical modeling was kindly given by Gilberto Urroz and James Powell of Utah State University. Finally, I thank my wife, Jill, and my two children, Clara and Tucker, for their support, encouragement, and just being here.

TABLE OF CONTENTS

| | |
|--|------|
| Abstract..... | ii |
| Acknowledgements..... | iv |
| Table of contents..... | v |
| List of Tables | viii |
| List of Figures..... | ix |
| List of Symbols used in the text..... | xii |
| Chapter 1: Introduction..... | 1 |
| Chapter 2: Entrainment of fine sediment into suspension over coarse immobile bed material in conditions of equilibrium transport..... | 4 |
| Introduction..... | 4 |
| Theoretical background | 4 |
| Entrainment from a sandy bed | 4 |
| Entrainment from an immobile coarse bed..... | 7 |
| Experimental Design and Methods..... | 8 |
| Results..... | 13 |
| Observations on the formation of a sediment bed | 13 |
| Flow structure and characterization of bed stress..... | 17 |
| Vertical distribution of suspended sediment and determination of the reference elevation | 26 |
| Sand elevation correction function | 28 |
| Conclusions..... | 32 |
| Chapter 3: Observations of evolving bed configuration under conditions of non- uniform transport of suspended sediment over a coarse immobile substrate | 34 |
| Introduction..... | 34 |
| Methods | 36 |

| | |
|---|----|
| Experimental design..... | 36 |
| Measurement of flow | 40 |
| Measurement of bed topography and grain size | 44 |
| Measurement of suspended sediment | 49 |
| Results..... | 50 |
| Description of bed configuration | 50 |
| Prediction of bed state..... | 55 |
| Bed sediment mixing depth | 60 |
| Sediment transport field..... | 63 |
| Predicting the distribution of sand patches | 66 |
| Conclusions..... | 72 |
| Chapter 4: Entrainment and non-uniform transport of sand in coarse-bedded rivers: Laboratory experiments and numerical model | 74 |
| Introduction..... | 74 |
| Background..... | 74 |
| Controls on sand entrainment in a coarse-bedded river..... | 77 |
| Measuring non-uniform sand transport over a coarse bed..... | 81 |
| Experimental design..... | 81 |
| Data collection | 82 |
| Experimental results..... | 85 |
| Non-Uniform Sand routing Model | 87 |
| Characterization of streamflow and bed stress | 87 |
| Entrainment from a sand bed | 91 |
| Sand elevation correction function | 91 |
| Sand transport and bed sediment continuity | 94 |
| Computational procedure..... | 95 |

| | |
|--|-----|
| Comparison of numerical predictions and experimental observations | 97 |
| Coupling local and spatially-averaged sand entrainment | 117 |
| Conclusions..... | 130 |
| References..... | 132 |
| Appendices..... | 136 |
| Appendix A. Collection and Processing of Acoustic-Doppler Velocimeter Data from the Tilting Bed Experiments | 136 |
| Appendix B. Collection and Processing of Acoustic-Doppler Velocimeter Data from the Main Channel Experiments..... | 138 |
| Appendix C. Bed Material Size Data from the Main Channel Experiments..... | 145 |
| Appendix D. Suspended Sediment Size Data from the Main Channel Experiments | 146 |
| Appendix E. Sampling of Suspended Sediment in Main Channel Experiments | 147 |
| Appendix F. Profiles of Bed Topography from Main Channel Experiments..... | 152 |
| Vita..... | 163 |

Note: In this copy, data tables included in Appendices C, D, and E have been omitted. These tables may be viewed in the original, on file at Johns Hopkins University. Electronic copies are included on the CD which should accompany this copy. Electronic copies are also available from the author, upon request. As a result, this version has fewer pages. The original version has 193 pages. This does not affect pages in the body and this copy is otherwise identical.

LIST OF TABLES

| | | |
|------------|---|----|
| Table 2.1 | Flume run characteristics and final bed condition. | 11 |
| Table 3.1. | Rouse number R and Froude number Fr associated with the two flow velocities used in the Main Channel experiments..... | 38 |
| Table 3.2. | Summary characteristics of experimental runs. | 39 |

LIST OF FIGURES

| | | |
|-------------|--|----|
| Figure 2.1 | Sketch of the 14-m “tilting-bed” flume at St. Anthony Falls Laboratory | 9 |
| Figure 2.2 | Size distribution of feed sediments..... | 10 |
| Figure 2.3 | Photographs showing post-run bed conditions | 14 |
| Figure 2.4 | Plot of sediment feed rate and flow rate | 16 |
| Figure 2.5 | Profiles for mean streamwise velocity | 18 |
| Figure 2.6 | Velocity defect representation of the velocity profile..... | 19 |
| Figure 2.7 | Profiles of normalized mean streamwise velocity | 20 |
| Figure 2.8 | Profiles of normalized shear velocity | 21 |
| Figure 2.9 | Comparison of total average boundary shear stress estimated using the shallow water equation to the total average boundary shear stress calculated by applying the sidewall correction procedure to the bed stress determined from the near-bed Reynolds stresses..... | 23 |
| Figure 2.10 | Measured and modeled profiles of sediment concentration | 27 |
| Figure 2.11 | The near-bed sand concentration predicted by the Garcia and Parker (1991) entrainment model and the observed concentrations | 29 |
| Figure 2.12 | The sand elevation correction | 30 |
| Figure 2.13 | Comparison of sand entrainment rate predicted with the sand elevation correction and without the correction compared to observed near-bed sand concentrations..... | 31 |
| Figure 3.1 | Gravel bar exposed at low flow on the Colorado River in Grand Canyon..... | 35 |
| Figure 3.2 | Size distribution of feed sediment and sediment used for initial bed cover..... | 37 |
| Figure 3.3 | Photograph looking upstream at the 40 m test section in the Main Channel at St. Anthony Falls | 38 |

| | | |
|-------------|---|----|
| Figure 3.4 | Plot showing normalized shear velocity as function of normalized elevation above the bed..... | 42 |
| Figure 3.5 | Plot showing the normalized shear velocity computed at each of the 5 cross-channel and 10 downstream measurement locations. | 43 |
| Figure 3.6 | Photographs of bed at the conclusion of each run segment. | 45 |
| Figure 3.7 | Diagram showing locations for measurements of sand depth. | 49 |
| Figure 3.8 | Frequency distribution of sand bed elevations for each segment of each run..... | 51 |
| Figure 3.9 | Bed-state diagram showing the stability fields identified by Southard (1991)..... | 56 |
| Figure 3.10 | Bed-state stability diagram modeled after that proposed by Kleinhans et al. (2002)..... | 59 |
| Figure 3.11 | Proposed bed-state stability diagram. | 60 |
| Figure 3.12 | Mixing depth normalized by total sand depth as a function of time following the addition of colored sand at the conclusion of the feed segment of each run. | 61 |
| Figure 3.13 | Grain size variation in sediment cores..... | 62 |
| Figure 3.14 | Photographs of sediment cores from Run 4a and Run 4c..... | 63 |
| Figure 3.15 | Time series of suspended sediment concentrations measured by laser-diffraction instruments for Run 1. | 64 |
| Figure 3.16 | Comparison between the rate of transport in suspension as measured by the samples collected by siphon and the run segment-average rate of sediment transport as determined by bed-sediment mass balance | 65 |
| Figure 3.17 | Cross-channel variation in suspended sediment transport rates. | 66 |
| Figure 3.18 | Channel cross-section profile of measured sand bed elevations..... | 67 |
| Figure 3.19 | Sand bed elevation as a function of mean sand bed elevation..... | 69 |
| Figure 3.20 | Fraction of bed covered by sand patch as a function of the spatially-averaged sand bed elevation. | 71 |
| Figure 4.1 | View of the Colorado River in Grand Canyon. | 75 |

| | | |
|-------------|---|-----|
| Figure 4.2 | View of the bed of the Colorado River in Grand Canyon. | 76 |
| Figure 4.3 | Sand elevation correction function. | 79 |
| Figure 4.4 | ..Size distribution of feed sediment and sediment used for initial bed cover..... | 82 |
| Figure 4.5 | Photographs of bed at the conclusion of selected run segments..... | 86 |
| Figure 4.6 | Plot showing normalized shear velocity as function of normalized elevation above the bed..... | 88 |
| Figure 4.7 | Plot showing velocity normalized by the mean velocity as a function of the normalized elevation above the bed. | 89 |
| Figure 4.8 | Sand elevation correction functions tested in the numerical transport and routing model. | 93 |
| Figure 4.9 | Plots of observed and predicted sand bed elevations..... | 98 |
| Figure 4.10 | Plot of observed and predicted sand bed elevations at the end of each run segment..... | 104 |
| Figure 4.11 | Profiles of modeled and observed concentration of suspended sediment. | 107 |
| Figure 4.12 | Plots of observed and modeled median grain size of the bed..... | 112 |
| Figure 4.13 | Plots of the bed elevation density functions for each run segment..... | 119 |
| Figure 4.14 | Plots using data from each segment of Run 4 that were used to determine relations for each of the parameters in the modified beta distribution as a function of the sand bed elevation normalized by the bed sediment median diameter. | 124 |
| Figure 4.15 | The modeled density functions of sand bed elevation..... | 126 |
| Figure 4.16 | Plot showing SASEC-1, SASEC-2, and SASEC-3. | 127 |
| Figure 4.17 | Plot of LOSEC function..... | 128 |

LIST OF SYMBOLS USED IN THE TEXT

| | |
|-----------------|--|
| a | = reference elevation for suspended sediment concentration; |
| a_β | = coefficient in modified beta distribution; |
| A | = constant = 1.3×10^{-7} ; |
| A_b | = bed area; |
| A_d | = cross-sectional area of roughness element or bedform presented to flow; |
| A_s | = area of bed that is sand; |
| B | = width of channel; |
| b_β | = coefficient in modified beta distribution; |
| c_β | = coefficient in modified beta distribution; |
| c' | = instantaneous deviation from suspended sediment concentration; |
| C | = concentration of suspended sediment; |
| C_D | = drag coefficient; |
| c | = instantaneous concentration of suspended sediment; |
| c_a | = observed concentration of suspended sediment evaluated at bed elevation $z = a$; |
| \hat{c}_a | = predicted concentration of suspended sediment for a full sand bed evaluated at bed elevation $z = a$; |
| d_β | = coefficient in modified beta distribution; |
| D | = grain size; |
| D_b | = size of immobile bed material; |
| D_{50} | = median grain size; |
| D_j | = characteristic size of sediment in j th size range; |
| e | = exponential function; |
| E_{sA} | = spatially-averaged dimensionless entrainment rate; |
| E_{sL} | = local dimensionless entrainment rate; |
| $\hat{E}_{s,j}$ | = predicted dimensionless entrainment rate in j th size range for a full sand bed; |
| E_s | = dimensionless entrainment rate; |
| $E_{s,j}$ | = dimensionless entrainment rate for sediment in j th size range; |
| F_d | = drag force due to large bedforms; |
| F_{za} | = net upward flux of sediment near the bed; |
| Fr | = Froude number; |
| F_p | = fraction of bed sediment in sand patches; |
| F_b | = fraction of bed sediment in non- patches; |
| g | = gravitational acceleration; |
| h | = flow depth; |
| h' | = flow depth associated with skin friction; |
| j | = index for grain size fraction; |
| k | = von Karmen's constant; |
| K_z | = diffusion coefficient for suspended sediment; |

| | | |
|--------------|---|--|
| K_E | = | turbulent eddy viscosity; |
| k_s | = | Nikuradse equivalent grain roughness associated with total bed stress; |
| k'_s | = | Nikuradse equivalent grain roughness associated with skin friction; |
| L | = | length of bed, in streamwise direction; |
| m | = | power in similarity variable for nonuniform sediment = 0.2; |
| n | = | power in similarity variable = 0.6; |
| N | = | number of roughness elements per unit channel length; |
| P | = | wetted perimeter; |
| p_j | = | volume fraction of bed material in j th size range. |
| q_s | = | streamwise flux of suspended sediment; |
| \bar{q}_s | = | cross-section average streamwise flux of suspended sediment; |
| q_T | = | total streamwise sediment flux; |
| \mathbf{R} | = | Reynolds number; |
| $R_{p,j}$ | = | particle Reynolds number for sediment in j th size range; |
| R^* | = | boundary Reynolds number; |
| R_o | = | Rouse number; |
| R | = | hydraulic radius; |
| r_b | = | bed roughness height; |
| s | = | specific gravity of sediment; |
| S | = | water surface slope; |
| S_0 | = | bed slope; |
| U | = | mean velocity in channel; |
| u | = | instantaneous downstream velocity; |
| \bar{u} | = | time-average downstream velocity; |
| \bar{u}_s | = | time-average downstream velocity at the water surface; |
| u' | = | instantaneous deviation from mean downstream velocity; |
| u_* | = | shear velocity; |
| u_{*b} | = | near-bed shear velocity; |
| u'_* | = | skin friction shear velocity; |
| V_b | = | volume of sand per unit bed area in non-patches; |
| V_p | = | volume of sand per unit bed area in patches; |
| V_t | = | volume of sand per unit bed; |
| w_s | = | particle settling velocity; |
| $w_{s,j}$ | = | particle settling velocity for sediment in j th size range; |
| w | = | instantaneous vertical velocity; |
| \bar{w} | = | time-average vertical velocity; |
| w' | = | instantaneous deviation from mean vertical velocity; |
| x | = | downstream coordinate axis; |
| y | = | cross-stream coordinate axis; |
| z | = | vertical axis, normal to bed; |
| z_s | = | sand bed elevation; |

| | | |
|-------------------|---|--|
| z_m | = | maximum bed elevation for which the bed is divided into sand patches and non-patches; |
| \hat{z}_m | = | maximum bed elevation for which the bed is divided into sand patches and non-patches, non-dimensionalized by the bed roughness height; |
| \bar{z}_s | = | spatially-averaged sand bed elevation; |
| \bar{z}_b | = | mean elevation of sand in interstitial spaces; |
| \bar{z}_p | = | mean elevation of sand in sand patches; |
| \underline{z}_p | = | minimum elevation of sand in sand patches; |
| z_{sL} | = | local sand bed elevation; |
| \hat{z}_s | = | sand bed elevation normalized by bed roughness height r_b ; |
| \hat{z}_{sL} | = | local sand bed elevation normalized by bed roughness height r_b ; |
| $Z_{m,j}$ | = | similarity variable for sediment in j th size range; |
| Z^* | = | parameter in sand elevation correction function; |
| β | = | beta function; |
| β' | = | modified beta function; |
| γ | = | specific weight of water; |
| χ | = | sand bed elevation normalized by bed sediment median diameter; |
| ε | = | sand elevation correction function; |
| ε_A | = | spatially-averaged sand elevation correction function; |
| ε_L | = | local sand elevation correction function; |
| ϕ | = | $-\log_2 D$ |
| η | = | power in sand elevation correction function; |
| λ | = | straining parameter; |
| λ_p | = | porosity of bed sediment; |
| ν | = | kinematic viscosity; |
| ρ | = | density of water; |
| σ | = | parameter in model for predicting the fraction of bed covered by sand patches; |
| τ_{zx} | = | turbulent Reynolds stress; |
| τ | = | shear stress; |
| τ_b | = | bed component of boundary shear stress; |
| τ_w | = | wall component of boundary shear stress |
| τ_0 | = | average boundary shear stress; |
| τ' | = | grain stress; |
| τ^* | = | dimensionless grain stress; |
| ω | = | parameter in model for predicting the fraction of bed covered by sand patches; |
| ξ | = | power in sand elevation correction function |

Chapter 1: Introduction

The annual sediment load of many rivers consists largely of sand and finer material that is transported over a coarse and immobile bed surface. During periods of abundant sediment supply, the coarse grains may be completely covered by fine sediment. As the supply decreases relative to the transport capacity of the system, parts of the underlying substrate become exposed and transport occurs over a bed that consists partially of fine sediment and partially of large immobile grains. This behavior has been observed in natural rivers (Kleinhans et al., 2002; Carling et al., 2000) and is a recognized feature of systems with limited supply of fine sediment (Rubin and Topping, 2001). Despite the widespread occurrence of this phenomena, very little research has been directed towards understanding the processes of sand transport over a bed of coarse, immobile grains and no general model has been developed.

Some outstanding examples of rivers with this characteristic can be found in the canyons of the western United States. The mainstem rivers of this region, such as the Snake River, the Green River, the Colorado River, and the San Juan River all transport large annual loads of fine sediment supplied primarily by large mainstem tributaries that drain areas of highly erodible sedimentary rocks (Howard and Dolan, 1981). Segments of these rivers flow through narrow canyons in which local channel morphology is dominated by debris fans that form at tributary junctions (Schmidt and Rubin, 1995; Grams and Schmidt, 1999). Debris fans are reworked by large mainstem floods and the coarse alluvium is redistributed to downstream gravel bars and the channel bottom (Webb et al., 1989; Larsen et al., 2004). The coincidence of abundant supplies of fine sediment and local supplies of coarse sediment results in a river channel with a coarse bed that is intermittently overlain by fine sediment. During extreme flow events that are capable of mobilizing the coarse fraction of the bed, most of the fine sediment is flushed downstream or deposited on the channel margins (Schmidt, 1999). However, during average flows that do not mobilize the coarse fraction of the bed, fine sediment is transported over the immobile bed, forming patches of fine sediment and partially filling interstitial spaces. Because many of these rivers are managed for water storage,

hydroelectric power generation, or flood control, flows that mobilize the coarse component of the bed are rare. Transport of fine sediment, then, occurs primarily during moderate flows when the bed framework is immobile (Topping et al., 2000).

Routing of fine-grained bed material (sand) through river systems is an important component in a wide range of geomorphic, engineering, and resource management applications. Herein, fine sediment is defined as the suspendable component of the bed material load, and is practically defined as sand in the size range from 0.062 mm to 2 mm. Fine sediments create and maintain important instream habitat for endangered native fish, form the substrate for riparian communities, and provide camping sites for recreationists. Methods currently in use for predicting the entrainment, transport, and routing of fine sediment were developed for conditions in which the bed and the transported material have the same size distribution. For fine-grained transport over a coarse, immobile bed, it is necessary to develop and test new analytical and modeling approaches. The goal of the research described here was to develop a predictive understanding of fine sediment entrainment over a bed of coarse immobile grains partially covered with mobile sediment.

The dissertation is organized into three main parts. Chapter 2 describes laboratory experiments on fine sediment transport over coarse immobile grains conducted under conditions of constant flow and sediment supply designed to produce equilibrium transport conditions. An important observation from these experiments was that a partially sand-covered bed could be maintained only for a narrow range of sediment supply and flow conditions. Outside this range, the bed was either devoid of sand or covered by migrating sand dunes. Coupled observations of near-bed suspended sand concentration and sand bed elevation were used to develop a model for the rate of sand entrainment from a partially covered bed. The model is formulated as a “sand-elevation correction” (SEC) function, in which the entrainment rate for a partial bed cover is scaled to the entrainment rate from a full sand bed.

Chapters 3 and 4 are based on a second set of laboratory experiments involving nonuniform transport of fine sediment over coarse immobile grains in a large

experimental channel. The bed configuration observed during periods of sediment accumulation and evacuation included flow-parallel sand stripes, flow-transverse barchan-like dunes, and conventional dunes on a sand-covered bed. Chapter 3 describes the bed configuration observed in these experiments and develops a bed state stability diagram based on the size of the mobile sediment and the thickness of the mobile layer relative to the size of the immobile grains. The fraction of the bed covered by sand bed forms is also shown to be a predictable function of the average thickness of the mobile sediment layer, a useful relation for sand routing.

The transport experiments conducted in the large channel are also used to test the sand entrainment formulation developed in Chapter 2. In Chapter 4, the entrainment formulation is implemented in a numerical sand routing model that predicts profiles of suspended sediment concentration, the evolution of bed sediment storage, and bed sediment grain size. A slightly modified version of the sand-elevation correction function is shown to produce model predictions in good agreement with the experimental observations. The basis of this modification is explored in terms of differences between local and spatially averaged entrainment and sand bed elevation.

Chapter 2: Entrainment of fine sediment into suspension over coarse immobile bed material in conditions of equilibrium transport

Introduction

The movement of fine-grained sediment through river systems is an essential component in a wide range of geomorphic, engineering, and resource management applications. For example, fine sediment transport and routing is applied in studies of watershed sedimentation (e.g. Trimble, 1997), fisheries management (e.g. Lisle and Lewis, 1992), and drainage basin evolution (e.g. Willgoose et al., 1990). Large fine sediment loads are not limited to alluvial rivers with sandy beds. In many gravel- and cobble-bedded rivers, much of the sediment load may consist of sand or finer material that is transported primarily in suspension. Indeed, fine-grained sediment comprises a significant component of the total transported load in most fluvial systems around the world (Meade et al., 1990). There is, therefore, a need for models that can be used to route fine-grained sediment over coarse beds that are largely immobile during extended periods of suspended sediment transport. Existing models for fine-sediment transport are typically developed for conditions in which the bed is uniformly composed of the same material that is in transport. When the bed sediment and the transported load are exclusively fine-grained, bedforms typically develop (Middleton and Southard, 1984) and several transport models are available which account for their effect on the flow and transport field (e.g. Engelund and Hansen, 1967; Smith and McLean, 1977; McLean et al., 1999). However, the dynamics of fine sediment entrainment from a coarse bed that is only partially covered by fine sediment are poorly understood and no modeling framework addresses this situation explicitly. The purposes of this paper are to describe laboratory experiments that were conducted to investigate fine sediment entrainment over a coarse bed and to propose an entrainment relation developed from those experiments.

Theoretical background

Entrainment from a sandy bed

The entrainment of sediment into suspension is a function of the fluid forces acting on the sediment and the sediment characteristics. A general functional relation for

sediment entrainment was proposed by Parker and Anderson (1977) based on dimensional analysis and expanded by Garcia and Parker (1991) to include sediment mixtures:

$$E_{s,j} = f\left(\frac{u'_*}{w_{s,j}}, \frac{h}{D_{50}}, R_{p,j}, \frac{D_j}{D_{50}}\right), \quad (2.1)$$

where E_s is a dimensionless sediment entrainment rate for the particle size fraction j , u'_* is the shear velocity associated with grain stress, $w_{s,j}$ is the particle settling velocity, h is the flow depth, D_{50} is the mean particle size for the sediment mixture, D_j is the sediment grain diameter, $R_{p,j}$ is the grain Reynolds number,

$$R_{p,j} = \frac{\sqrt{g(s-1)D_j} D_j}{\nu}, \quad (2.2)$$

$(s-1)$ is the submerged specific gravity of sediment, and ν is kinematic viscosity.

The net upward flux of suspended sediment near the bed F_{za} is the difference between erosion and deposition

$$F_{za} = \text{erosion} - \text{deposition}. \quad (2.3)$$

The volume rate of bed erosion rate per unit bed area per unit time is equivalent to the upward normal Reynolds flux of suspended sediment,

$$\text{erosion} = \overline{w'c'}, \quad (2.4)$$

where w is the instantaneous streamflow velocity normal to the bed and c is instantaneous sediment concentration. The overbar represents the time average quantity and the primes denote the instantaneous deviations from that average. The bed erosion rate is nondimensionalized by the particle settling velocity w_s , defining a dimensionless bed sediment entrainment rate,

$$E_s = \frac{\overline{w'c'}}{w_s}. \quad (2.5)$$

The volume rate of deposition per unit bed area per unit time is the product of the settling velocity and the near-bed sediment concentration

$$\text{deposition} = w_s \bar{c}_a, \quad (2.6)$$

where the \bar{c}_a denotes a near bed value for the time average concentration. Combining these expressions,

$$F_{za} = w_s (E_s - \bar{c}_a). \quad (2.7)$$

When transport is at equilibrium, there is no net normal flux of suspended sediment at the bed, erosion equals deposition, and $F_{za} = 0$. Thus,

$$E_s = \bar{c}_a. \quad (2.8)$$

This relation may be generalized for nonuniform sediment mixtures as

$$E_{s,j} = \frac{\bar{c}_{a,j}}{p_j}, \quad (2.9)$$

where the p_j is the volume fraction of bed material in the j th size range.

Because direct measurements of sand entrainment have been made only for limited conditions (Schmeeckle and Nelson, 2003), relations for sand entrainment depend on this theoretical equivalence of E_s with the near-bed suspended sediment concentration c_a under equilibrium transport conditions.

Garcia and Parker (1991) used field and laboratory data in which near-bed sediment concentrations had been measured under equilibrium transport to evaluate the relation given in equation (2.1). Based on these data, they proposed an entrainment relation of the form

$$E_{s,j} = \frac{A(\lambda Z_{m,j})^5}{1 + \frac{A}{0.3}(\lambda Z_{m,j})^5}, \quad (2.10)$$

where $Z_{m,j}$ is a similarity variable

$$Z_{m,j} = \frac{u'_*}{w_{s,j}} R_{p,j}^n \left(\frac{D_j}{D_{50}} \right)^m \quad (2.11)$$

and m and n are exponents chosen to minimize scatter when fitting the relation to laboratory and field data. The straining parameter λ is related to the standard deviation of

the grain size distribution. The similarity variable does not include the relative roughness h/D_{50} , which Garcia and Parker (1991) concluded was of secondary importance to flow strength and grain size in controlling entrainment rates. The data they had available, however, spanned only a limited range of h/D_{50} , thus the full range of possible effects of this parameter on entrainment are incompletely understood (Wright and Parker, 2004). While a formulation for fine-sediment entrainment from a coarse immobile bed should share basic characteristics with this relation, there are several reasons why it may perform poorly or require substantial modifications.

Entrainment from an immobile coarse bed

We propose that the functional relation described in equation (2.1) can be expanded for sand transport over a coarse, immobile bed by including a parameter that describes the relative elevation of the sand bed, such that

$$E_{s,j} = f\left(\frac{u'_*}{w_{s,j}}, \frac{h}{D_{50}}, R_{p,j}, \frac{D_j}{D_{50}}, \frac{z_s}{r_b}\right), \quad (2.12)$$

in which the additional parameter is the ratio of the sand cover thickness z_s to a characteristic roughness height r_b for the coarse grains on the bed.

Relative sand elevation can be argued to have both a positive and a negative effect on sand entrainment. One line of reasoning argues that entrainment rate should decrease in proportion to the area of the bed covered by sand. As the sand bed elevation drops and the proportion of the bed area covered by sand decreases, less sand is available for entrainment resulting in lower near-bed concentrations and lower total transport rates. This effect is analogous to the findings of Einstein and Chien (1953), who concluded that transport for a given grain size occurs in proportion to its abundance on the bed. This effect is included in the Garcia and Parker (1991) entrainment model in equation (2.9) provided p_j is understood to include all sediment on the bed, including immobile grains. By extension, one could infer that transport of the sand fraction of a coarse bed might occur in proportion to the abundance of sand among the bed roughness elements.

Sand entrainment may, however, also depend on the elevation of the sand bed relative to the elevation of the immobile grains. The large grains may exert a hiding effect whereby sand is hidden in interstitial spaces, causing reduced entrainment. This effect has been recognized for mixed size sediments in which the presence of grains of a given size alter the mobility of grains of differing sizes (Garcia and Parker, 1991). This effect could dampen entrainment rates below those predicted when the effects of the large particles are ignored.

Alternatively, the turbulent wakes shed by the large roughness elements may enhance local scour causing evacuation of the fine sediment when flow separation occurs over the roughness elements. Enhanced entrainment was observed in wind-tunnel experiments involving the emergence of large roughness elements in a deflating sand bed (Nickling and McKenna Neuman, 1995). They found elevated transport rates as roughness elements were initially exposed in the deflating surface. As the sand bed elevation continued to decrease, they reported a rapid transition from enhanced transport to extremely low transport rates. They argued that the elevated transport rates resulted from increased turbulence introduced by the emerging surface roughness and that the transition to low transport rates occurred when all of the bed stress was consumed by form drag on the bed roughness elements.

Experimental Design and Methods

The primary objective of the laboratory experiments described in this paper was to measure sand entrainment rates for different conditions of bed sand coverage over an immobile rough bed. The essential scaling properties for these objectives are those pertaining to the near-bed flow and sediment entrainment conditions. Thus, the critical components of the experimental design are (1) a large ratio between the size of sand in transport and the size of the immobile bed material, (2) suspended sediment concentrations similar to those that occur in natural conditions, and (3) a ratio between bed shear stress and particle settling velocity, expressed as the Rouse number,

$$R_o = \frac{w_s}{ku_*}, \quad (2.13)$$

that is comparable to those that occur in natural conditions. A further requirement for these experiments was near-equilibrium transport conditions such that measured values of c_a can be used to estimate E_s (Eq. 2.8).

The experiments were conducted in a 14-m flume at the St Anthony Falls Laboratory (Figure 2.1). Bed roughness was achieved by attaching 10-cm diameter hemispheres to the flume bed in a closest-packing arrangement. Although the immobile component of the bed in natural settings can be orders of magnitude larger, the ratio between this size and the fine component exceeds 800 and should be large enough that essential interactions between the two bed grain-size components are represented.

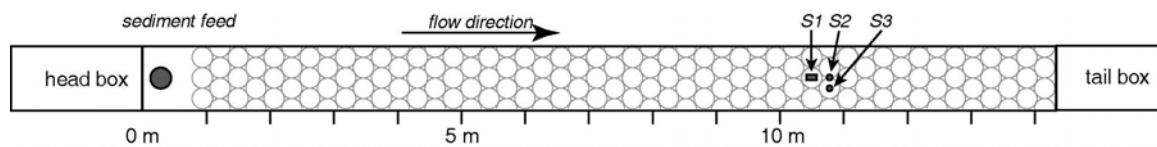


Figure 2.1. Sketch of the 14-m “tilting-bed” flume at St. Anthony Falls Laboratory showing configuration of the 10-cm diameter hemispheres installed as roughness elements. S1 is the suspended-sediment sampling station and ADV measurement location. S2 and S3 are additional ADV measurement locations.

Two sediment mixtures were used for the fine-sediment feed. The “fine” sediment was a natural grain quartz sand with a median diameter of approximately 0.13 mm (US Silica F110); the “coarse” sediment was a natural grain sand mixture with a median diameter of approximately 0.17 mm (Figure 2.2). These sizes are within the range of sand grain sizes that comprise the fine fraction of the bed-material load of many rivers.

The bed slope was set at 0.0002 with a flow depth of 40 cm (measured from the top of the hemispheres) such that the Rouse number was between about 0.5 and 0.7. This range of Rouse number is representative of conditions for which the majority of bed-material transport occurs in suspension. A 40-cm flow depth was chosen such that the flow would include both a spatially variable near-bed region and a spatially integrated region away from the bed. The resulting ratio of flow depth to grain size is roughly an order of magnitude smaller than occurs in the field. This distortion is likely to affect the

frequency and magnitude of the largest turbulent eddies that reach the near-bed region. The effect of those processes on sand entrainment should be secondary to the effects of flow separation and wake turbulence within the near bed region caused by the roughness elements. Measurements of velocity profiles indicated that the flow depth was sufficient to produce both a near-bed spatially variable layer and a thicker spatially averaged layer in the core of the flow. To keep the rate of sand feed to a manageable quantity, the flume was operated at a working width of 30 cm. Sediment concentrations were between 500 and 2500 mg/l.

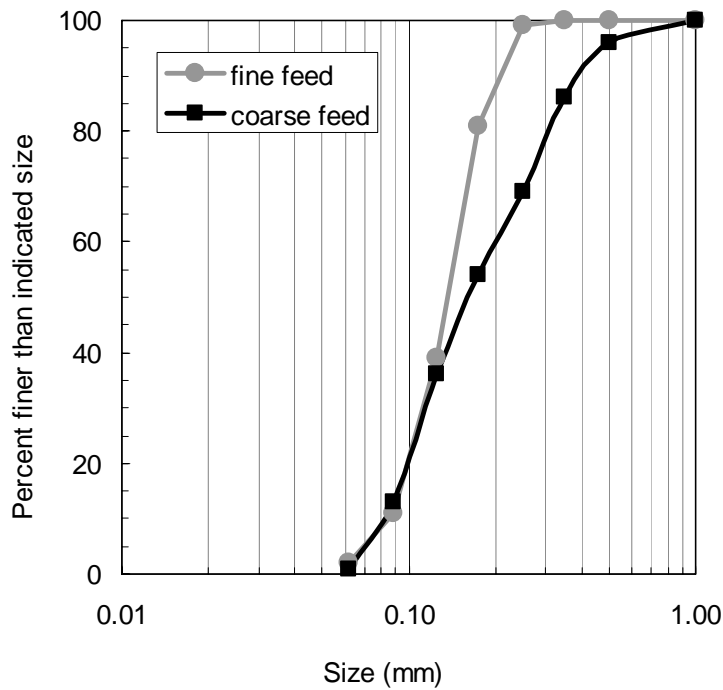


Figure 2.2. Size distribution of feed sediments.

Sediment was fed into the upstream end of the flume through a pipe that introduced the sediment near the bed to ensure rapid mixing. Constant sediment feed rates were maintained by an automated sediment feeder or by continuously pouring small containers of known volume at timed intervals. Water surface elevations were measured to monitor for uniform flow conditions.

For each sediment feed rate, a series of experimental runs was conducted using different flow rates to establish conditions producing a uniform sediment bed and transport field (Table 2.1). Each run was started with no sand on the bed and run durations were determined such that the total volume of sand fed exceeded the maximum available bed storage by a factor of three or greater. For the final 2 to 5 minutes of most runs, the sand feed was replaced with a colored sand feed of the same size in order to allow observations of sediment mixing within the bed.

Table 2.1 Flume run characteristics and final bed condition.

| Run | Q (l/s) | Q_s (g/s) | U (m/s) | Runtime (hr) | Fr | R_o | Feed | z_s^1 (cm) | Bed Condition |
|-----|--------------|----------------|--------------|-----------------|------|-------|--------|-----------------|-----------------------|
| 0 | 98 | 75 | 0.81 | 2.2 | 0.40 | 0.36 | fine | 0 | no sand cover |
| 6a | 97 | 200 | 0.80 | 0.8 | 0.40 | 0.37 | fine | 0 | no sand cover |
| 3 | 66 | 75 | 0.56 | 2.0 | 0.28 | 0.52 | fine | 0.9 | minimal sand cover |
| 14 | 66 | 41 | 0.55 | 2.5 | 0.28 | 0.53 | fine | 1.0 | minimal sand cover |
| 2 | 71 | 75 | 0.59 | 2.0 | 0.30 | 0.49 | fine | 1.0 | minimal sand cover |
| 13 | 71 | 43 | 0.59 | 2.2 | 0.30 | 0.49 | coarse | 1.6 | partial sand cover |
| 15 | 66 | 20 | 0.55 | 2.0 | 0.28 | 0.53 | coarse | 1.9 | partial sand cover |
| 16 | 79 | 46 | 0.66 | 3.0 | 0.33 | 0.44 | coarse | 2.2 | partial sand cover |
| 17 | 93 | 179 | 0.78 | 1.3 | 0.39 | 0.38 | coarse | 2.9 | partial sand cover |
| 6b | 92 | 200 | 0.76 | 1.1 | 0.38 | 0.39 | fine | 1.2 | partial sand cover |
| 8 | 60 | 33 | 0.50 | 2.5 | 0.26 | 0.58 | fine | 1.9 | partial sand cover |
| 12 | 60 | 75 | 0.50 | 1.3 | 0.25 | 0.58 | fine | 3.1 | partial sand cover |
| 7 | 53 | 33 | 0.45 | 2.5 | 0.23 | 0.64 | fine | 2.0 | aggrading-small dunes |
| 5 | 88 | 200 | 0.73 | 1.0 | 0.36 | 0.40 | fine | 2.0 | aggrading-small dunes |
| 1 | 53 | 75 | 0.45 | 2.1 | 0.23 | 0.64 | fine | 8.1 | aggrading-large dunes |
| 4 | 79 | 200 | 0.67 | 1.3 | 0.34 | 0.44 | fine | 9.4 | aggrading-large dunes |

¹ z_s is the mean elevation of sand in the bed at the conclusion of the run.

Samples of suspended sediment were collected at one sampling location 10.5 m downstream from the flume headbox. This location was chosen because it was well downstream from entry effects caused by flow exiting the headbox and the beginning of the rough bed at the head of the flume. Samples were drawn from the flow by a rake of stainless steel 3.18 mm i.d. Pitot tubes with nozzles positioned at elevations of 0.5, 2, 5, 10, and 30 cm above the hemisphere tops. Each Pitot tube was attached to a length of plastic tubing that carried the sample to a collection jar. Prior to sampling the suspended sediment, point velocities at each sampling location were measured with an acoustic Doppler velocimeter (ADV; SonTek 10-MHz). Velocity through the sampling tube was

adjusted to match that of the local flow by adjusting the elevation of the siphon tube outlet. Between one and five sets of suspended sediment samples were collected for each run and sample durations ranged from 30 to 60 s. A total of 294 suspended sediment samples were collected and analyzed to determine sand concentration. A subset of these samples, including the final sample for each run, was processed in a settling tube to determine the grain size distribution.

For each of the flow rates used in the experimental runs, a set of detailed velocity measurements was made with the ADV. Velocity profiles were measured directly over a hemisphere in the center of the channel at the sediment sampling location and on the right side of the channel one row downstream from the sampling location. A third profile was collected over the gap between two spheres one row downstream from the sediment sampling location (Figure 2.1). For one flow rate, centerline velocity profiles were collected at 1-m intervals along the length of the flume to test for flow uniformity and secondary flow patterns. Each profile consisted of seven velocity measurements made 0.5, 1, 2, 5, 10, 20, and 30 cm above the height of the hemisphere tops. Individual velocity measurements were collected at a 25 Hz sampling rate for a period of one minute. The ADV measured velocities in three orthogonal coordinates within a 0.2 cm^3 sample volume.

Following each run, the entire length of the hemisphere-covered bed was photographed from above in 0.5 m sections. The depth of sand was measured directly along the centerline and along each sidewall at 69 evenly spaced positions. The depth of colored sand mixing was determined by measuring the depth of colored sand occurrence at each of these locations for runs in which colored sand was used. Bed samples were collected at approximately 2-m intervals along the flume bed. Separate surface and sub-surface samples were collected where there was a difference in surface and sub-surface grain size or sediment color.

Results

Observations on the formation of a sediment bed

For each sediment feed rate, a partially sand covered bed could be developed and maintained over only a narrow range of flows. At discharges above this range, most of the sediment remained in suspension and very little or no sand bed developed (Figure 2.3a). At lower discharges, sediment accumulated on the bed and migrated downstream as a coherent dune (Figure 2.3b). Within the correct range of water discharge and sediment feed, sand accumulated in the hemisphere interstices, resulting in partial sand coverage but no dune formation (Figure 2.3c). This elevation was typically reached about midway during a run and maintained for the remainder of the run. However, even in the runs for which the mean sand bed elevation was less than the height of the hemispheres, the hemispheres could be buried locally (Figure 2.3c). The greatest sand depths were concentrated along the sidewalls, driven by reduced velocity and bed shear near the wall. Those experiments that resulted in a bed with some sediment retention but without continued aggradation and dune formation, were divided into runs with an average sand depth of 1 cm or less (minimal sand cover) and runs with an average sand depth of greater than 1 cm (partial sand cover). The runs without a stable sand bed were classified as either “dune-forming” or “evacuating” runs, depending on whether dunes formed or no sediment bed formed, respectively. Two of the dune forming runs resulted in large dunes that covered much of the flume bed and resulted in an average sand depth that exceeded the bed roughness height. Smaller dunes formed in the other two dune-forming runs and average sand depths were less than the bed roughness height.

Bed conditions with minimal or partial sand cover were achieved for six sediment feed-discharge combinations (Figure 2.4). For example, at the sediment feed rate of 75 g/s, there was one run in which the bed aggraded and formed large dunes. At slightly higher discharges, beds with partial and minimal sand cover were achieved. The transition from runs with an aggrading bed to runs with an evacuated bed is most narrowly defined for the runs conducted at a sediment feed rate of 200 g/s. This feed rate combined with a discharge of 92 l/s produced a partially sand covered bed. The slightly

higher discharge of 97 l/s resulted in an evacuated bed and the slightly lower discharge of 88 l/s caused a small dune to form. The even lower discharge of 79 l/s resulted in a large dune.



(a)



(b)



(c)

Figure 2.3. Photographs showing post-run bed condition for an evacuated bed (a), a bed partially covered with sand (b), and an aggrading bed with large dunes (c).

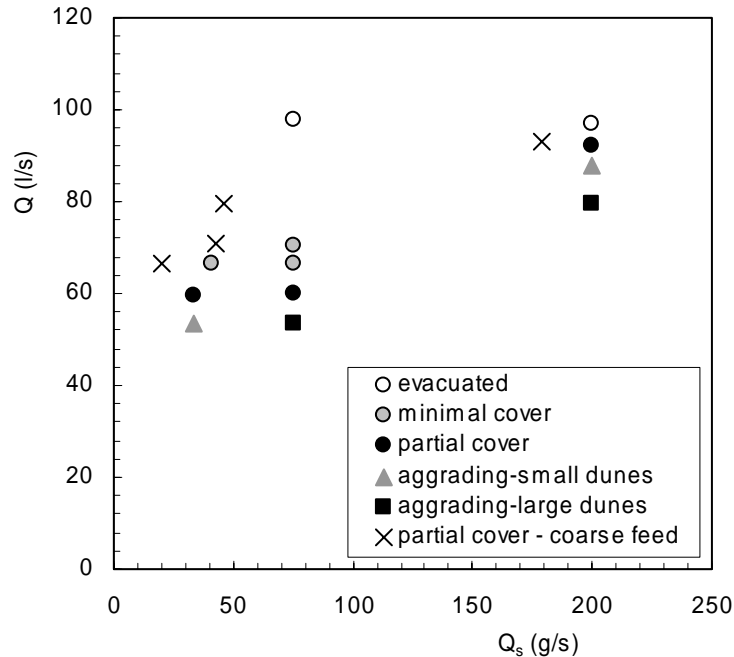


Figure 2.4. Plot of sediment feed rate (Q_s) and flow rate (Q) for uniform transport runs conducted in 2002. The dashed lines identify the narrow range of Q for which a given Q_s will produce a bed of partial sediment cover, which is one with deposition of sand among the sphere interstices, but without massive aggradation that forms migrating dunes. The coarse sediment feed requires a larger discharge to create partial sand cover.

These results suggest that a partially sand-covered bed may not be a stable condition and that the transition from full sand bed to a bed with low sand elevations can occur abruptly. The rapid transition from aggrading to evacuating conditions suggests that as the sand elevation drops below the tops of the roughness elements, entrainment rates must be maintained at or near the full sand bed rate or, perhaps, elevated. If entrainment rates declined rapidly as the bed roughness elements were exposed, the condition of partial sand cover should be more stable and we would observe a wider range discharge and feed rates that produced partial sand coverage. This interpretation is consistent with the observation by Nickling and McKenna Neuman (1995) of enhanced entrainment as roughness elements became exposed in aeolian transport. Because inter-grain collisions are less important in accelerating entrainment in water than in air, we would expect to have a smaller degree of enhanced entrainment than observed by Nickling and McKenna Neuman (1995). Because we do not have paired instantaneous

measurements of the sand entrainment rate and the local sand bed elevation, we can only conclude that entrainment rates do not drop significantly as the sand bed elevation drops.

Flow structure and characterization of bed stress

Because sand entrainment is a strongly non-linear function of bed stress, the method for estimating bed stress is a critical component of any transport model. For these experiments the bed slope and the average depth were essentially the same for each run, and most of the hydraulic adjustment over the 50% variation in discharge occurred in mean velocity (Table 2.1). This, however, resulted in slightly non-uniform flow conditions. Thus, it is not possible to estimate average boundary shear stress τ_o from the depth-slope product,

$$\tau_o = \gamma h S, \quad (2.14)$$

where γ is the specific weight of water, h is the flow depth, and S is the water surface slope. We, therefore, estimated bed stress from (1) near-bed velocity measurements and (2) the shallow-water equation applied with measured water surface elevations.

The raw ADV data were processed to remove spikes and correct for instrument small variations in instrument alignment (Appendix A). Mean velocities and turbulence statistics were calculated from the filtered and rotated data. The turbulent Reynolds stress τ_{zx} was calculated at each elevation in the flow as

$$\tau_{zx}(z) = -\rho \overline{(u'w')}, \quad (2.15)$$

where z represents height above the bed, ρ is the fluid density, u and w are the streamwise and vertical components of velocity, taken positive in the downstream and upward directions, the overbar represents time-averaged quantities and the primes denote instantaneous deviations from the mean (i.e. $u' = u - \bar{u}$). The corresponding shear velocity u_* was calculated as

$$u_*(z) = \sqrt{\tau_{zx} / \rho}. \quad (2.16)$$

Measurements made at 1 m intervals along the length of the flume show the development of the rough flow profile and indicate that fully developed flow conditions

existed at distances of 8 to 11 m downstream from the flume headbox (Figure 2.5). The development of the velocity profile is also shown by an examination of the velocity defect profile, calculated as

$$\frac{(\bar{u}_s - \bar{u})}{u_*}, \quad (2.17)$$

where \bar{u}_s is the surface velocity, taken as the measured velocity 30 cm above the hemisphere tops. The velocity defect profile for the sediment measurement station (10.6 m downstream from the entrance) is shown in Figure 2.6. The measured velocities fit a logarithmic velocity-defect distribution down to 2 cm above the bed, further indicating fully developed flow.

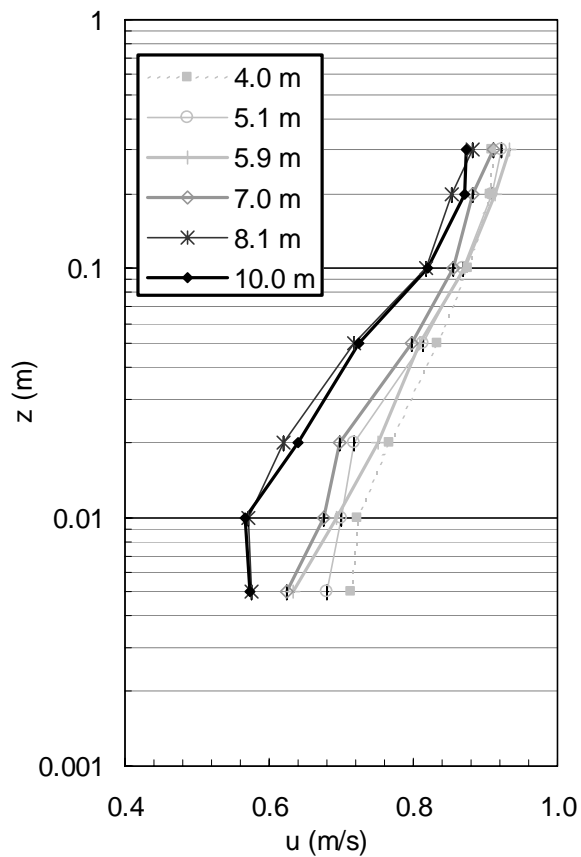


Figure 2.5. Profiles for mean streamwise velocity from 4.0 to 10.0 m downstream from flume headbox.

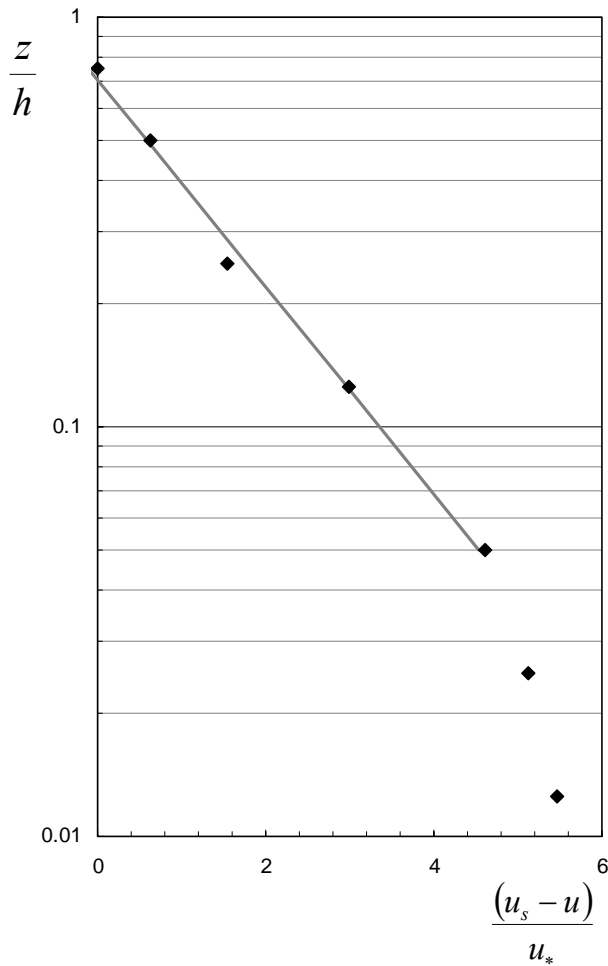


Figure 2.6. Velocity defect representation of the velocity profile.

The velocity profiles collected in the vicinity of the sediment sampling station indicate that there existed a vertically mixed region of the flow in the first 2 cm above the hemispheres (Figure 2.7). From 0.5 to 2 cm above the hemispheres, velocities are constant within the range of uncertainty in the measurements. Between 2 cm and 30 cm above the roughness elements, velocity increases in a log-linear relationship. The variation of u_*/u from 0.5 to 2 cm above the hemispheres is not correlated with either the magnitude of the mean flow velocity or the measurement position. The mean u_*/u is similar among the three different measurement stations (Figure 2.8). These data suggest that shear stress near the bed can be represented as a simple function of mean velocity

$$u_{*b} = 0.07U, \quad (2.18)$$

where u_{*b} represents the near-bed shear velocity. Analysis of the residuals of the predicted estimates of u_{*b} compared to the measured values of u_* at 0.5, 1.0 and 2.0 cm indicate a root-mean-square error of 0.01. The error is approximately the same among the different measurement positions and elevations.

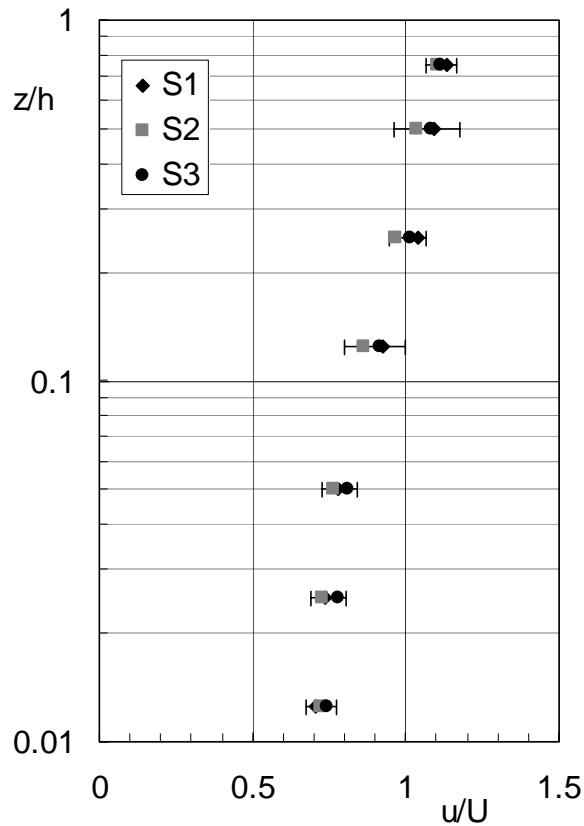


Figure 2.7. Profiles of normalized mean streamwise velocity for each of the three measurement stations near the sampling station. The location of the measurement stations is indicated in Figure 2.2. The error bars show +/- one standard deviation about the mean for all measurement stations.

Non-uniform flow conditions at the flume entrance and exit caused measurable variations in depth at the upstream and downstream ends of the flume compared to the depths in the region from 4 to 12 m downstream from the headbox. At 3 m downstream, depths were up to 1 cm greater than the average depth in the center region and at 13.6 m downstream, depths were up to 0.7 cm greater than the average depth in the center region.

To estimate the effect of non-uniformity on our modeled bed stress u_{*b} , we estimated the non-uniform flow total boundary shear stress $\tau_0(N)$ using the shallow water equation

$$\tau_0(N) = \rho g R \left[S_0 - \frac{dh}{dx} - \frac{U}{g} \frac{du}{dx} \right], \quad (2.19)$$

where S_0 is the slope of the flume bed. The hydraulic radius R and local velocity u were calculated from the measured depths. The section mean velocity U was calculated as the average of each two adjacent local velocities. The gradients in depth and velocity were determined by backward differences from each measurement position, starting with the second station downstream.

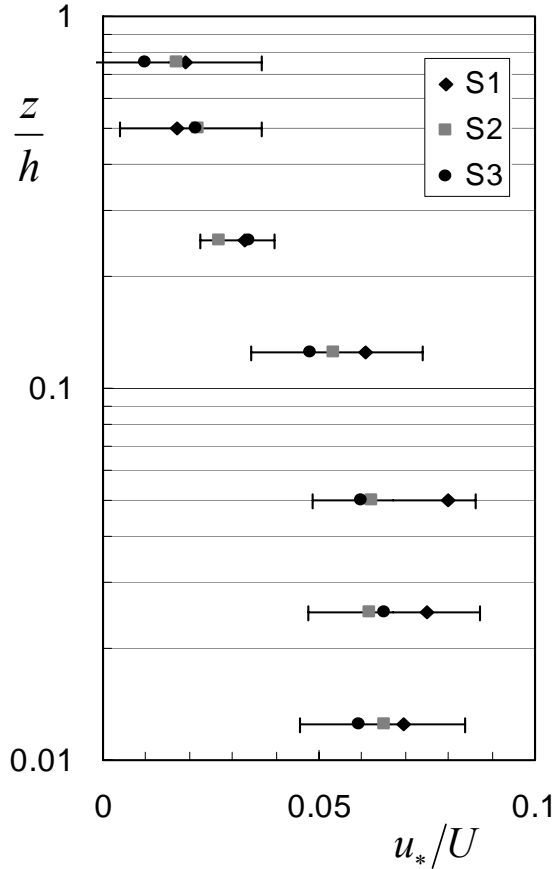


Figure 2.8. Profiles of normalized shear velocity for each of the three measurement stations near the sampling station. The location of the measurement stations is indicated in Figure 2.2. The error bars show +/- one standard deviation about the mean for all measurement stations.

The shallow water equation yields an estimate of total boundary stress, whereas the Reynolds fluxes calculated from the ADV measurements yield an estimate of bed stress. To compare these, we estimated total boundary shear stress $\tau_0(m)$ from the bed stress calculated using equation (2.18) by applying the flume sidewall correction procedure of Vanoni (1975) and modified by Chiew and Parker (1994). In the sidewall correction, the bed friction factor is calculated based on the friction factor for the total flow and for the hydraulically smooth sidewall. The sidewall friction factor is estimated from a standard relation between friction factor and Reynolds number \mathbf{R} for a hydraulically smooth surface:

$$\mathbf{R} = 4UR/\nu . \quad (2.20)$$

The bed portion of the shear stress τ_b is then calculated from the bed friction factor. The total stress $\tau_0(m)$ is related to τ_b and the wall stress τ_w as

$$\tau_0(m)PL = \tau_b BL + \tau_w 2hL , \quad (2.21)$$

where L is a length of bed in the streamwise direction and, for a rectangular flume, and the wetted perimeter $P = B + 2h$. The modeled bed stress is approximately 2.5 times the wall stress and 1.8 times the total stress. Figure 2.9 shows $\tau_0(N)$ compared with $\tau_0(m)$. Although there is scatter in the boundary stress calculated from the shallow-water equation, that estimate of stress is generally consistent with the bed stress as determined from the near-bed Reynolds stress. Thus, the simple relation between bed stress and mean velocity (Eq. 2.18) based on the near-bed Reynolds stress provides a convenient measure of bed stress that is also consistent with estimates based on bulk flow parameters.

Nearly all particle entrainment models use grain stress derived by some stress partitioning method (e.g. Engelund and Hansen, 1967; Smith and McLean, 1977; Van Rijn, 1984; Garcia and Parker, 1991). Two fundamentally different methods for stress partitioning are considered here, the form-drag reduction and the stress decomposition. In the form-drag reduction, the drag force F_d contributed by large-scale roughness

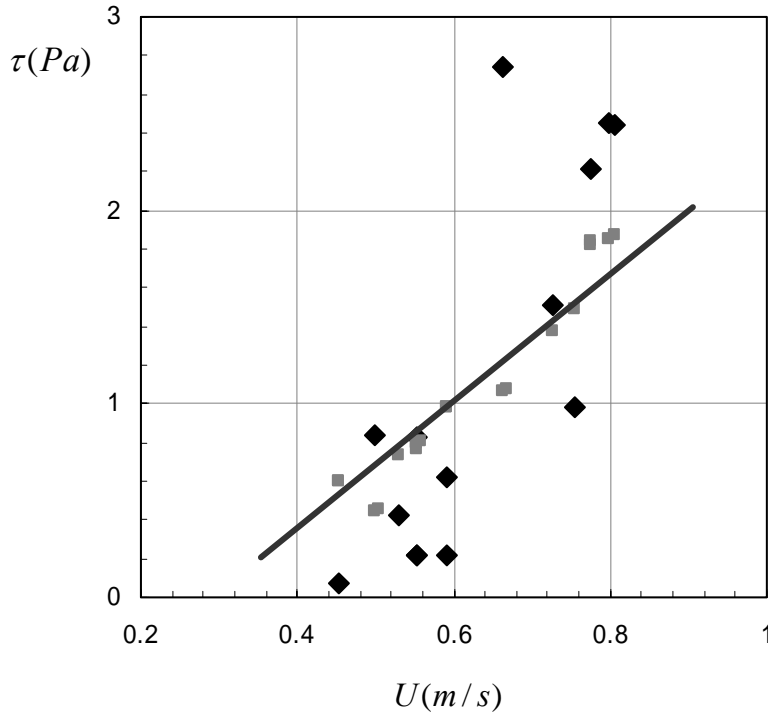


Figure 2.9. Comparison of total average boundary shear stress estimated using the shallow water equation (black diamonds) to the total average boundary shear stress calculated by applying the sidewall correction procedure to the bed stress determined from the near-bed Reynolds stresses (gray squares). The solid line shows the total stress approximated from Eq. 2.18 with the sidewall correction applied.

elements, bedforms or large immobile particles, is calculated as a function of the form geometry and the near bed velocity profile.

$$F_d = \frac{\rho}{2} C_D A_d \int_{z_s}^{r_b} \bar{u}^2, \quad (2.22)$$

where C_D is a coefficient of drag and A_d is the area of the bedform or roughness element presented to the flow. This method was used by Smith and McLean (1977) and has been applied in modified form by Wiberg and Smith (1991) and Nelson et al. (1991), among others. The calculated form drag is subtracted from the total stress to determine the grain stress. Because the form drag is subtracted from the average bed stress, equation (2.22) must be executed such that the result is the spatially-averaged form drag. The effectiveness of this approach is compromised when the particles that are eligible for

entrainment are distributed such that they are subject to grain stresses that are systematically different from the spatially-averaged grain stress. McLean et al. (1999) identified this problem in the calculation of entrainment of sand into suspension from bedforms. They determined that most entrainment occurred near the top of a bedform where the grain stress was higher than in the dune troughs. Additionally, instantaneous measurements of Reynolds fluxes have shown large spatial and temporal variations of local stress in the presence of bed forms or other large roughness elements (Nelson et al., 1995; McLean et al., 1999), and it has been demonstrated that particle entrainment in wakes is not always associated with turbulent events that contribute positively to bed shear stress (Nelson et al., 1995). In our experiments, the sand was nonuniformly distributed among the roughness elements, such that some was near the bottom of the interstitial spaces and some was at elevations at or near the top of the roughness elements (Figure 2.3). This condition existed for all of the runs with minimal or partial sand cover, and there was never a situation where the sand partially filled the interstitial spaces to an even depth throughout the channel (Figure 2.3). Thus, the bed is never configured such that one can reasonably assume that all of the sand is subject to the same spatially-averaged grain stress. While the form-drag reduction can be used to estimate a mean grain stress, for a variety of immobile roughness exposure conditions (i.e. different sand bed elevations among the coarse grains), the calculated grain stress will always be spatially-averaged and never correspond directly to local grain stress that is causing entrainment.

Alternatively, grain stress may be estimated by stress decomposition. This method was first proposed by Einstein and Barbarossa (1952). Engelund and Hansen (1967) applied this method in modified form and it has also been implemented in recent applications (Garcia and Parker, 1991; Wright and Parker, 2004). At the core of this approach is the analogy between the flow of interest and a hypothetical flow that has the same slope and mean velocity but lacks the drag exerted by bedforms. In the application considered here, this analogy is extended to exclude the drag exerted by the large bed

roughness elements in the hypothetical flow. The mean velocity is related to the bed stress through a standard resistance relation

$$\frac{U}{u_{*b}} = \frac{1}{k} \ln \left(\frac{11h}{k_s} \right), \quad (2.23)$$

where U is the mean velocity, h is the flow depth, k is the von Karmen constant, and k_s is the Nikuradse equivalent grain roughness associated with the total bed stress. By the analogy of the Einstein decomposition, a similar relation holds for the hypothetical flow:

$$\frac{U}{u'_{*b}} = \frac{1}{k} \ln \left(\frac{11h'}{k'_s} \right), \quad (2.24)$$

where h' is the flow depth due to grain stress and k'_s is the grain stress roughness height. Here $k'_s = 3D_{50}$ is used. The slope S of the hypothetical flow is also the same as that of the flow in question, thus,

$$u_{*b} = \sqrt{ghS}, \text{ and} \quad (2.25)$$

$$u'_{*b} = \sqrt{gh'S}. \quad (2.26)$$

Combining equations (2.25) and (2.26),

$$\frac{u'_{*b}}{u_{*b}} = \sqrt{\frac{h'}{h}}. \quad (2.27)$$

Given the total stress and the mean velocity, equations (2.24) and (2.27) can be solved iteratively for the grain stress. This method does not involve an explicit calculation of form drag. Any flow with the same energy gradient and mean velocity is assumed to possess the same form drag and grain stress if the mobile particles have the same size distribution. However, in our application the local grain stress is spatially variable and the effect of this unequal distribution of grain stress is, in essence, the phenomena that we seek to investigate. By using a method for the calculation of grain stress that does not vary as the relative exposure of the partially buried roughness elements varies, we are relegating all variability in the entrainment rates to our entrainment formulation, which does depend on condition of the sand bed. Thus, the Einstein stress decomposition is more consistent with our approach, which is to examine the integrated effects of spatially

variable grain stress and other factors related sand bed configuration on near-bed suspended sediment concentrations.

Vertical distribution of suspended sediment and determination of the reference elevation

The governing equation for sediment mass balance in the flow is the advection-diffusion equation. Retaining the terms for streamwise advection and vertical diffusion and settling, it can be written

$$\frac{\partial c}{\partial t} + u \frac{\partial c}{\partial x} - w_s \frac{\partial c}{\partial z} = \frac{\partial}{\partial z} \left(K \frac{\partial c}{\partial z} \right), \quad (2.28)$$

where c is the time-mean concentration of suspended sediment and K is the diffusion coefficient for suspended sediment. If the diffusivity of sediment is assumed to be the same as that of water and is specified using a logarithmic velocity profile and linear stress distribution, equation (2.28) may be solved analytically for an equilibrium suspension to yield the well-known Rouse distribution (Rouse, 1936)

$$\frac{c}{c_a} = \left[\frac{(h-z)/z}{(h-a)/a} \right]^{R_o}, \quad (2.29)$$

in which c is the time-mean concentration of suspended sediment and c_a is the concentration at reference elevation $z = a$. It was shown above that for equilibrium transport, the near-bed concentration is equal to the dimensionless rate of particle entrainment. The reference elevation a is not formally specified, but is usually taken to be near the bed, either scaling with the grain size of the sediment in transport (e.g. Englund and Fredsoe, 1976) or flow depth (e.g. Celik and Rodi, 1988; Garcia and Parker, 1991). Often, the selection of a reference elevation is driven by practical considerations to be the lowest elevation at which accurate measurements of suspended sediment concentration are possible.

Measured profiles of suspended sediment concentration are shown in Figure 2.10 together with theoretical profiles, calculated using equation (2.29) and the measured concentration at the indicated reference elevation c_a . These profiles show that concentrations in the upper part of the flow are predicted better by the Rouse distribution

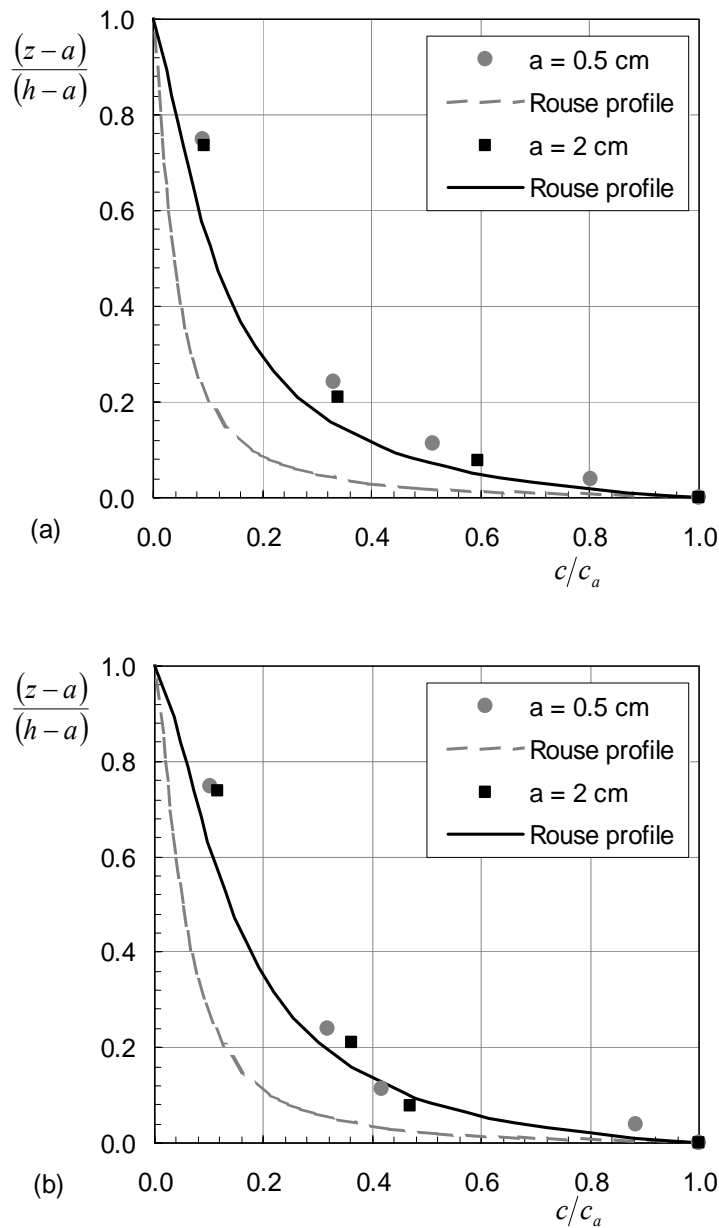


Figure 2.10. Measured suspended sediment concentrations normalized by the reference elevation and the near-bed concentration and modeled profiles of sediment concentration based on Rouse distribution calculated for the indicated near-bed reference elevation a . Data are from experimental runs 12 (a) and 14 (b).

when the reference elevation is 2 cm than when it is 0.5 cm. This behavior is consistent with the vertical structure of the velocity profile over the bed roughness elements (Figure 2.7). The Rouse distribution is based on a logarithmic velocity profile, which did not exist in the lower 2 cm of the flow (Figure 2.7). This type of profile is consistent with

other profiles measured over very rough beds (Byrd et al., 2000). The elevation of 2 cm is equivalent to $0.05h$, which is among the more frequently used measures of the reference elevation (Itakura and Kishi, 1980; Celik and Rodi, 1988; Garcia and Parker, 1991).

Sand elevation correction function

The observed rapid transition from full sand cover through a partially sand covered bed to a bare bed indicates that, for some range of average sand bed elevations between $z_s = 0$ and $z_s = r_b$, the rate of sand entrainment per unit bed area covered by sand should be greater than that which would occur from a completely sand-covered bed. To examine this possibility, we calculate entrainment for a sand-covered bed \hat{E}_s as a reference condition. Figure 2.11 shows entrainment predicted by the Garcia and Parker (1991) entrainment model (Eq. 2.11) compared with our observed near-bed concentrations and our observed near-bed concentrations normalized by the proportion of bed covered by sand,

$$\hat{c}_a = A_s c_a, \quad (2.30)$$

where \hat{c}_a is the concentration for a sand-covered bed, A_s is the proportion of the bed covered by sand, and c_a is the observed near-bed sand concentration. In calculating entrainment using equation (2.11), we used the grain stress determined by the Einstein decomposition (Eqs. 2.23 to 2.27), which is consistent with the method used by Garcia and Parker (1991) in developing their entrainment relation. The near-bed concentration was evaluated at 5% of the flow depth (2 cm) and only observations from runs resulting in minimal or partial sand cover (Table 2.1) were included. The observed concentrations are smaller than predicted by the entrainment model, which means that concentrations for conditions of partial sand cover were smaller than concentrations that would be predicted for the same flow over a full sand bed. However, the observed concentrations per unit bed area covered by sand are larger than predicted by the entrainment model. This indicates that the rate of entrainment per unit area of bed covered by sand is larger for conditions of partial sand cover than for a full sand bed.

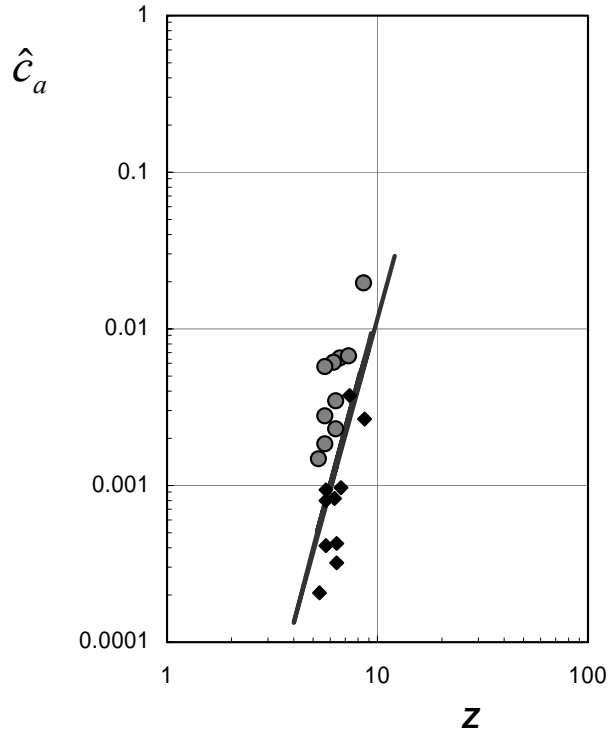


Figure 2.11. The near-bed sand concentration predicted by the Garcia and Parker (1991) entrainment model (sold line) and the observed concentrations at 2 cm above the hemisphere tops (black diamonds). The shaded circles show the observed concentrations normalized by the area of bed that was covered by sand.

These results can be expressed in terms of a sand elevation correction function that relates the actual entrainment over a partially sand-covered bed E_s to the full sand bed entrainment rate \hat{E}_s predicted by the Garcia and Parker (1991) entrainment model. The sand elevation correction ε is defined

$$\varepsilon = \frac{E_s}{\hat{E}_s} . \quad (2.31)$$

Figure 2.12 shows ε plotted as a function of the normalized sand bed elevation \hat{z}_s , where

$$\hat{z}_s = \frac{z_s}{r_b} . \quad (2.32)$$

Although there is scatter in the data, a rapid increase in the entrainment rate for $0.1 < \hat{z}_s < 0.5$ is indicated. The function shown in Figure 2.12 is a logistic function

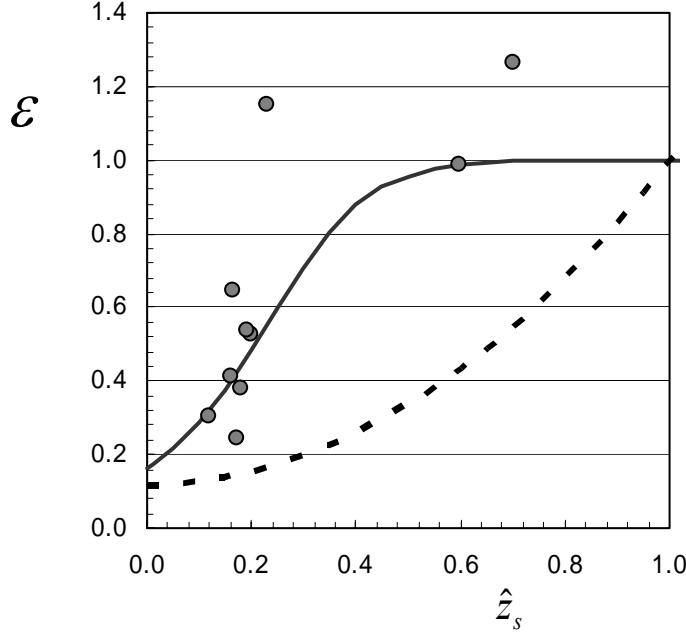


Figure 2.12. The sand elevation correction ε plotted as a function of the normalized sand bed elevation \hat{z}_s . The data points are the ratio of observed near-bed concentrations to concentrations predicted for a full sand bed c_a/\hat{c}_a . The solid line is the logistic function (Eq. 2.33), and the dashed line is a function for the area of exposed sand (Eq. 2.35).

chosen to fit the observations for $\varepsilon \leq 1$. Although the data suggest the shape of this function, the strongest constraints are those imposed at the extremes of the function. As the bed approaches full sand coverage, the entrainment must approach that of a full sand bed, and as the sand bed elevation approaches zero the net rate of entrainment must approach zero. Thus, some function that increases from zero to one is expected.

Although there are two data points where $\varepsilon > 1$ and it is possible that entrainment rates could exceed those predicted for a full sand bed for a range of partial sand-bed elevations, those data are few and, given the range of scatter indicated by the other data, can not be considered significantly different than $\varepsilon = 1$. The logistic function shown in Figure 2.12 is given by

$$\varepsilon = \left(1 + e^{-\xi(\hat{z}_s - Z^*)}\right)^{-\eta}, \quad (2.33)$$

with $\xi = 12$, $Z^* = 0.3$, and $\eta = 0.5$.

The proposed rough-bed entrainment correction is compared with a correction based solely on the proportion of bed covered by sand

$$\varepsilon = \frac{A_s}{A_b}. \quad (2.34)$$

For hemispheres the area of sand A_s normalized by the total bed area A_b is related to the sand depth by

$$\frac{A_s}{A_b} = \frac{B - N\pi(r_b^2 - z_s^2)}{B}, \quad (2.35)$$

where N is the number of hemispheres per meter of channel length, and B is the channel width. If this function were used as a sand-elevation correction, predicted entrainment rates would be much lower than observed entrainment rates. Entrainment rates predicted with the logistic function (Eq. 2.33) are compared with the measured near-bed concentrations in Figure 2.13. Use of the sand-elevation correction reduces the scatter in the predicted concentrations and results in a better match between predicted and observed concentrations.

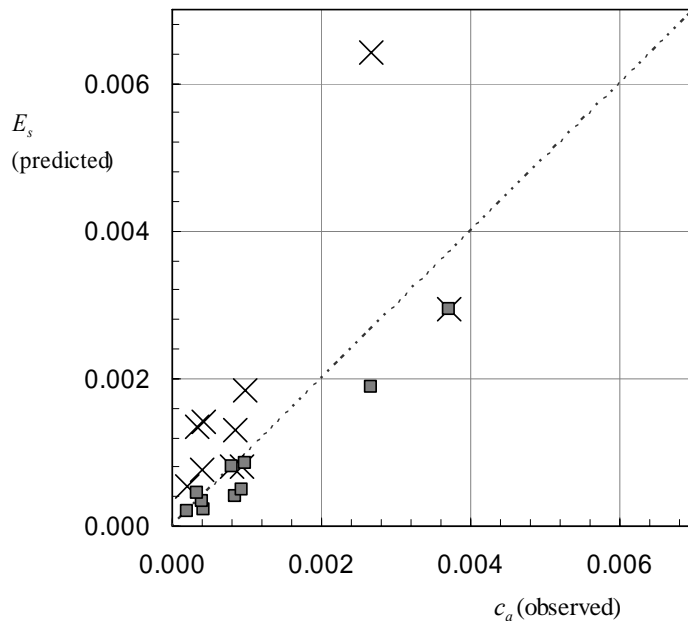


Figure 2.13. Comparison of sand entrainment rate predicted with the sand elevation correction (squares) and without the correction (x's) compared to observed near-bed sand concentrations. The dashed line is a line of perfect agreement.

Conclusions

Accurate prediction of the sediment entrainment rate is a critical component of any fine sediment transport and routing model. Primary controls on the entrainment rate are the grain size of the available sediment and the shear stress at the bed, although when suspended sediment is transported over a partially covered bed of coarse and immobile grains, entrainment also depends on the volume and configuration of fine sediment on the bed. We found that conditions of spatially-uniform partial sand cover were difficult to achieve and could be produced only within a limited range of discharge and sediment feed combinations. By itself, this result suggests that entrainment rates increase as sand bed elevations drop below the elevation of the exposed immobile grains – sand is rapidly evacuated once the immobile grains are exposed. In fact, the entrainment rates that we observed were higher per unit bed area that was covered by sand, but the net entrainment rate from the entire bed was lower than for a full sand bed.

The sand elevation correction function encompasses these competing effects of decreasing sand cover and increasing rate of entrainment per unit sand area. Accelerated local entrainment that occurs as the coarse grains become exposed and generate near-bed turbulence is compensated by the decreasing exposed area of sand available for entrainment. For average sand bed elevations greater than about $0.5r_b$, the effect of enhanced entrainment per unit sand area maintains the net entrainment rate at approximately the rate that occurs for a full sand bed. This results in rapid evacuation of sand once the immobile grains are exposed. When the sand bed elevation decreases below $0.5r_b$, the decreasing area (and volume) of sand available for entrainment begins to restrict the net rate of entrainment, despite high entrainment per unit area that is covered by sand. This decrease in the net entrainment rate can then slow the rate of sand evacuation when the sand bed elevation is less than $0.5r_b$. This physical explanation is consistent with the frequent occurrence of average sand bed elevations between $0.1r_b$ and $0.3r_b$, and few observations greater than $0.4r_b$.

Further investigation is required to test (1) the sensitivity of a sand routing model to different forms of the sand elevation correction and (2) the degree to which different

sizes, size distributions, and arrangements of immobile grains affect the shape of the sand elevation correction.

Chapter 3: Observations of evolving bed configuration under conditions of non-uniform transport of suspended sediment over a coarse immobile substrate

Introduction

Bed forms are among the most common features associated with the transport of sediment by air or by water. The description and classification of bed forms as well as their dynamics and associated fluid mechanics have been central topics of research in the fields of sedimentology, geomorphology, and engineering for decades. Understanding the fluid flow and sediment transport conditions that create specific bed form morphologies is a critical element of interpreting the stratigraphic record and is also a key element in predicting rates of sediment transport in active river channels. The characteristics and dynamics of bed forms that exist in uniform or well-mixed bed sediment conditions have been widely studied and are well understood (Allen, 1982; Southard, 1991; Best, 1996). Less effort has been applied to the study of bed forms that develop as fine sediment is transported over a bed of coarse and immobile grains.

Beds partially covered with fine sediment indicate that the supply of fine sediment is smaller than the capacity of the stream to transport that sediment. One of the characteristics of these conditions is a bed configuration consisting of stripes or isolated barchan bed forms (McCulloch and Janda, 1964; Allen, 1968; Carling et al., 2000a; Carling et al., 2000b; Kleinhans et al., 2002). Kleinhans et al. (2002) used a wide range of field and laboratory data to examine the stability regimes of bed states composed of bimodal sand-gravel sediment mixtures in conditions of partial sand cover. They identified small and large dunes, barchans, and sand ribbons (stripes). Barchans are individual unconnected bed forms that migrate over an immobile base that is exposed between the features. Barchanoids are a transitional form between barchans and dunes, and occur when the entire bed, including the deepest troughs between dunes, is fully mobile. Kleinhans et al. (2002) proposed a bed state stability diagram that illustrated the transition from sand stripes to barchans to dunes as the volume of mobile sediment decreased.

In a river bed composed of immobile grains or bedrock, both bed configuration and transport rate depend entirely on the supply of the mobile sediment. In the Colorado River downstream from Glen Canyon Dam, tributaries contribute fine sediment that has a mean diameter on the order of 0.10 mm that is transported downstream in the Colorado River over a largely immobile bed of cobbles and boulders (Figure 3.1). This fine sediment may completely cover the coarse substrate for periods of time, but as the supply is winnowed (and coarsened), conditions of partial cover occur. Similar conditions exist in mountain rivers that have fine sediment moving over a coarse immobile substrate. Habitat conditions, sediment storage, and sediment transport rates and yield depend of the bed configuration. The bed forms that develop in these circumstances and their effect on particle entrainment into suspension are poorly understood.



Figure 3.1. Gravel bar exposed at low flow on the Colorado River in Grand Canyon.

The purpose of this paper is to present data from large-scale laboratory experiments that describe bed form morphology, grain size and distribution for suspended sediment transport over a coarse-grained immobile bed that is partially covered with fine sediment. We report on bed configuration and the associated flow and transport field, discuss the mechanisms producing stripes and barchans, propose a suitable stability field, and develop a simple model for predicting bed form coverage as a function of the average elevation of the fine sediment. This expands on previous work, which focused on bed load and using sediments for which all sizes are mobile at some flows (Kleinhans, 2002).

Methods

Experimental design

These experiments were designed to investigate at nearly field scale the transport of suspended sediment over a bed of partially covered coarse immobile grains. The field analog is a river with a coarse immobile substrate transporting a variable supply of fine sediment (Figure 3.1). Because the focus of the experiments was the interaction between the sediment in transport and the evolving bed configuration, the essential scaling properties are those that determine the near-bed flow and sediment entrainment conditions and those that influence the development of mobile bed forms. Thus, these experiments featured (1) sufficient flow depth to allow bed form development, (2) a large size ratio between the sand in transport and the immobile bed material, and (3) a ratio between bed shear stress and particle settling velocity, expressed as the Rouse number R_o , typical of transport in suspension. The Rouse number is given by

$$R_o = \frac{w_s}{ku_*}, \quad (3.1)$$

where w_s is the particle settling velocity, k is von Karmans's constant, and u_* is shear velocity.

The material used for the fine-sediment feed was a natural quartz sand with a median diameter of approximately 0.13 mm (Figure 3.2). Bed roughness was created by installing 15-cm diameter concrete hemispheres in a 40-m test section of an 84-m long

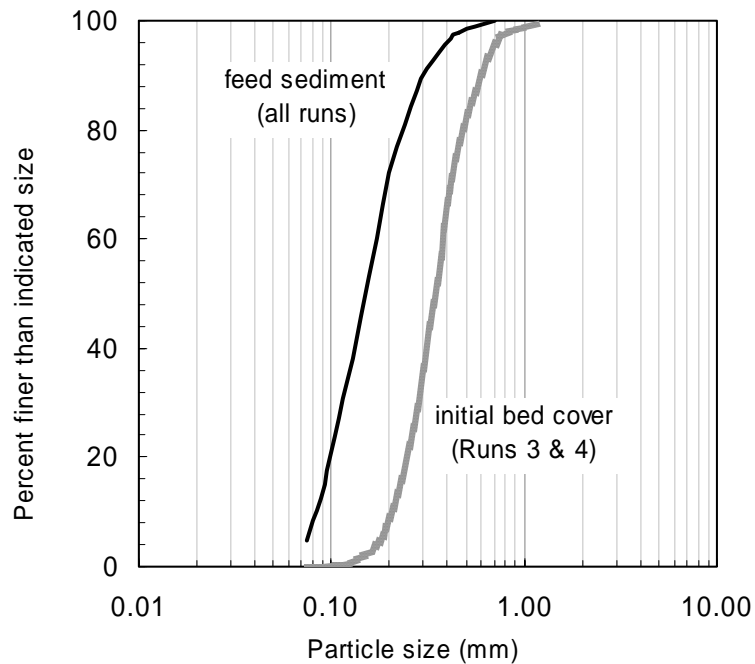


Figure 3.2. Size distribution of feed sediment and sediment used for initial bed cover.

concrete rectangular channel located at the St Anthony Falls Laboratory of the University of Minnesota (Figure 3.3). The 5400 hemispheres covered the full 2.74 m width of the channel and were installed in closest-packing arrangement. The ratio between the size of the large grains and the feed sediment is of order 10^3 and large enough that interactions between the immobile bed and the mobile sediment are adequately represented. The length scale relevant for sediment storage in the bed is the height of the immobile grains above the flat bed surface, which is the hemisphere radius r_b and is 7.5 cm. The flow depth over the tops of the hemispheres was 60 cm for all runs, in order to allow a spatially integrated region in the flow above the near bed region and to provide sufficient depth for the development of a range of bed forms (Southard, 1991). Two flow rates were used, both of which produced Rouse numbers less than one such that the dominant mode of transport would be in suspension, and Froude numbers less than one to ensure lower regime flow conditions and bed forms (Table 3.1). The bed slope was 0.0005 for all experimental runs.



Figure 3.3. Photograph looking upstream at the 40 m test section with installed bed of 15-cm diameter hemispheres.

Table 3.1. Rouse number R and Froude number Fr associated with the two flow velocities used in the Main Channel experiments.

| U (m/s) | u_* (m/s) | u'_* (m/s) | R^1 | Fr^2 |
|--------------|-------------|--------------|-------|--------|
| 0.50 | 0.043 | 0.024 | 0.68 | 0.21 |
| 0.76 | 0.065 | 0.037 | 0.45 | 0.31 |

¹ The Rouse number was calculated using the feed sediment grain size of 0.13 mm, common to all runs.

² The Froude number was calculated using the flow depth of 60 cm, common to all runs.

Each experimental run began with a 90-min segment with sediment feed, followed by one to four additional segments without sediment feed (Table 3.2). Fine sediment was fed into the channel upstream from the test section with an automatic feeder and apparatus that distributed sand to four vertical pipes with bottom openings positioned 16 cm above the channel bottom. To avoid clogging of sand in the feed pipes, a small stream of water was introduced at the top of each pipe. Average concentration during the sediment feed was approximately 750 mg/l. The initial bed condition for Runs

1, 2, and 5 consisted of bare hemispheres (Table 3.2). A layer of fine sediment was installed on the bed for Runs 3 and 4. The initial bed was a well-sorted medium sand

Table 3.2. Summary characteristics of experimental runs.

| Run | Length (min) | Q (l/s) | U (m/s) | Q_s (Mg/hr) | Sed. sample events | Initial | Final bed state | | |
|-----|-----------------|--------------|--------------|------------------|--------------------------|---------------------------|------------------|---------------------|----------------|
| | | | | | | bed state ¹ | D_{50} (mm) | \bar{z}_s (cm) | Configuration |
| 1A | 60 | 801 | 0.49 | 2.1 | 1 | <i>N</i> | -- | -- | -- |
| 1A | 31 | " | " | 2.1 | 1 | | 0.19 | 2.6 | stripe |
| 1B | 60 | 801 | 0.49 | 0 | 2 | | 0.22 | 2.5 | stripe |
| 1C | 145 | 878 | 0.53 | 0 | 3 | | 0.24 | 2.3 | stripe |
| 1D | 365 | 878 | 0.53 | 0 | 3 | | 0.28 | 1.9 | stripe |
| 2A | 60 | 878 | 0.53 | 2.0 | 1 | <i>N</i> | -- | -- | -- |
| 2A | 28 | " | " | 3.5 | 1 | | 0.18 | 2.8 | stripe |
| 2B | 313 | 878 | 0.53 | 0 | 4 | | 0.25 | 1.8 | stripe |
| 2C | 78 | 1311 | 0.80 | 0 | 2 | | 0.38 | 0.8 | barchan |
| 3A | 60 | 835 | 0.51 | 2.0 | 2 | <i>Y</i> | -- | -- | -- |
| 3A | 29 | " | " | 3.5 | 1 | | 0.25 | 3.2 | stripe |
| 3B | 208 | 835 | 0.51 | 0 | 3 | | 0.29 | 2.9 | stripe/barchan |
| 3C | 128 | 793 | 0.48 | 0 | 2 | | 0.32 | -- | stripe/barchan |
| 3D | 240 | 793 | 0.48 | 0 | 2 | | 0.35 | 2.9 | stripe/barchan |
| 3E | 161 | 1209 | 0.74 | 0 | 3 | | 0.46 | 1.9 | barchan |
| 4A | 60 | 1243 | 0.76 | 2.7 | 2 | <i>Y</i> | -- | -- | -- |
| 4A | 31 | " | " | 5.4 | 2 | | 0.34 | 4.4 | stripe/barchan |
| 4B | 53 | 1277 | 0.78 | 0 | 3 | | 0.36 | 3.1 | barchan |
| 4C | 85 | 1254 | 0.76 | 0 | 3 | | 0.44 | 2.4 | barchan |
| 4D | 119 | 1246 | 0.76 | 0 | 4 | | 0.55 | 1.9 | barchan |
| 5A | 60 | 1232 | 0.75 | 2.6 | 2 | <i>N</i> | -- | -- | -- |
| 5A | 33 | " | " | 5.3 | 1 | | 0.21 | 2.1 | stripe |
| 5B | 34 | 1218 | 0.74 | 0 | 3 | | 0.27 | 1.2 | no bed forms |

¹Initial bed state: *N* indicates no sediment bed at the beginning of run; *Y* indicates that 4.4 cm of sand with $D_{50}=0.34$ mm was distributed uniformly among coarse grains before the first segment of the run.

with a median diameter of 0.34 mm (Figure 3.2) that was spread evenly to a thickness of 4.4 cm throughout the test section. Run 1 consisted of constant sediment feed and flow for 90 min, followed by three segments of steady flow at the same rate without sediment feed, resulting in a cumulative run duration of 662 min. The initial flow and feed rate in Run 2 was the same as for Run 1, except the feed rate in Run 2 was increased by 175% for the final 30 min of the 90-min feed segment (Table 3.2). In the final segment of Run 2, the flow rate was increased by 150% to accelerate sediment evacuation. Run 3 used the same initial flow rate and feed pattern as Run 2, but the bed was seeded with a layer of sediment prior to the run. In the final segment of Run 3, the flow rate was increased by 150% to accelerate sediment evacuation. Run 4 had the same initial bed condition as Run 3, but was conducted with a higher flow and feed rate. Run 5 used the same initial flow rate and feed pattern as Run 4, but did not include the initial sand bed.

Measurement of flow

Bulk flow

Flow in the main channel at St. Anthony Falls is controlled by a motor-driven headgate that diverts water from the Mississippi River. This mechanism does not allow precise control of inflow volume, resulting in slightly variable flow rates between run segments (Table 3.2). The flow rate of each segment was measured by collecting outflow for a measured interval in large volumetric tanks. Water surface elevations were recorded by reading temporary staff gages installed at eight locations in the channel to monitor for flow uniformity. These measurements were made to the nearest 0.5 cm.

Velocity observations

To characterize the velocity field over the coarse bed in the absence of mobile sediment, velocity profiles were measured with an acoustic Doppler velocimeter (ADV). Each velocity profile included eight measurement positions located 1, 2, 3.5, 6, 10, 15, 25, and 40 cm above a hemisphere top. These profiles were measured at five cross-channel positions located 45.5, 91.5, 137, 183, and 228.5 cm from the left sidewall. For the smaller discharge, measurements at all five cross-channel positions were made at six

locations along the flume: 1.2, 3.0, 5.1, 7.0, 10.9, and 15.1 m upstream from the downstream end of the test section. Four additional velocity profiles were collected at the center channel position at distances of 19.1, 23.0, 31.1, and 37.2 m (hereafter, all streamwise positions are referenced by distance from the downstream end of the test section). For the larger discharge, velocity profiles were collected at all five cross-channel positions at 1.2, 3.0, 5.1, and 7.0 m. Additional profiles in the center of the channel were collected at 10.9, 15.1, 19.1, 23.0, and 31.1 m. During each run segment, velocity was measured continuously at one position, 2 cm over a hemisphere in the center of the channel at 7 m. All measurements were made at sample rate of 50 Hz for 1 min. or longer with a SonTek 16 MHz MicroADV. This instrument has a maximum sampling rate of 50 Hz and a velocity resolution of 0.01 cm/s up to 250 cm/s. Reported accuracy is 1% of measured velocity. The sampling volume is 0.09 cm³ and is centered 4.67 cm below the probe tip.

The ADV data were processed to remove spikes and analyzed for velocity profiles and turbulence characteristics (Appendix B). Turbulent Reynolds stresses were calculated from the ADV data as

$$u_* = \sqrt{-\overline{u'w'}}, \quad (3.2)$$

where

$$\overline{u'w'} = \frac{\sum uw}{n-1} - \frac{\sum u \sum w}{n(n-1)}, \quad (3.3)$$

u is the instantaneous downstream velocity, w is the instantaneous vertical velocity, and n is the number of instantaneous measurements. Primes denote instantaneous deviations from the mean velocity $u' = u - \bar{u}$ and overbars represent time averages.

Figure 3.4 shows profiles of shear velocity normalized by depth-averaged velocity for all measurement stations including both flow rates. The velocity characteristics vary within this range in both the downstream and cross-stream directions, but the variability is not systematic in either direction (Figure 3.5). Similar variability in the velocity characteristics were also observed when the Reynolds stress was calculated in 1-min

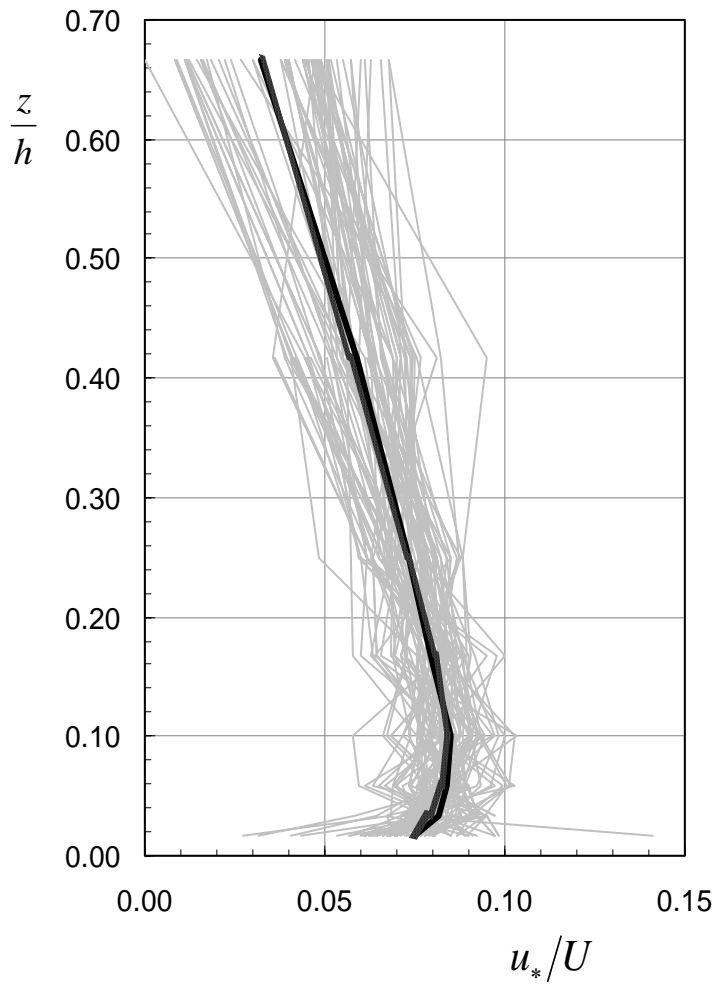


Figure 3.4. Plot showing normalized shear velocity u_*/U as function of normalized elevation above the bed z/h . The light gray lines show the individual measurements for all transverse and downstream positions at both low and high flow rates. The heavy shaded line is the average among all measurement positions for the high flow rate and the heavy black line is the average among all measurement positions for the low flow rate.

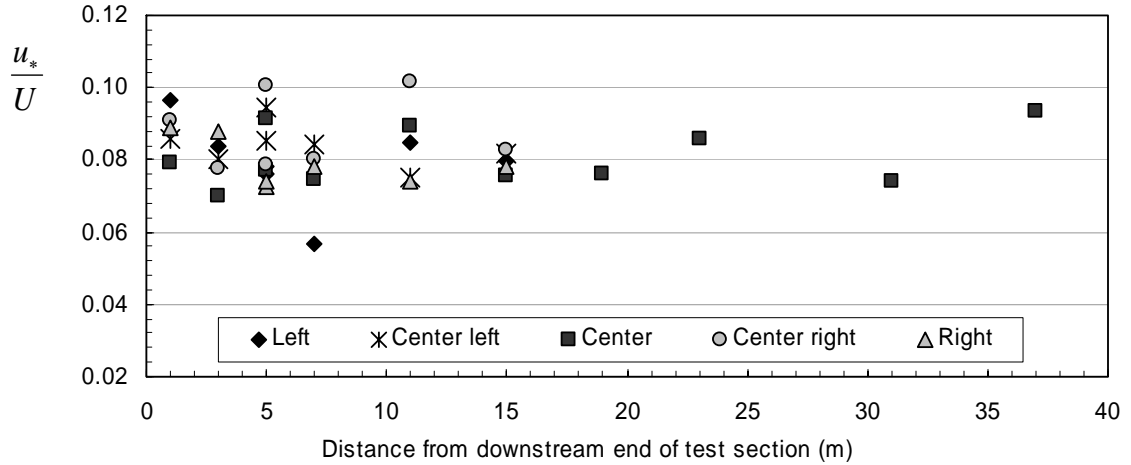


Figure 3.5 Plot showing the normalized shear velocity u_*/U computed at each of the 5 cross-channel and 10 downstream measurement locations. Measurements were made in the center of the channel only for the measurement stations upstream from 15 m.

windows over the course of an entire run segment. Despite the variability, there is a consistent pattern in the Reynolds stress in the near-bed region (Figure 3.4). The stress decreases linearly from the upper region down to approximately $0.10h$ above the hemispheres (Figure 3.4). From this height down to about $0.05h$, the mean shear stress is constant and equivalent to about $0.085U$. Closer to the bed, the measured Reynolds stress decreases. Voulgaris and Trowbridge (1998) reported that Reynolds stresses computed from ADV measurements within 3 cm of the bed deviate from expected flow characteristics while those computed above 3 cm were in good agreement. Expected flow characteristics were estimated with a statistical model using velocity records collected simultaneously by an ADV and a laser Doppler velocimeter. Other researchers have reported errors in ADV measurements near the bed resulting from shear within the sampling volume (Kim et al., 2000). Therefore, the Reynolds stresses measured within the short segment of constant stress are considered to be the most reliable estimate of average bed stress. Based on these observations, the bed stress for both flow conditions is calculated from the mean velocity as

$$u_* = 0.085U . \quad (3.4)$$

Measurement of bed topography and grain size

Following each run segment, the entire bed was photographed from above (Figure 3.6). The sand depth above the elevation of the base of the hemispheres was measured using a ruler at locations on a grid defined by 18 or 19 transverse positions and 34 streamwise positions at 1.2 m intervals (Figure 3.7). The transverse positions were at each interstitial gap between hemispheres. There are 18 gaps for even-numbered rows, which have a half-hemisphere on the edges of the channel and there are 19 gaps for odd-numbered rows, which have whole hemispheres on the edges of the channel. At each gap between hemispheres, a measurement was made in the interstitial space on the upstream and downstream side of the gap, forming a measurement pair. Measurements were made in this way to avoid bias towards interstitial spaces that are immediately downstream of either a hemisphere center or a gap between two hemispheres. The measurements were made in alternating odd and even-numbered rows to avoid bias in cross-stream position. A typical measurement set consisted of 630 measurement pairs, or 1260 individual measurements. The sand depth was measured to the nearest millimeter with a ruler constructed to fit in the interstitial spaces.

Bed material samples were collected from each of four distinct deposit facies. The area at the upstream end of the test section where more than 90% of bed roughness elements were completely buried was identified as the accumulation zone. The stripe facies consist of longitudinal sand stripes that extend several meters or tens of meters in the downstream direction and are on the order of one bed roughness element diameter in width. Non-stripe facies are areas of interstitial sand storage that are not part of a sand stripe. Samples from dune facies were collected in those run segments where isolated dunes existed. Samples of the surface (upper 0.5 cm), sub-surface (0.5 to 2 cm below surface) and body (more than 2 cm below surface) of each deposit facies were collected at distances of 10, 25, and 34 m in the test section. At each of these sample locations, several sub-samples were collected from multiple cross-channel positions and combined to form an integrated sample. In the runs that included the seeded bed and resulted in more complex bed stratigraphy, sediment cores were collected and photographed at



Run 1A



Run 1B



Run 1C



Run 1D



Run 2A



Run 2B



Run 2C



Run 3A



Run 3B



Run 3C



Run 3D



Run 3E



Run 4A



Run 4B



Run 4C



Run 4D



Run 5A



Run 5B

Figure 3.6 (pages 45-48). Photographs of bed at the conclusion of each run segment (Table 3.2). In each image, the channel width is 2.74 m and the length is 40 m. The small white tabs along the top of each image are at 1 m intervals. Flow was from left to right.

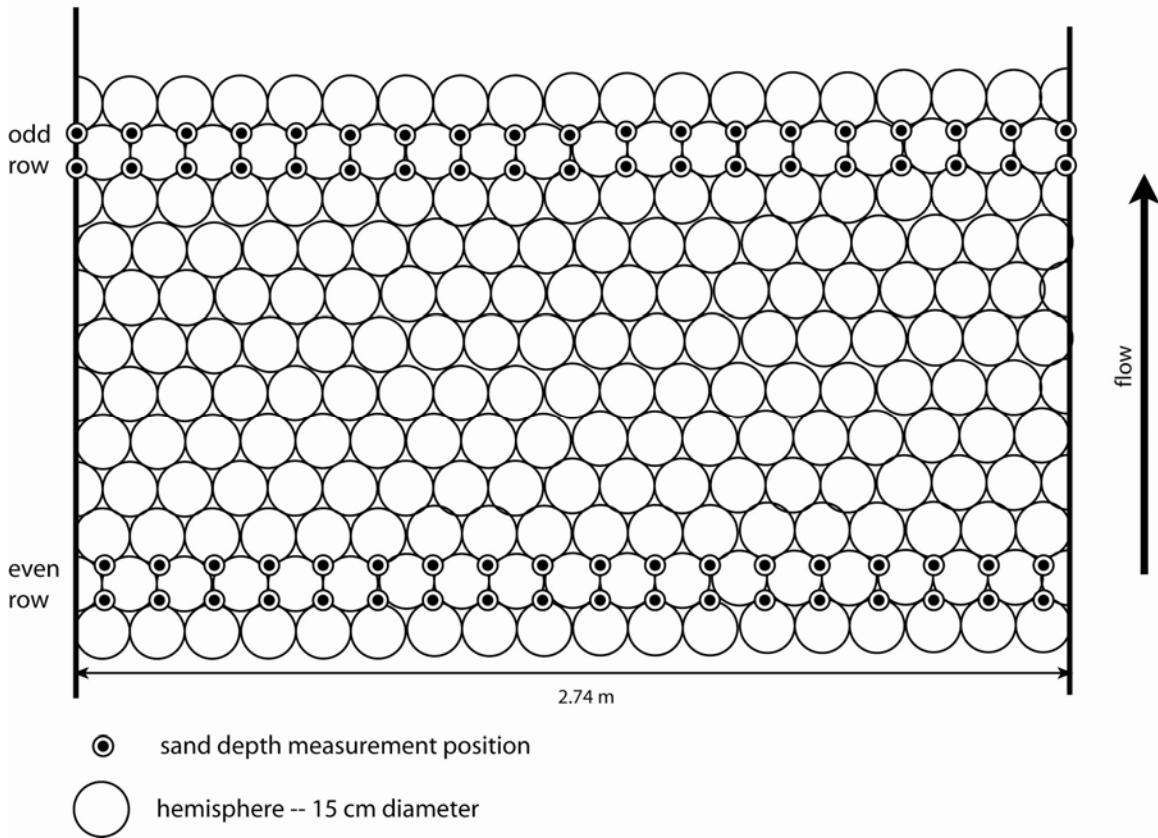


Figure 3.7. Diagram showing locations for measurements of sand depth.

multiple locations in the test section. Samples were retained from several of the cores for grain size analysis. All sediment samples were analyzed using wire sieves for the fraction larger than 0.5 mm and a Sequoia Scientific LISST-100 laser-diffraction particle size analyzer with a laboratory mixing chamber for the fine fraction (Appendix C).

Measurement of suspended sediment

Siphon samples

Direct measurements of sediment concentration were made during each run segment by collecting water samples through isokinetic siphon sampling tubes. The tube inlets were positioned 5.17 m upstream from the downstream end of the test section

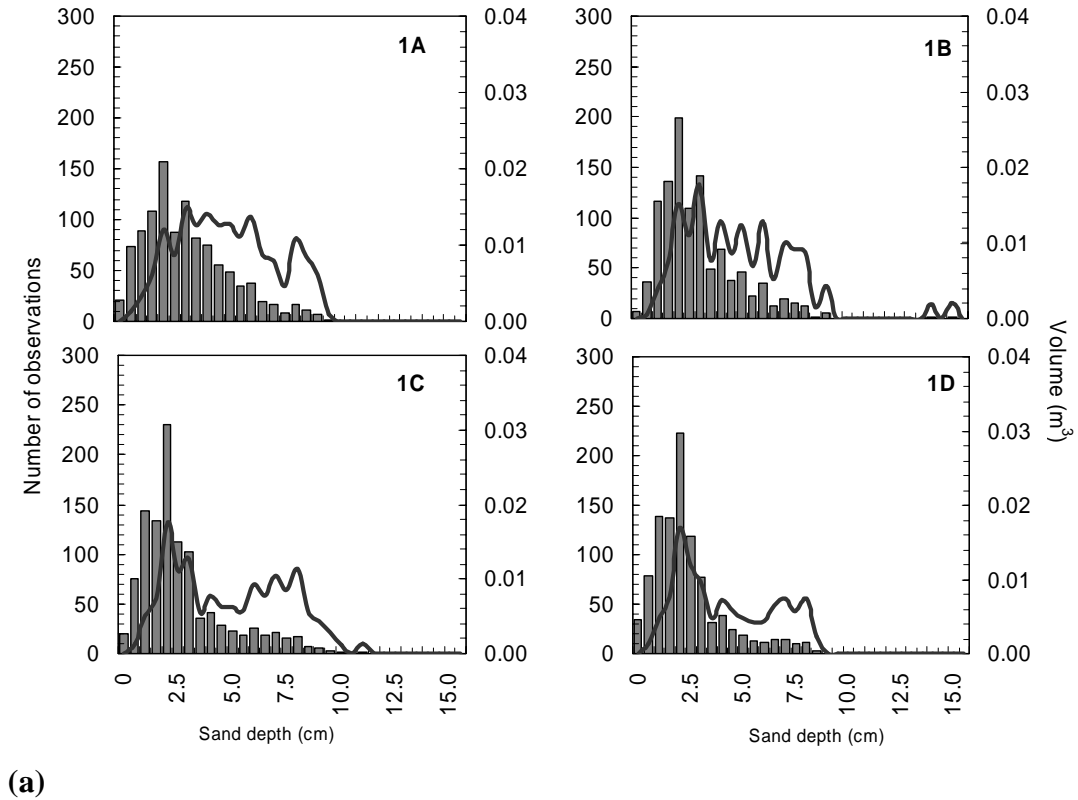
(22.17 m from downstream end of flume) in three cross-channel positions and at five elevations above the hemisphere tops. The inlets were positioned directly above hemisphere tops. The three cross-channel positions were 44, 136, and 227 cm from the left sidewall. The tube inlets were positioned 1, 2, 6, 15, and 40 cm above the hemisphere tops. In most cases, samples were collected simultaneously from all 15 siphons during each sample event. In some cases, individual tubes were sampled. There were between 2 and 4 sample events in each run segment (Table 3.2). Sample durations typically ranged from 60 to 90 seconds, depending on the flow rate. Each sample was analyzed for suspended sediment concentration and selected samples were analyzed for grain size (Appendix D). Suspended sediment concentrations were also measured continuously by three laser-diffraction instruments positioned in the center of the channel 2 m downstream from the siphon samples. The instrument in the center of the channel was positioned such that the sampling volume was from 11 to 16 cm above the hemispheres (Sequoia Scientific LISST-100). The instruments positioned left and right sides of the channel (45 cm and 27 cm from the left channel wall) were positioned such that their sampling volume was centered 5 cm above the hemispheres (Sequoia Scientific LISST-25x). Details regarding the deployment of this and other sediment sampling instruments are included in Appendix E.

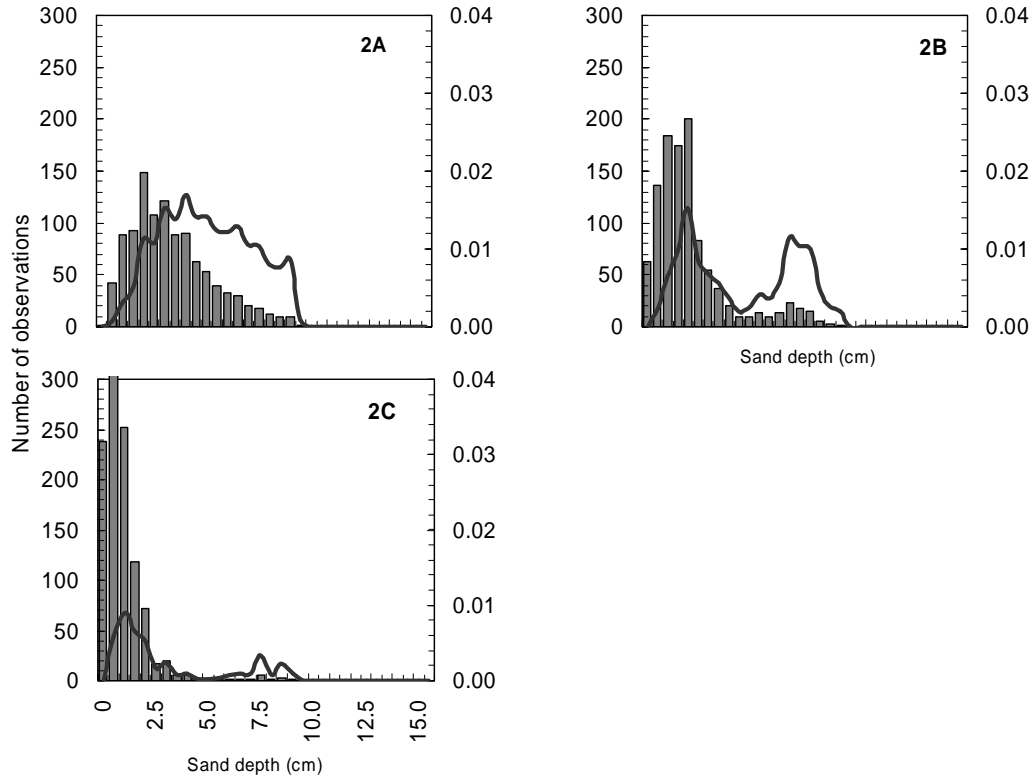
Results

Description of bed configuration

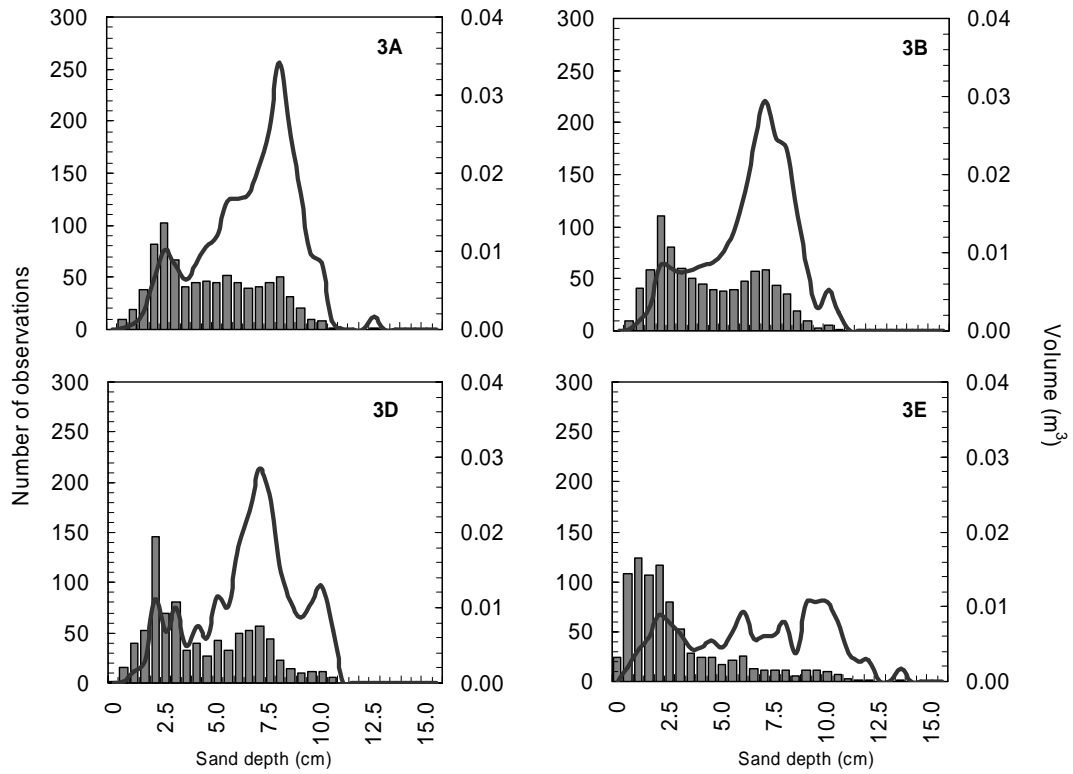
Sand accumulated on the bed of the channel during the feed segment of each run. The thickness of accumulation was greatest in the upstream 10 m where a large proportion of the bed roughness was buried (Figure 3.6). Downstream from the sand accumulation zone, the sand organized into patches consisting of sand stripes or barchan dunes. The sand stripes ran parallel to the flow, often extending nearly the entire length of the 40 m test section. Occasionally, individual stripes bifurcated to form two stripes or two stripes coalesced to form a single stripe. These patterns typically occurred only in the run segments with greater areas of sand coverage. The elevation of the crests of the sand stripes was generally near the top of the hemispheres (7.5 cm) and the width of individual

stripes varied from about $0.5r_b$ up to about $3r_b$. We identified as barchans isolated bed forms that had an orientation transverse to the flow direction. Some of the barchans had a classic crescent shape with horns extending downstream (e.g. Run 4D), however, in many cases, they had irregular form and were connected by sand stripes (e.g. Run 4A) or occurred in a series of barchans (e.g. Run 4B). The average elevation of sand in barchans was also on the order of the bed roughness height. Between the bed forms, sand partially filled the interstices of the coarse grains. Regardless of the dominant bed configuration, the distribution of bed elevations is similar from run to run (Figure 3.8). The parts of the bed that are not part of a barchan or a sand stripe have a modal elevation of about 2 cm ($\sim 0.25r_b$). Parts of the bed that are covered by bedforms do not have a distinct peak, but occupy the shoulder of the distribution with a average elevation of about 6 to 7.5 cm ($\sim 0.8r_b$ to $1.0r_b$).

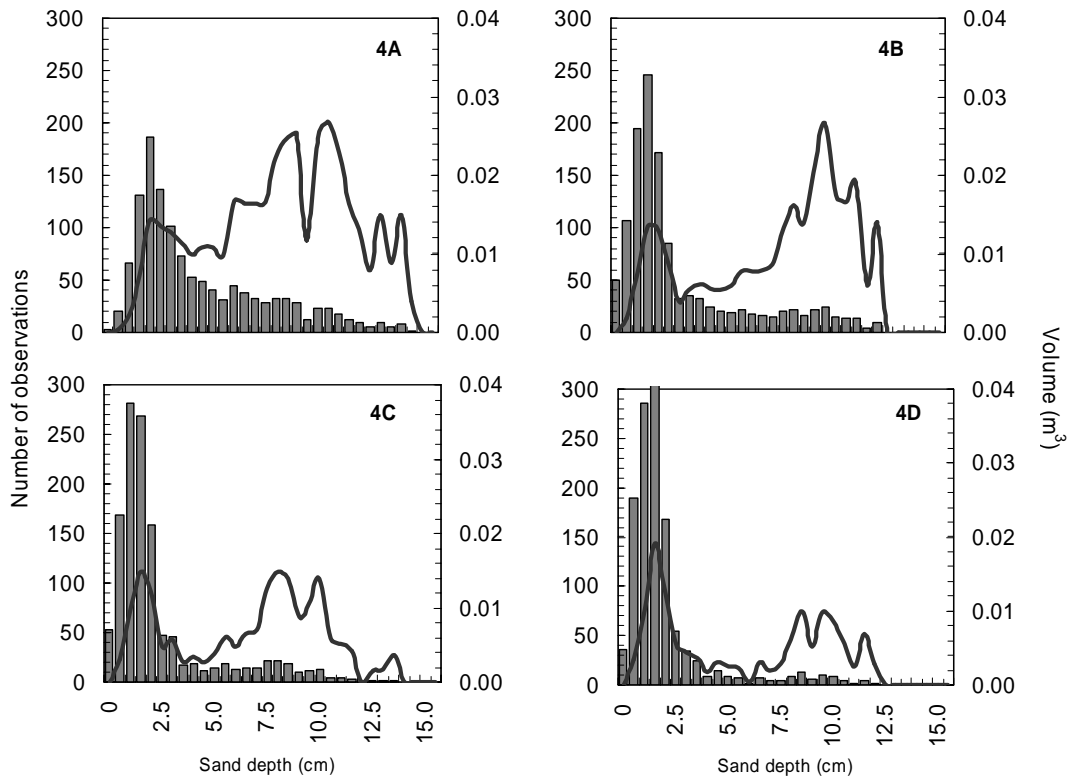




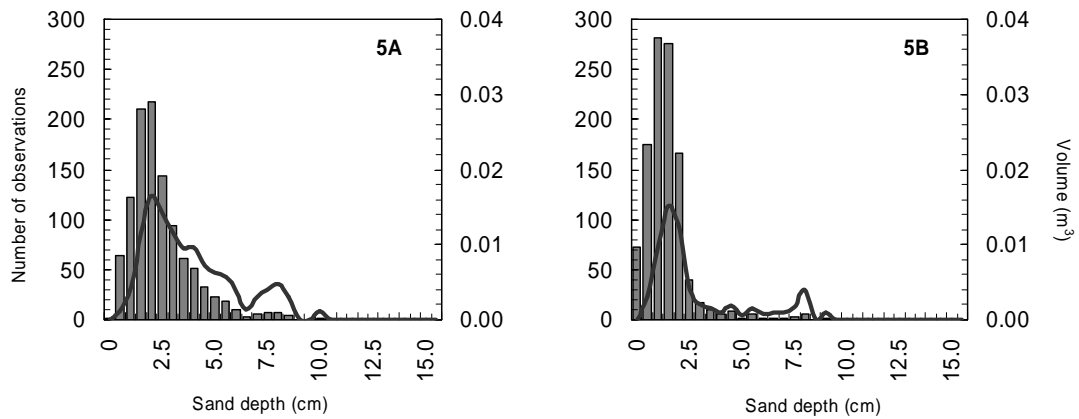
(b)



(c)



(d)



(e)

Figure 3.8. Frequency distribution of sand bed elevations for each segment of each run (shaded columns). The line on each plot is the volume of sand stored on the bed within each bin of the frequency distribution.

In run segments with sand stripes, the stripes formed at the downstream end of the accumulation zone and extended throughout most of the length of the test section (Figure

3.6). The cross-channel uniformity of the deposit in the accumulation zone demonstrates that sediment was well mixed at the upstream end of the test section and indicates the stripes resulted from secondary circulation originating in the test section and were not the result of the sediment feed arrangement or other upstream boundary conditions.

Sand stripes have been observed by previous field and flume studies and have been shown to result from secondary currents caused by instabilities introduced by the sidewalls and/or the erodible bottom (McLean, 1981; Ikeda, 1981; Colombini, 1993). McLean (1981) demonstrated that the secondary circulation associated with sand stripes could result from the roughness difference between the sand stripes and the intervening coarse material. Colombini (1993) and Colombini and Parker (1995) concluded that the secondary circulation could be caused either by a roughness difference or by an elevation difference between the elevated stripes and the bare bed. The barchan dunes that we observed sometimes occurred in combination with sand stripes (e.g. segment 4A), and sometimes occurred in isolation (e.g. segment 4D).

The width and number of sand stripes varied among the run segments in which these were the dominant bed form. Following run segments 1A, 2A, and 3A, there were 6 to 8 stripes that were spaced approximately evenly across the width of the channel (Figure 3.6). The number of stripes and the average width of the stripes decreased during the sediment evacuation segments of each run. As the number of stripes decreased, some of the stripes persisted while others decreased in width and eventually disappeared. The average height of the stripes that persisted decreased slowly while the height of the stripes that eroded decreased more rapidly. Most descriptions of sand stripes in the literature report stripe spacing of between the flow depth (Columbini and Parker, 1995) and twice the flow depth (Wolman and Brush, 1961; Culbertson, 1967; McLean, 1981). McLean (1981) used a perturbation model to predict that maximum secondary circulation occurred with stripe spacing of approximately $4h$. We observed spacings between stripes ranging from $0.5h$ (Run 1A) to $4.5h$ (Run 1D). McLean (1981) suggested that observed deviation from stripe spacing driven by secondary circulation may result from different initial conditions or the distribution of roughness irregularities on the bed. However, in

these experiments, the roughness elements were uniformly distributed and identical initial conditions and flow depths produced different stripe spacings for different rates of discharge and sediment feed. In all cases, we observed fewer stripes as the sediment supply diminished. This suggests that, while secondary circulation plays a role, actual spacing between sand stripes may be more strongly related to the sediment supply than bed irregularities or flow depth.

Although the distribution of the barchans can not be described by simple transverse spacing like the stripes, their behavior as the sediment supply diminished was similar to that of the stripes. In Run 4, which was the only run in which barchans occurred in all segments, the number and size of barchans decreased as the sand supply diminished.

Prediction of bed state

The assemblage of bed forms, or the bed state, in sandy sediment can be classified by grain size and one or more measures of flow strength, such as flow velocity, boundary shear stress, or depth (e.g. Allen, 1984; Southard, 1991; Best, 1996). These classifications have been developed for unisize sand transported at capacity over a full sand bed. In these conditions, the observed bed forms achieve a configuration with stable mean geometry. These classifications typically distinguish among ripples, dunes, plane bed, and anti-dune bed states. Some researchers have specifically examined bed configurations for coarse sediments (Carling, 1999) and sediment mixtures (Chiew, 1991). Recently, Kleinhans et al. (2002) investigated sand ribbons (stripes) and barchan dunes occurring in partially mobile conditions for mixed sand-gravel sediments in flumes and natural rivers. They found that these bed forms plotted within the dune regime of the bed-state stability diagrams of Southard and Boguchwal (1990), Chiew (1991), and Van den Berg and Van Gelder (1993), but that these diagrams could not be used to distinguish among barchans and sand stripes. Kleinhans et al. (2002), therefore, proposed a modified stability diagram that included the thickness of the layer of transported sediment as a parameter representing the relative proportion of mobile sediment. They concluded that dunes, barchans, and sand stripes occur on a continuum of decreasing availability of

mobile sediment. Figure 3.9 shows the data of Kleinhans et al. (2002) and the data collected in this study overlain on the bed-state stability diagram of Southard (1991). Both data sets include sand stripes and barchans, but the differing size of the transported material causes them to plot in different stability regions. In the data reported by Kleinhans et al. (2002), the sand stripes plot in the transition between ripples and dunes and the barchans all plot in the dune region. In contrast, both the stripes and barchans observed in this study plot in the ripple field. Thus, in a traditional stability diagram different partial sand cover bed states occur within a single stability field and similar partial bed cover configurations can occur in multiple stability fields.

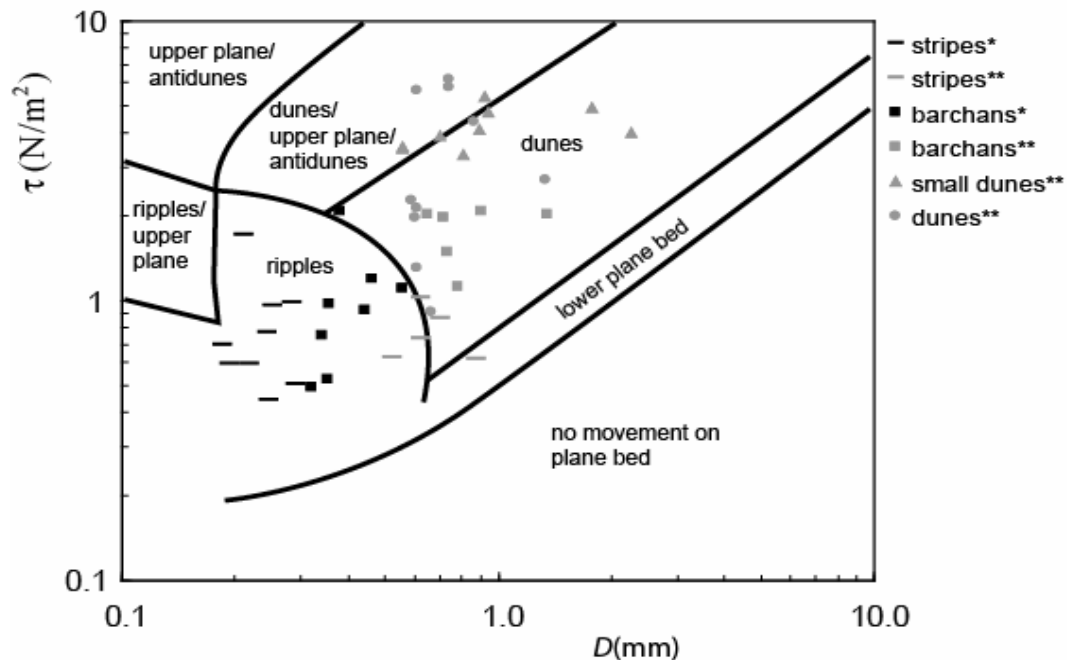


Figure 3.9. Bed-state diagram showing the stability fields identified by Southard (1991). Symbols marked (*) in the legend indicate data collected in this study. Symbols marked () in the legend are data reported by Kleinhans et al. (2002) and includes data from Bennett and Bridge (1995), Blom et al. (2000), Carling et al. (2000), Dinehart (1992), Horton et al. (2000), Hirano and Ohmoto (1988), and McLelland et al. (1999).**

Kleinhans et al. (2002) proposed a stability diagram in terms of the bed sediment mobility and a measure of the volume of mobile sediment. The bed sediment mobility is expressed by the dimensionless grain stress τ^{*} given by

$$\tau^{*} = \frac{\tau'}{(s-1)\rho g D_{50}}, \quad (3.5)$$

where τ' is the grain stress, $(s-1)$ is the submerged specific gravity of the sediment, ρ is the fluid density, g is gravitational acceleration, and D_{50} is the grain size of the mobile sediment. The volume of mobile sediment is represented by the average sediment thickness z_s , scaled by the flow depth h . The average sediment thickness is defined as the average depth that would result if all the mobile sediment were distributed evenly over the bed. The flow depth was chosen as a scaling parameter because dune height typically scales with flow depth.

The bed configurations that we observed do not plot in the same space of the stability diagram proposed by Kleinhans et al. (2002) (Figure 3.10). We observed sand stripes in the range of dimensionless grain stress and sediment supply conditions that Kleinhans et al. (2002) observed dunes. Although, the dimensionless grain stress is frequently used to distinguish between the stability fields of ripples, dunes, and plane beds, it is of limited utility in distinguishing among the bed forms that occur when mobile sediment partially covers the bed and those that occur when the bed is fully covered by mobile sediment. Flow strength is probably not an effective predictor because the limited supply of mobile sediment does not permit the development of the bed forms that would occur on a bed composed entirely of mobile sediment. The differentiation among the bed states identified by Kleinhans et al. (2002) is related mainly to the relative thickness of the transport layer.

We have modified the stability diagram of Kleinhans et al. (2002) by using boundary Reynolds number as the ordinate and by scaling the thickness of the mobile sediment with the size of the immobile grains. Since starved bed forms are unlikely to grow large, flow depth (which limits dune height) is not likely to be of great importance. Instead, the volume of mobile sediment, expressed by z_s , can be scaled by the size of the

immobile grains r_b , which will describe the degree to which the mobile sediment covers the bed substrate. The dimensionless shear stress has been substituted with a different dimensionless variable, the boundary Reynolds number R^* , defined as

$$R^* = \frac{u_*' D_{50}}{\nu}, \quad (3.6)$$

where ν is the kinematic viscosity of the fluid. The observations from the main channel experiments and the data reported by Kleinhans et al. (2002) are shown plotted in this modified stability diagram in Figure 3.11. This illustrates that the volume of mobile sediment, as represented by the average thickness of the mobile sediment layer, and the near-bed hydraulic regime, as represented by the grain stress and mobile sediment grain size, are factors that distinguish among configurations for partial sand cover. The data indicate a consistent progression from sand stripes to isolated barchans to full dunes. Transition along this progression can occur either in response to increasing supply of mobile sediment or, in the case of the transition from stripes to barchans, a change in the flow dynamics with respect to the mobile sediment. For similar conditions of sediment supply, sand stripes occur in a smooth flow regime relative to barchans. The transition from stripes to barchans occurs in the same general range of flow conditions as the transition from dunes to ripples. However, the transition is also a function of sediment supply and occurs at higher R^* for conditions of less sediment supply. Increases in bed stress and grain size, even during decreasing supply, can result in a transition from a stripe-dominated bed configuration to a barchan-dominated configuration.

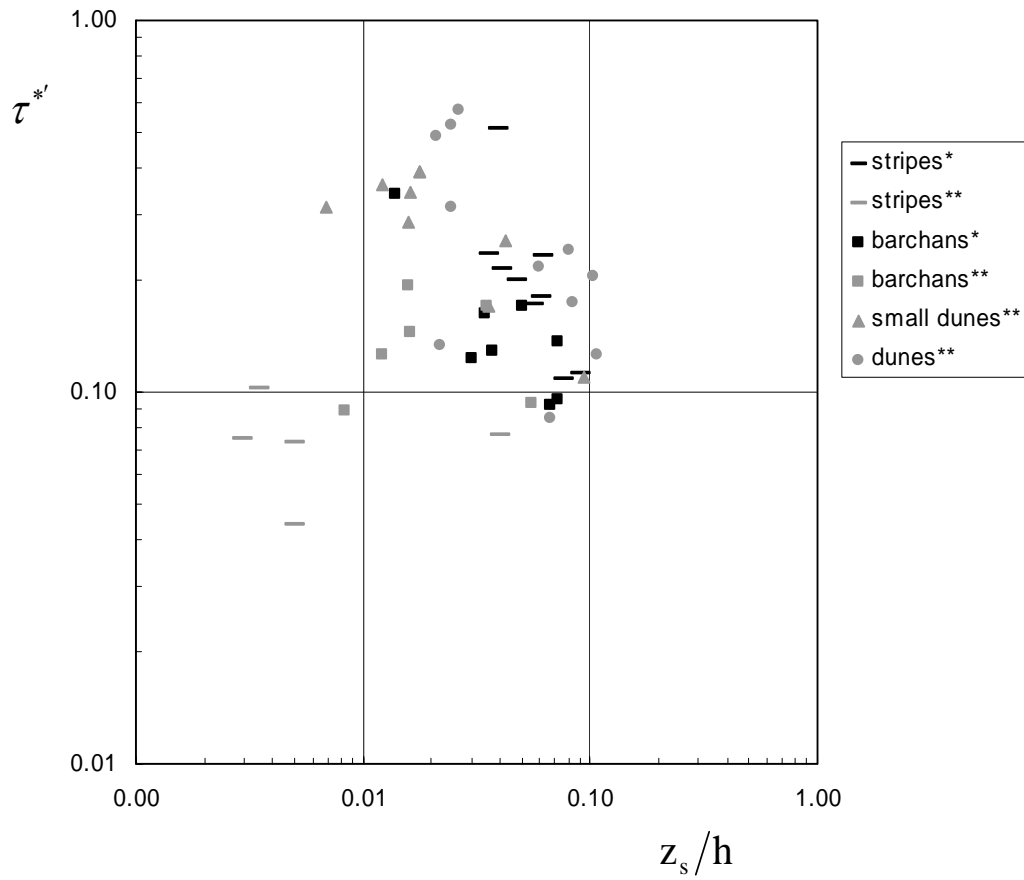


Figure 3.10. Bed-state stability diagram modeled after that proposed by Kleinhans et al. (2002). Symbols marked (*) in the legend indicate data collected in this study. Symbols marked () in the legend are data reported by Kleinhans et al. (2002) and includes data from Bennett and Bridge (1995), Blom et al. (2000), Carling et al. (2000), Dinehart (1992), Horton et al. (2000), Hirano and Ohmoto (1988), and McLelland et al. (1999).**

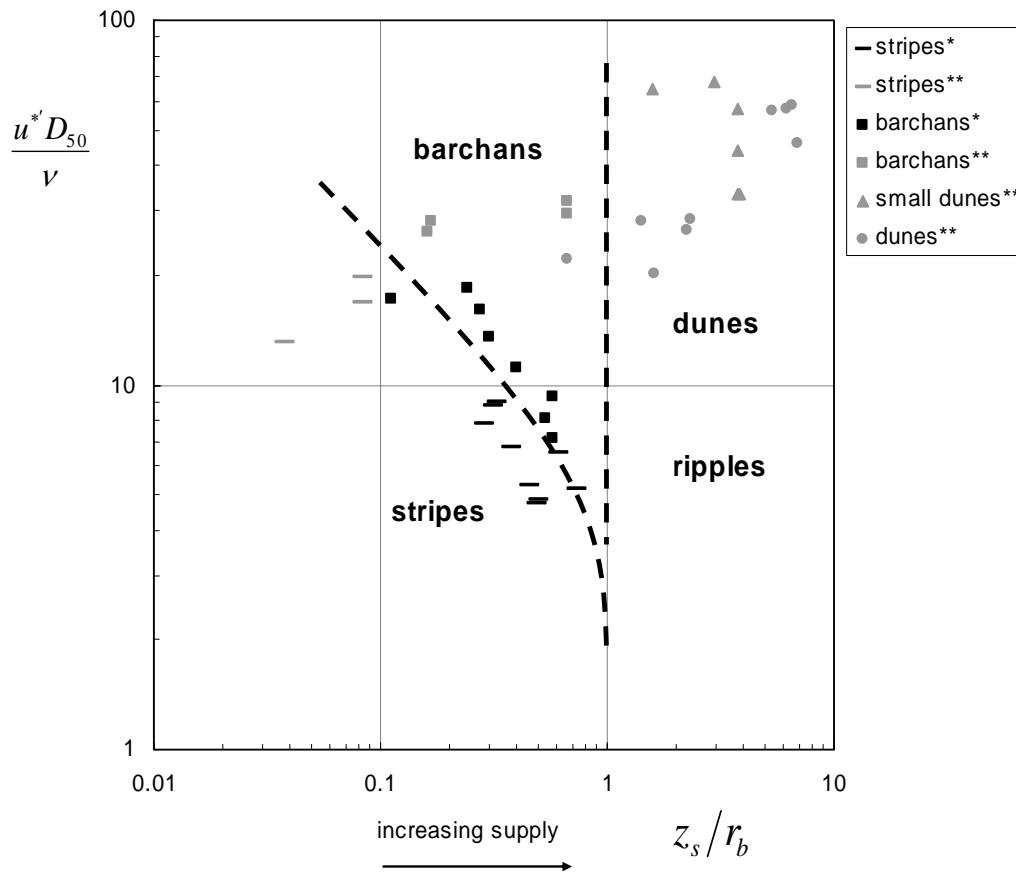


Figure 3.11. Proposed bed-state stability diagram. Symbols marked (*) in the legend indicate data collected in this study. Symbols marked () in the legend are data flume and field data collected and reported by Kleinhans et al. (2002).**

Bed sediment mixing depth

The nature of sediment mixing within the bed is of critical importance to modeling sediment entrainment and predicting bed morphodynamics. As the bed is eroded or aggraded, the exchange of sediment between the bed and the transport field must be considered to predict the evolving bed surface grain size and transport (Hirano, 1971). The traditional approach to this problem is to divide the bed into two or more layers (Hirano, 1971). The layer of active exchange is usually defined as the active layer. The thickness of the active layer is also referred to as the mixing depth. The active layer is assumed to be well-mixed in numerical models of morphodynamics. All size fractions within the active layer are, therefore, available for entrainment into suspension in

proportion to their presence in the grain size distribution. For plane-bed gravel transport, the mixing depth is usually represented by the diameter of the largest particles comprising the bed surface. For migrating dunes, the mixing depth is generally taken to be approximately 0.5Δ , where Δ is the dune height (Blom, 2003). By this definition, all of the sediment that participates in dune migration is included in the mixing layer. In the case of the partially sand-covered bed, both of these approaches may be considered. The mixing depth should include all of the fine sediment that participates in the formation and migration of the bedforms. Fine sediment in the interstices of the immobile roughness elements should also be within the mixing layer.

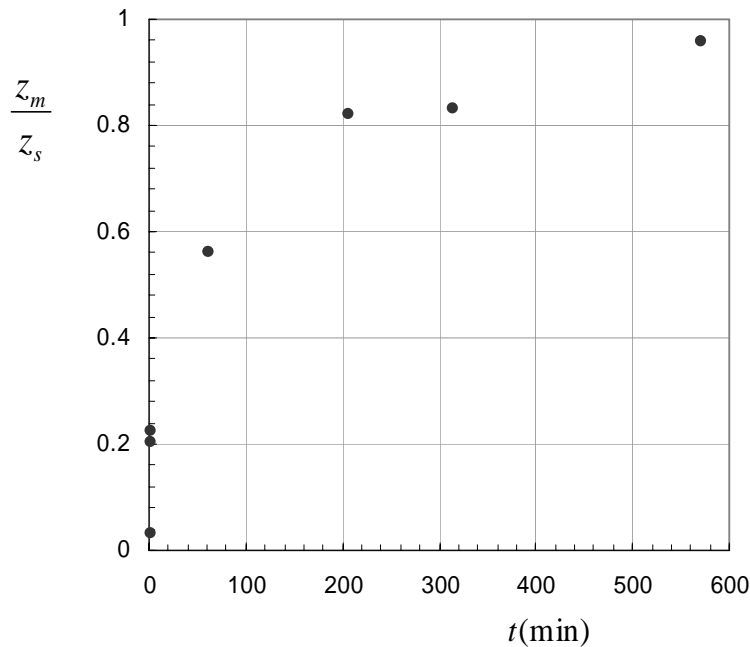


Figure 3.12. Mixing depth z_m normalized by total sand depth z_s as a function of time following the addition of colored sand at the conclusion of the feed segment of each run. Colored sand was added for last 1 min of each feed segment.

We added colored sand to the sediment feed for a period of 1 to 2 min at the conclusion of the feed segment for each run to examine the mixing depth in our experiments. We can also evaluate the mixing of the feed sand with the initial bed for Runs 3 and 4, because the feed sand and the sand used to seed the bed were different colors. Figure 3.12 shows the mixing depth scaled by the total sand thickness plotted as a

function of time following the addition of the colored sand. Mixing depths following the 1 to 2 min. of feed were typically about 1 cm or less. The colored sand was incorporated to greater depths in the bed with increasing run time. By approximately 10 hrs of run time, mixing occurred to nearly the entire sand depth.

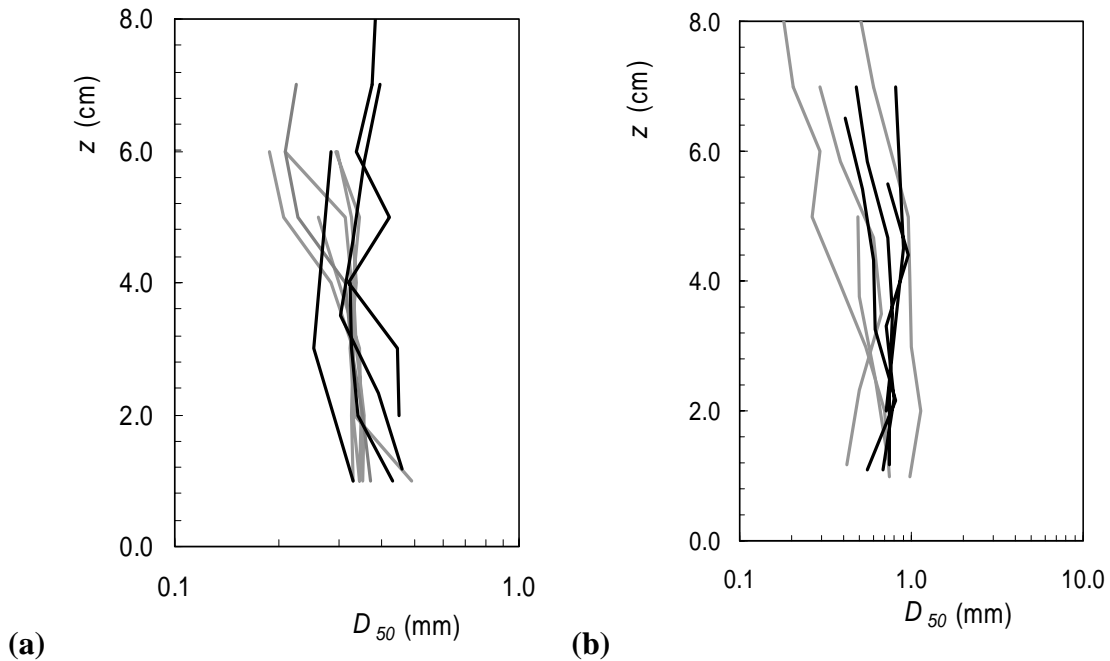


Figure 3.13. Grain size variation in sediment cores comparing Run 3A with Run 3D (a) and Run 4A with Run 4D (b). In each plot, the gray lines are from cores collected following the first run segment and the black lines are from cores collected following the “D” run segment. Each individual line is from a separate core sample. Samples were collected at similar locations in each run segment.

Grain size sorting within the bed is also an important characteristic of the active layer. If the bed is highly sorted, it may be necessary to use a smaller mixing depth, requiring a complex multi-layer or probabilistic treatment (Parker et al., 2000) of the bed for application in a sediment transport and routing model. If the bed sediment is well-mixed, a simple active layer approach may be justified. Figure 3.13 shows the evolution of the bed grain size profile measured by sediment cores collected from bed forms. Both Run 3 and Run 4 started with a well-mixed coarse bed that was approximately 4 cm ($0.5r_b$) thick. The sediment feed was fine sand that caused initial upward fining in the

grain size profiles. As these runs progressed, the feed sediment was incorporated in the bed sediment resulting in well-mixed profiles. In Run 3, mixing occurred down to about $0.5z_s$, while in Run 4, which was conducted at a higher flow rate, the entire depth was well-mixed. Figure 3.14 shows an example of a poorly mixed profile following the feed segment and a well-mixed profile collected from a nearby location later in the Run.

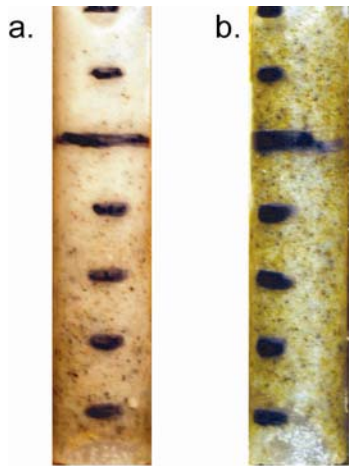


Figure 3.14. Photographs of sediment cores from Run 4a (a) and Run 4c (b). The white sand is the fine sediment feed ($D_{50} = 0.13$ mm) and the brown sand is the coarser sand that was used for the initial bed ($D_{50} = 0.34$ mm). Both cores were collected 27 m from the downstream end of the test section in center of channel. The tick marks are at 1 cm intervals and each core is 7 cm deep.

The sediment cores and grain size profiles indicate the bed was well-mixed to depths of about 7 cm, which is approximately equivalent to the bed roughness height of 7.5 cm. While for these conditions it seems that the mixing depth does scale with the bed roughness height, our experiments included only a single immobile grain size, and the extension of this scaling to mixed size roughness can not be tested.

Sediment transport field

Suspended sediment concentrations increased during the feed segment of each run and decreased during each of the evacuation segments (Figure 3.15). There was an increase in concentration during the final segments of Runs 2 and 3 when the flow rate was increased. During the evacuation segments, the deposit in the upstream accumulation zone deflated by entrainment of sediment into suspension. Although some

migration of the downstream margin of the deposit occurred, the rate of sediment movement on the bed was slow relative to the rate of transport in suspension.

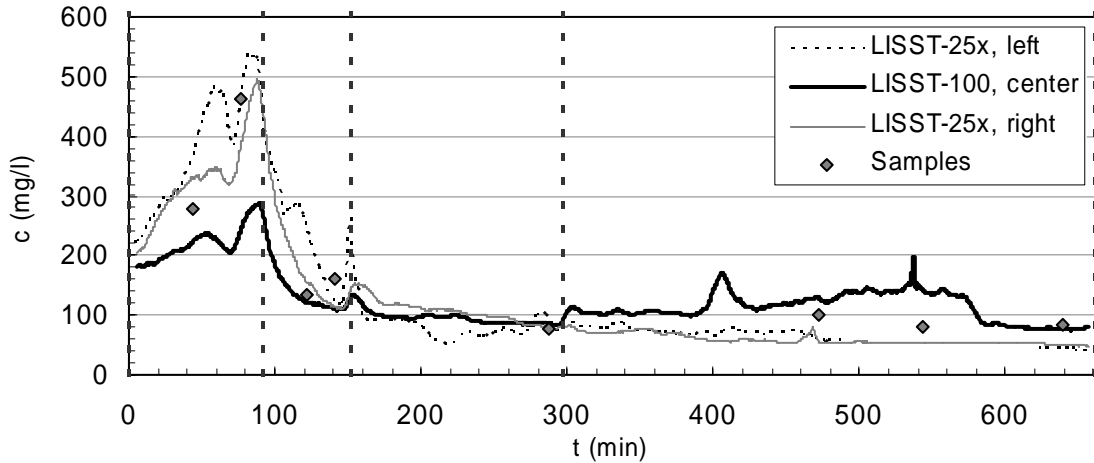


Figure 3.15. Time series of suspended sediment concentrations measured by laser-diffraction instruments for Run 1. The instrument labeled “left” was positioned 45 cm from the left flume wall; the instrument labeled “center” was positioned 137 cm from the left flume wall; and the instrument labeled “right” was positioned 227 cm from the left flume wall. The sampling volume of the LISST-100 was positioned 11-16 cm above the hemispheres. The sampling volume of the LISST-25x’s were positioned 5 cm above the hemispheres. The plotted siphon samples are the average of samples collected 6 cm above the hemispheres from the three transverse positions. The vertical dashed lines indicate the breaks between segments of Run 1.

The measurements of bed topography made at the conclusion of each run segment were used to estimate segment-average transport rates based on the bed sediment mass balance. The segment-average transport rate was calculated as the change in bed storage during the segment subtracted from the input volume for the run segment. These estimates of transport are compared to the measured rates of transport in suspension collected by siphon samples (Figure 3.16). For most of the run segments, the transport measured in suspension is approximately equivalent to the segment-average transport rate determined by the bed sediment mass balance. For the largest transport rates, the measured rate of transport in suspension exceeded the segment-average transport determined from the mass balance. This discrepancy is likely the result of comparing measures of transport that are averaged over different time intervals and uncertainty in

the mass balance, which did not account for sediment that leaked into the system. The movement of sediment out of the accumulation zone by diffusion rather than bed form translation is consistent with observations of sediment pulses reported by Lisle et al. (1997) and Cui et al. (2003).

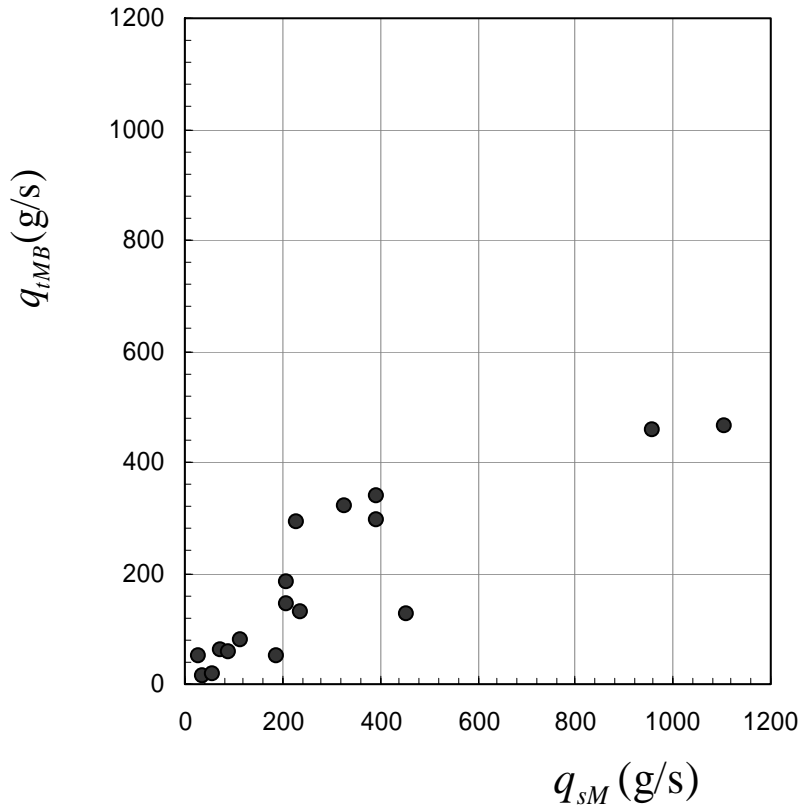


Figure 3.16. Comparison between the rate of transport in suspension as measured by the samples collected by siphon q_{sM} and the run segment-average rate of sediment transport as determined by bed-sediment mass balance q_{tMB} .

In most of the run segments, the sand stripes or barchans were distributed uniformly across the channel. In these segments we did not detect significant cross-channel variation in suspended sediment transport rates. However, we did observe cross-channel variations in sediment concentrations in runs that had nonuniform lateral distribution of bed forms. Figure 3.17 shows the variation in suspended sediment concentration among the three siphon rakes for run segments 1C, and 1D, 2A, and 4A. In run segments 2A and 4A, the bed forms are distributed uniformly across the channel

(Figure 3.6), and the concentrations are similar across the channel. In segments 1C and 1D, the sand stripes are concentrated in the center of the channel, where suspended sediment concentrations are highest.

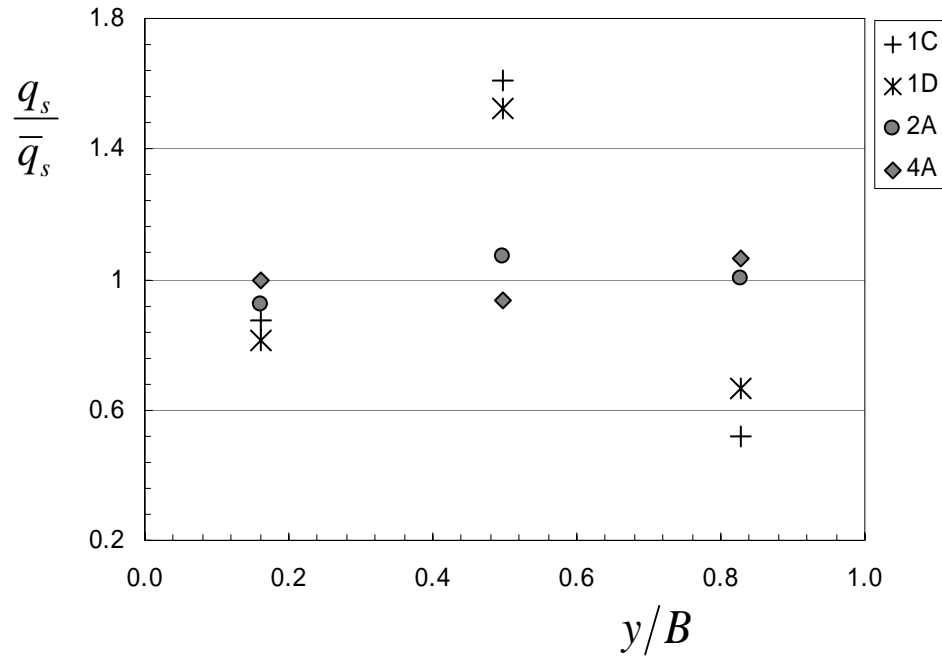


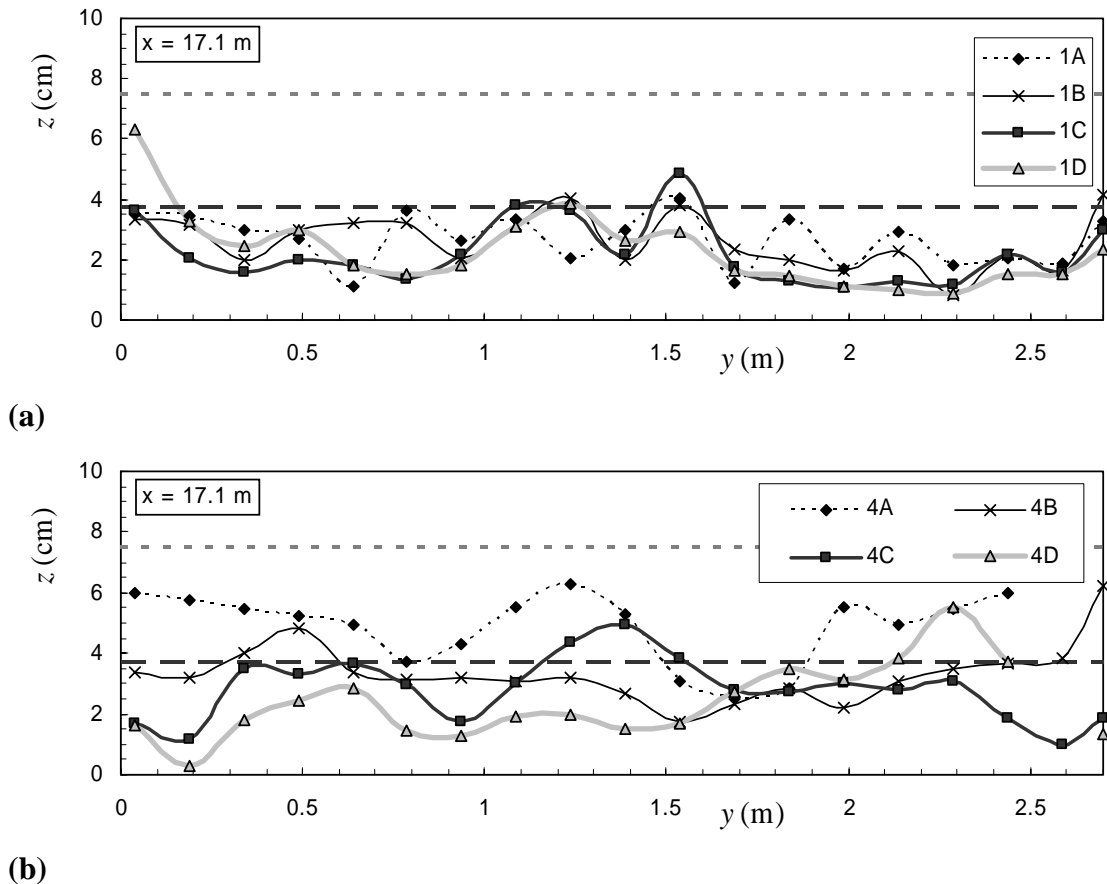
Figure 3.17. Cross-channel variation in suspended sediment transport rates. q_s is the transport for a single siphon rake and \bar{q}_s is the average transport for the three siphon rakes. y is distance from left side of channel B is channel width.

Predicting the distribution of sand patches

These experiments have demonstrated that as sediment is evacuated from a bed with a coarse substrate, the mobile sediment organizes into distinct bed forms separated by areas with thin deposits of fine sediment in the interstices. Collectively, the barchan and stripe bed forms may be referred to as sediment patches. The distributions of sand bed elevations (Figure 3.8) are similar for runs with different characteristic bed forms and different volumes of sediment in storage. This regularity of the distribution of sand bed elevations can be used to construct a model that predicts the spatial extent of sand patches based on the average thickness of the transported sediment layer. Such a model may be

useful for predicting bed state in a sediment routing model, or for estimating the sediment volume from images of the bed surface.

To examine the bed topography in detail, cross-sectional profiles of sand-bed elevation were constructed by averaging the sand depth measurements for each cross-stream position in 4.7 m segments along the length of the flume (see Appendix F for plots of all profiles). These profiles show that as the storage of sediment in the bed decreased, the sand stripes decreased in width, number, and elevation (Figure 3.18a). The stripes that persisted throughout the sediment evacuation remained nearly stationary in position as they shrank in size. Although the barchans were not stationary, they also consistently decreased in size as the supply diminished (Figure 3.18b).



(b) **Figure 3.18. Channel cross-section profile of measured sand bed elevations. The dashed line indicates the elevation of the hemisphere tops. Each plot contains the average of all measurements made in the 4.7 m bed segment that is centered 17.1 m upstream from the downstream end of the test section. y is distance from left sidewall and z is elevation above the bed at the base of the hemispheres. Run 3 (a) was dominated by sand stripes and Run 4 (b) was dominated by barchan bed forms.**

The sand bed elevations were analyzed systematically to determine relations for the average elevation of the sand in patches \bar{z}_p and the average elevation of the sand between patches \bar{z}_b . Within each 4.7 m segment, each measured sand bed elevation z_s was compared to the average sand bed elevation \bar{z}_s for the same segment. In order to determine the mean elevation of sand in patches and between patches, it is necessary to define a threshold separating patch and non-patch areas of the bed. This threshold was defined as the minimum patch elevation z_p . Values of $z_s \geq z_p$ were defined as belonging to sand patches and values of $z_s < z_p$ were defined as belonging to non-patches. The minimum sand patch elevation was determined by inspection of the distributions of sand bed elevations and the cross-section profiles. Nearly all of the frequency distributions of sand bed elevation include either one mode with a broad shoulder or two distinct modes. In both cases, the transition from the first mode to the second mode (or shoulder) occurs at sand elevations of between 3 and 4 cm (Figure 3.8). Similarly, most of the bed forms visible on the cross-section profiles were larger than 3 or 4 cm in elevation. Thus,

$$z_p = 0.5r_b \quad (3.7)$$

was chosen as the threshold elevation for defining a sand patch. Figure 3.19 shows all measured sand elevations in patches and non-patches plotted as a function of \bar{z}_s . Using this threshold, \bar{z}_p and \bar{z}_b were calculated as the average of the patch and non-patch elevations, respectively, in each 4.7 m bed segment. These data compiled from all run segments were used to construct relations for \bar{z}_p and \bar{z}_b . For the sand patches

$$\frac{\bar{z}_p}{r_b} = \begin{cases} \omega(1 + e^{(\alpha \hat{z}_s)}); & \hat{z}_s < 1 \\ 0.94\hat{z}_s + 0.12; & 1 \leq \hat{z}_s < \hat{z}_m \\ \hat{z}_s; & \hat{z}_s \geq \hat{z}_m \end{cases} \quad (3.8)$$

where $\omega = 0.5z_p$. This function was defined to fit the observations of \bar{z}_p , with the additional constraints that $\bar{z}_p \geq z_p$ and that $\bar{z}_p/r_b \rightarrow \hat{z}_s$ as $\hat{z}_s \rightarrow \hat{z}_m$, where $\hat{z}_m = z_m/r_b$ and z_m is the maximum sand bed elevation for which the bed is divided into sand patches and non-patches. For average sand elevations above z_m , the bed is completely sand

covered. As sand cover on the bed increases, the bed approaches a full sand condition and patches no longer exist, the average patch elevation and the average elevation become equivalent. The data that we have for the average patch elevation in each bed segment indicates that z_m is between r_b and $2r_b$ (Figure 3.19). The only change required in equation (3.8) is that for $z_m = r_b$, $\sigma = 1.1$ and for $z_m = 2r_b$, $\sigma = 1.2$.

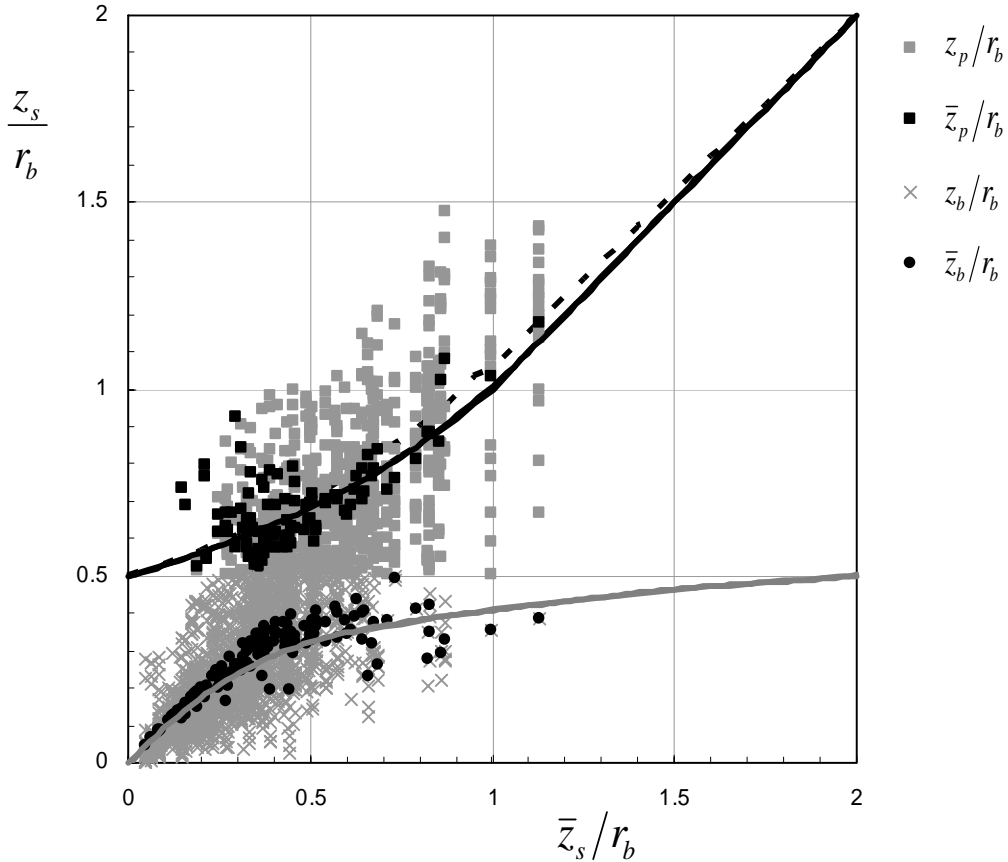


Figure 3.19. Sand bed elevation z_s as a function of mean sand bed elevation \bar{z}_s for the 4.7 m bed segment associated with each measurement. All data are scaled by the height of the immobile grains r_b . The data in gray are all the individual measurements of z_s in sand patches z_p and between patches z_b , respectively. The data in black are the average of the measurements in sand patches and between patches for each bed segment. The dashed black line is the modeled mean sand patch elevation assuming $\hat{z}_m = 2$ and the solid black line is the modeled mean sand patch elevation assuming $\hat{z}_m = 1$ (Eq. 3.6). The gray line is the modeled mean between patch elevation (Eq. 3.7).

The average elevation of sand between the sand patches was defined for the range of observations as

$$\frac{\bar{z}_b}{r_b} = \begin{cases} 0.85\hat{z}_s; & \hat{z}_s < 0.27 \\ 0.13 \ln(\hat{z}_s) + 0.41; & 0.27 \leq \hat{z}_s < 2, \\ \bar{z}_p/r_b; & \hat{z}_s \geq 2 \end{cases} \quad (3.9)$$

using the constraints that $\bar{z}_b/r_b \rightarrow \hat{z}_s$ as $\hat{z}_s \rightarrow 0$ and that $\bar{z}_b/r_b \rightarrow \bar{z}_p/r_b$ as $\hat{z}_s \rightarrow \hat{z}_m$.

Equations (3.8) and (3.9) provide an estimate of the average sand elevation in sand patches and the average sand elevation between patches if the sand elevation averaged over the entire bed is known. If the geometry of the immobile grains is known, these quantities can be used to determine the proportion of the bed sediment that is stored in patches and non-patches. Let F_p be the proportion of bed sediment stored in sand patches (stripes or barchans), V_p be the volume of sediment per unit bed area for sand patches, V_b be the volume of sediment per unit bed area for non-patches, and V_t be the average volume of sediment per unit bed area for the channel segment. F_b is the proportion of bed sediment stored in non-patch areas such that

$$F_b = 1 - F_p. \quad (3.10)$$

If all of the sediment on the bed is assumed to belong to either a patch or non-patch region, the distribution between these regions is given by

$$V_p F_p + V_b (1 - F_p) = V_t. \quad (3.11)$$

Solving equation (3.11) for F_p ,

$$F_p = \frac{V_t - V_b}{V_p - V_b}. \quad (3.12)$$

If the geometry of the bed roughness is known, the volume of sediment in the bed for any given sand bed elevation can be determined. For 15 cm diameter hemispheres in closest packing arrangement, the volume of sediment in storage per hemisphere V can be calculated by the following polynomial approximations of the closed-form solution

$$V = \begin{cases} 7.39 \cdot 10^{-1} z^3 - 3.55 \cdot 10^{-14} z^2 + 3.51 \cdot 10^{-3} z, & \left\{ \begin{array}{l} z < r_b \\ z \geq r_b \end{array} \right. \\ 2.0 \cdot 10^{-2} z - 9.25 \cdot 10^{-4} \end{cases} \quad (3.13)$$

where z is the sand bed elevation and r_b is the bed roughness height. Equation (3.9) is given here in dimensional form with V in units of $\text{m}^3/\text{hemisphere}$ and z and r_b in units of m . Using equation (3.13), V_p and V_b can be expressed as functions of the average patch and non-patch elevations, \bar{z}_p and \bar{z}_b , respectively; and V_t can be expressed as a function of the average bed elevation for the channel segment.

The method described above can be used to estimate the proportion of the bed covered by sand patches F_p as a function of the average sand bed elevation. Figure 3.20 shows the result of this calculation for the geometry of the bed considered here compared to the area of sand measured from photographs of the bed. Within the range of observations, the predicted sand coverage compares well with the measured sand coverage. The steepness of the curve for average sand bed elevation greater than $0.6r_b$ depends entirely on the choice of z_m , the average sand bed elevation at which the bed roughness elements are completely buried.

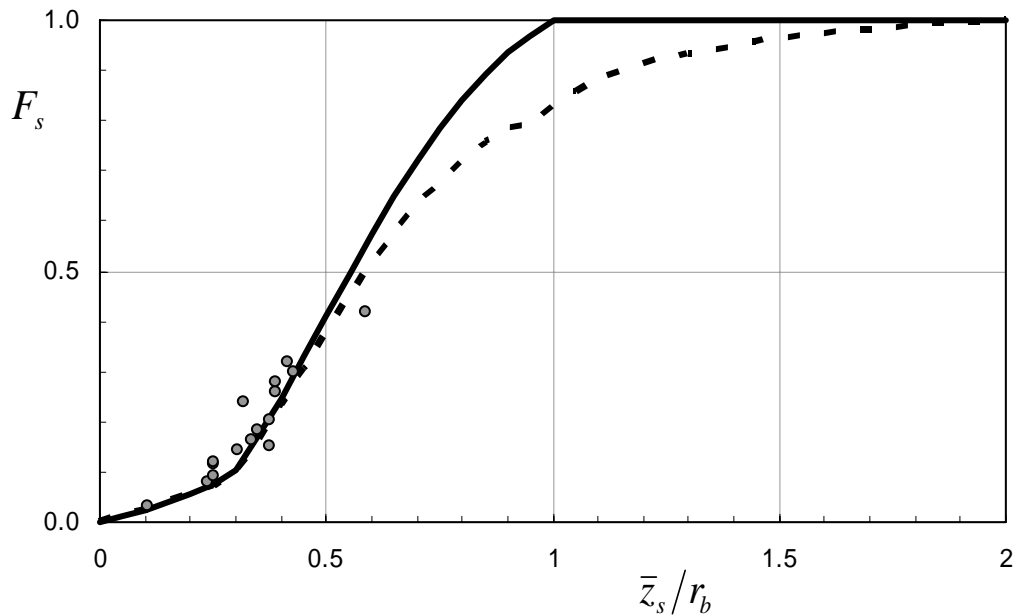


Figure 3.20. Fraction of bed covered by sand patch as a function of the spatially-averaged sand bed elevation. The points show the area of sand patches as measured from the post-run segment bed photographs. The line is the fraction of bed covered by sand patches modeled using Eqs. 3.6-3.11. The dashed line is for $\hat{z}_m = 2$ and the solid line is for $\hat{z}_m = 1$.

This model provides a simple method to calculate the fraction of the bed covered by bed forms or sand patches based on either the total volume of sediment in storage or the average sand bed elevation. The model could also be inverted to estimate the average sand depth or the volume of sediment in storage from observations of the spatial extent of sand patches. Further experimentation or field observations are required to better constrain the estimate of z_m .

Conclusions

Fine sand transported in suspension over coarse immobile grains forms a consistent sequence of bed forms as a function of the amount of sand in the system and the size of the mobile sediment. These bed configurations include flow parallel sand stripes and flow transverse barchan dunes, and are consistent with the bed forms that have been observed in other cases where the bed is partially covered by mobile sediment but where the transport is dominated by bed load (Carling, 1999; Kleinhans et al., 2002). A new bed-state stability diagram can be used to predict the transition from these isolated bedforms to a full sediment bed. The axes of the stability diagram are the boundary Reynolds number and the volume of the mobile sediment, expressed by the ratio of the average depth of the mobile sediment to the size of the immobile grains. In general, increasing the amount of available sediment results in a transition from sand stripes to barchans to fully developed dunes. However, because the near-bed hydraulic regime and degree of supply limitation are important in determining the bed state, other trajectories are possible. For example, if grain size and/or bed stress increases as supply decreases, which is a common occurrence in supply-limited conditions (Topping et al., 2000), one may observe a transition from sand stripes to barchans. This behavior could not be predicted with previous stability diagrams.

The division of the bed into patches of mobile sediment that nearly bury the immobile grains and patches with sand bed elevations less than one-half the bed roughness height is consistent with the findings reported in Chapter 2. In those experiments, we found that there existed a threshold between a fully sand covered bed and a partially sand covered bed. In 17 experimental runs, we had difficulty prescribing

conditions that resulted in average sand bed elevations greater than about 0.4 times the bed roughness height without forming sand patches. This indicated that the large grains cause decreased entrainment below elevations of about 0.4 to 0.5 times the bed roughness height and enhanced entrainment above that elevation range. In the Main Channel experiments, we did achieve average elevations in this range, but only because the averaging included both the patch and non-patch areas.

Mixing depth is on the order of the bedform height, which is the same order as the bed roughness height. Mixing depth on the order of bed roughness height is confirmed by observations of sediment mixing over the course of run segments. Under conditions of non-uniform transport (decreasing sediment supply and decreasing bed elevations), bed sediment is well-mixed to a depth approximately equivalent to the bed roughness height. Instantaneous mixing depths are much less and are on the order of 0.2 times the bed roughness height.

The elevation and volume of the sand in patches formed by sand stripes and barchans is predictable based on the bed roughness height and the average sand depth, or equivalently, the total volume of sand in the bed. This makes it possible to construct a simple predictive model for the fraction of the bed that is covered by sand patches as a function of the average sand bed elevation. This type of relation could be very useful in a numerical sand routing model. This may also have application in the inverse form, to estimate the depth and volume of sediment in storage based on areal measurements of the distribution of sand patches.

Chapter 4: Entrainment and non-uniform transport of sand in coarse-bedded rivers: Laboratory experiments and numerical model

Introduction

Background

The annual sediment load of many rivers consists largely of sand and finer material transported by a wide range of flows. In many cases, this fine sediment load is transported over a bed of coarse grains that are rarely or never mobilized. Some outstanding examples of rivers with this characteristic can be found in the canyons of the western United States. The mainstem rivers of this region, such as the Snake River, the Green River, the Colorado River, and the San Juan River all transport large annual loads of fine sediment supplied primarily by large mainstem tributaries that drain areas of highly erodible sedimentary rocks (Howard and Dolan, 1981). The delivery of sediment from these tributaries generally occurs during monsoonal thunderstorms and does not coincide with the snowmelt driven annual flood on the mainstem rivers. Segments of these rivers flow through narrow canyons in which local channel morphology is dominated by debris fans (Figure 4.1) that form at tributary junctions (Schmidt and Rubin, 1995; Grams and Schmidt, 1999). Debris fans are reworked by large mainstem floods and the coarse alluvium is redistributed to downstream gravel bars and the channel bottom (Webb et al., 1989; Larsen et al., 2004). The coincidence of abundant supplies of fine sediment and local supplies of coarse sediment results in a river channel with a coarse bed that is intermittently overlain by fine sediment. During extreme flow events capable of mobilizing the coarse fraction of the bed, most of the fine sediment is flushed downstream or deposited on the channel margins (Schmidt, 1999). However, during average flows that do not mobilize the coarse fraction of the bed, fine sediment is transported over the immobile bed, forming patches of fine sediment and partially filling interstitial spaces (Figure 4.2). Because many of these rivers are managed for water storage, hydroelectric power generation, or flood control, flows that mobilize the coarse component of the bed are rare. Transport of fine sediment, then, occurs primarily during moderate flows when the bed framework is immobile (Topping et al., 2000).



Figure 4.1. View of the Colorado River in Grand Canyon showing tributary debris fans and fine sediment stored in eddy bars on the channel margins.

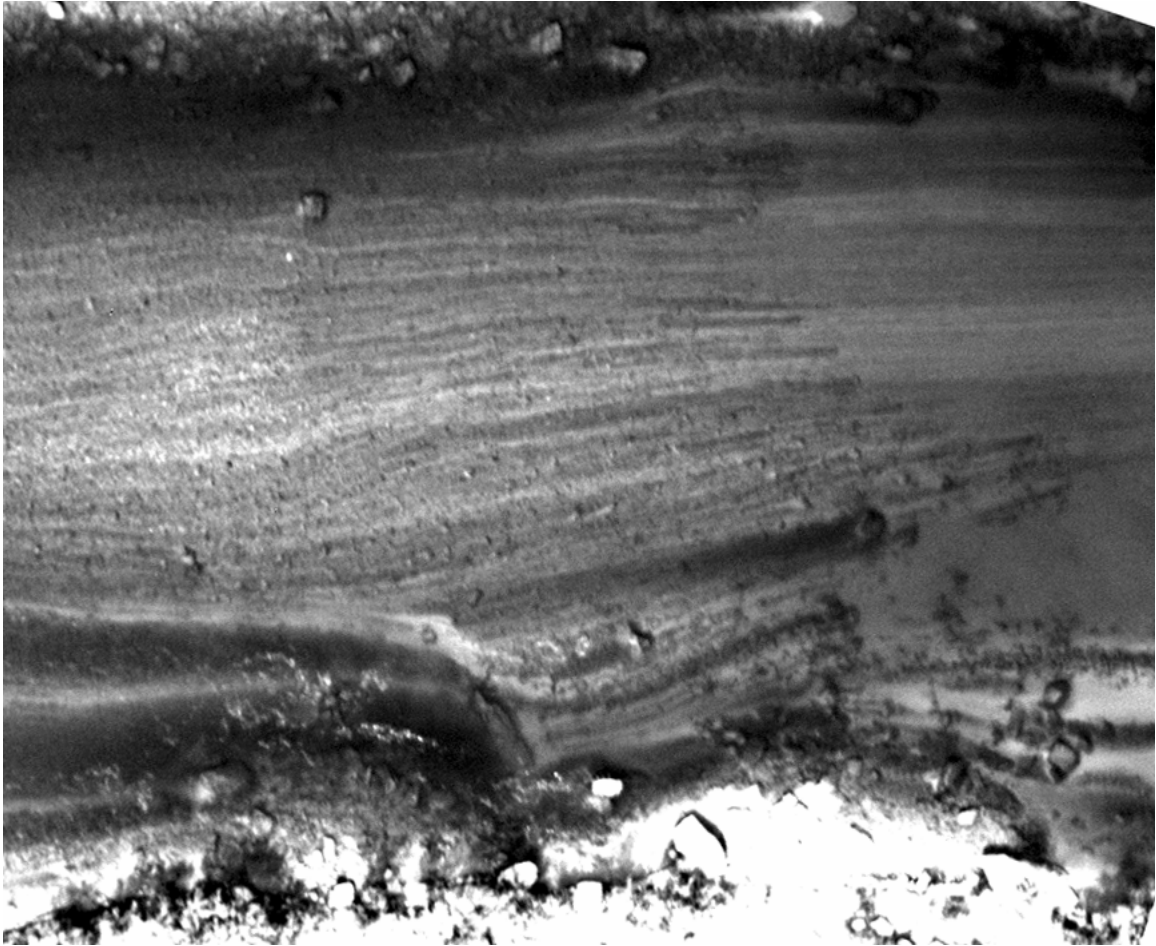


Figure 4.2. View of the bed of the Colorado River in Grand Canyon showing a coarse bed partially filled with fine sediment that is organized as sand stripes. Flow is from right to left.

Routing of the fine component of the bed material load (sand) through river systems is an important component in a wide range of geomorphic, engineering, and resource management applications. Fine sediment may be responsible for the creation and maintenance of important habitat for endangered native fish, form the substrate for riparian communities, and provide camping sites for recreationists in canyons where flat ground is often in short supply. Methods currently in use for predicting the entrainment and transport of fine sediment are appropriate for the case in which the bed and the transported material have the same size distribution. Less is known about the dynamics of sand transport over coarse immobile beds and no general formulation is available for sand routing in these conditions. In this paper we present a model for fine sediment

entrainment from a coarse immobile bed that is partially covered with fine sediment. A numerical sand routing model is developed from theoretical considerations and tested against laboratory measurements of sand transport over a coarse bed.

Controls on sand entrainment in a coarse-bedded river

For transport over a sand bed, the primary controls on the rate of sand entrainment are the bed stress and sediment grain size. When the bed sediment and the material in transport are exclusively fine-grained, bedforms typically develop; and several transport models account for their effect on the flow and transport field (e.g. Engelund and Hansen, 1967; Smith and McLean, 1977; McLean et al., 1999). Entrainment of sand from patches and interstices of a coarse immobile bed introduces two major complications to the entrainment problem. First, the large exposed grains will exert drag on the flow that will affect near-bed flow and stress distribution. Second, the elevation and spatial distribution of sand coverage among the immobile grains will alter the availability and mobility of the sand.

The estimation of the stress that leads to particle entrainment, the grain stress, is central in any sediment transport problem. However, grain stress is difficult to estimate precisely, and this difficulty is compounded by the interaction between large immobile grains and smaller mobile grains. The coarse grains exert drag on the flow and, depending on their size and packing arrangement, may carry most or all of the bed stress. Flow in the interstices over the mobile sediment will be strongly dominated by wakes shed by the coarse grains. The structure and intensity of the turbulent wakes is likely to vary depending on the elevation of the sand relative to the coarse grains, creating a complex relation between sand bed elevation and sand entrainment. These complex interactions between flow and sand entrainment can be integrated in a single sand elevation correction function ε whose exact form is not known, but whose limits can be specified. The sand elevation correction is the ratio of the observed rate of sand entrainment E_s from among coarse immobile grains to the rate of entrainment that would be predicted over a full sand bed \hat{E}_s :

$$\varepsilon = \frac{E_s}{\hat{E}_s}. \quad (4.1)$$

In Chapter 2, it was proposed that the sand elevation correction could be defined as a function of the normalized sand elevation among the coarse immobile grains \hat{z}_s ;

$$\hat{z}_s = \frac{z_s}{r_b}, \quad (4.2)$$

where z_s is the sand bed elevation and r_b is the height of the immobile grains. This function must go to zero as the bed becomes void of mobile sediment at $\hat{z}_s = 0$ and must go to one as the bed becomes covered with fine sediment at $\hat{z}_s > 1$. Small changes in \hat{z}_s near one would be expected to produce little change in ε until \hat{z}_s drops sufficiently low that wakes shed by the coarse grains cause accelerated entrainment. Similarly, we might expect little change in ε for \hat{z}_s near zero, because the interstitial sand is largely sheltered from the flow. Hence, the sand elevation correction is likely to take a sigmoidal or logistic shape.

A form for the sand elevation correction function was proposed in Chapter 2 based on data collected in equilibrium transport experiments in which the transport field was near equilibrium and measured near-bed concentrations could be used to approximate the entrainment rates. The shape of this sand elevation correction (SEC-1), shown by the bold line in Figure 4.3, suggests that entrainment rates are small relative to sand-bed conditions when the bed elevation is low. This implies that low sand bed elevations can be maintained by small entrainment rates over a coarse bed at flows that would produce much higher entrainment rates over a full sand bed. At slightly higher sand bed elevations, the rate of entrainment increases rapidly ($\hat{z}_s > 0.4$). This implies that as sand begins to accumulate on the bed, entrainment rate increases and effectively limits or precludes the further accumulation of sand in this intermediate range of bed elevations. Thus, bed elevations in this range might be unstable and infrequently observed. Finally, as sand elevations approach the height of the immobile grains, the entrainment rate approaches that of a full sand bed.

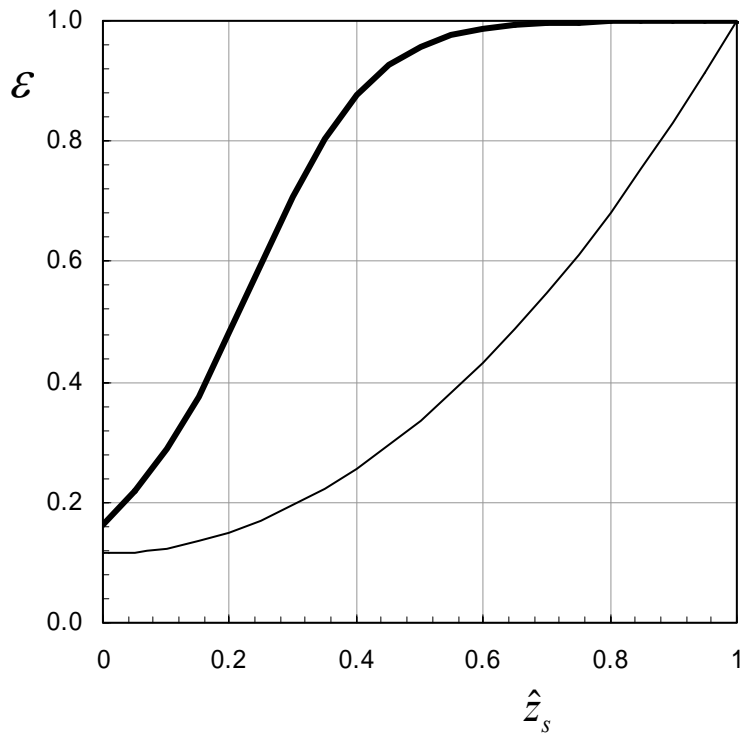


Figure 4.3. Sand elevation correction function ε . The function shown by the heavy black line is based on the data presented in Chapter 2 (SEC 1) ($\xi=12$, $Z^*=0.3$, and $\eta=0.5$). The function shown by the thin black line is based on the fraction of the bed covered by sand as a function of the average sand bed elevation for a uniform thickness of sand in a bed of closely packed hemispheres.

Another factor controlling sand entrainment is the proportion of the bed covered by sand. As \hat{z}_s decreases, the areal coverage of sand decreases. If sand entrainment depended only on the area of the bed covered by sand, as is commonly done for mixed-size transport models, the correction function would look like the thin line shown in Figure 4.3. The difference between the two curves indicates that factors other than aerial coverage of sand control sand entrainment.

The observations used to produce SEC-1 were made in a narrow flume that suppressed the development of sand patches. Spatially variable bed conditions, which were shown in Chapter 3 to be common for conditions of partial sand cover, may result in a different sand elevation correction. Thus, the difference between SEC-1 and the function that would exist if entrainment of sand was exactly proportional to the area of

sand on the bed may be due to the reasons discussed above or may be due to the limited range of bed configurations that existed in those experiments.

In a wide channel, partial sand cover does not result in a uniform thickness of sand among immobile grains. The sand bed organizes itself into bed forms that include sand stripes and barchan dunes (Chapter 3). These bed forms tend to have heights that are of the order of the immobile grains. Sand entrainment occurs from a mix of local bed conditions, which may be characterized as sand patches where $\hat{z}_s \approx 1$ and interstitial regions, or non-patches, where $\hat{z}_s < 1$. According to Figure 4.3, we might expect that non-patch areas of the bed with relatively small \hat{z}_s also have small ε , such that most of the entrainment, averaged over the entire bed, occurs from sand patches. If \hat{z}_s is calculated using the mean sand bed elevation across a spatially variable mix of sand patches and non-patches, then a value of $\hat{z}_s < 1$ would indicate that the sand in transport is derived from a mix of patch and no-patch areas, each of which would have different values of local ε . Although the actual form of this spatially averaged entrainment function is not known and would depend on the distribution of patch and non-patch areas, we can expect that it would not be the same as the entrainment function developed for the more spatially uniform conditions represented by the bold line in Figure 4.3.

Under spatially variable bed and transport conditions, it is not possible to estimate ε directly from observations of near-bed suspended sediment concentration. Hence, neither the local entrainment rates for patch and non-patch areas nor the spatially averaged entrainment rate for the bed can be determined directly. It is possible, however, to use observations of transport rate and bed cover in a partially covered, nonuniform transport field to test spatially averaged entrainment functions within a morphodynamic model for sand entrainment, transport, and deposition. The connection between spatially averaged entrainment and local entrainment from a spatially variable bed can also be examined in the context of observed distributions of local sand bed elevation.

Measuring non-uniform sand transport over a coarse bed

Experimental design

The laboratory flume experiments were designed to simulate the introduction and evolution of a sand pulse in a coarse-bedded channel, producing conditions of partial sand cover over immobile grains. The scaling properties and experimental conditions are identical to those described in Chapter 3, and are briefly summarized here. The most important scaling properties are those that determine the near-bed flow and sediment entrainment conditions and those that contribute to the development of a spatially variable bed configuration representative of natural conditions. To achieve the latter objective, the experiments were conducted in an experimental channel 2.74 m wide and 84 m long (the Main Channel at the St Anthony Falls Laboratory of the University of Minnesota), providing near field scale conditions.

The bed surface consisted of 15-cm diameter hemispheres arranged in closest-packing across the full width of the channel in a 40-m test section. The flow depth over the tops of the hemispheres was 60 cm for all runs, in order to allow a spatially integrated region in the flow above the near bed region and to provide sufficient depth for the development of a range of bed forms (Southard, 1991). Two flow rates were used, both of which produced Rouse numbers less than one such that the dominant mode of transport would be suspension, and Froude numbers less than one to ensure lower regime flow conditions and bed forms (Table 3.1). The bed slope was 0.0005 for all experimental runs.

Each experimental run included a 90-min feed segment followed by one to four additional non-feed segments (Table 3.2). Fine sediment with a median diameter of approximately 0.13 mm (Figure 4.4) was fed at the upstream end of the test section. The initial bed condition for Runs 1, 2, and 5 consisted of bare hemispheres. Prior to Runs 3 and 4, a layer of mobile sediment with a median diameter of 0.34 mm (Figure 4.4) was spread evenly to a thickness of 4 cm. The flow rates and sediment feed rates resulted in run segments of sediment accumulation and sediment evacuation.

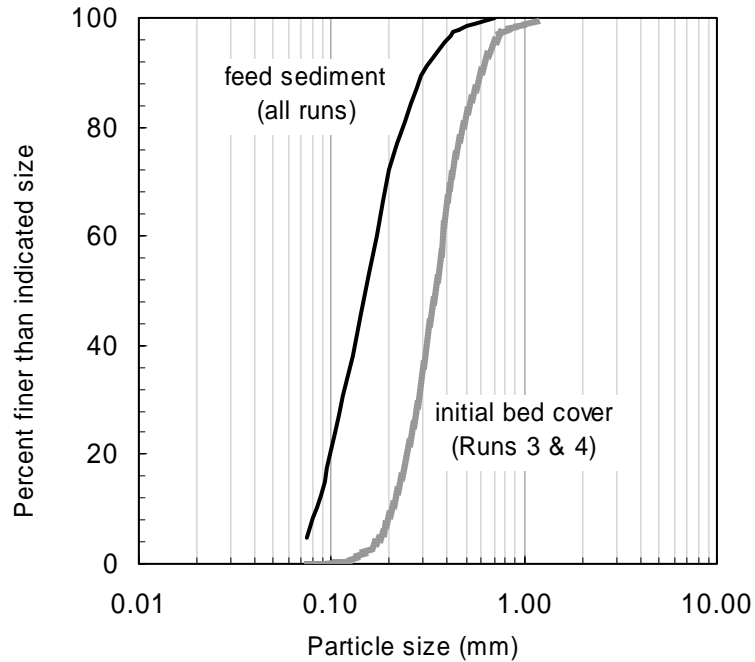


Figure 4.4. Size distribution of feed sediment and sediment used for initial bed cover.

Data collection

Flow measurements

Flow in this experimental channel is controlled by a motor-driven headgate that diverts water from the Mississippi River. This mechanism does not allow precise control of inflow volume, resulting in slightly variable flow rates between run segments (Table 3.2). The flow rate of each segment was measured by collecting outflow for a measured interval in large volumetric tanks.

To characterize the flow structure and the near-bed shear stress, velocity profiles were measured with an acoustic Doppler velocimeter (ADV). Each velocity profile included eight measurement positions located 1, 2, 3.5, 6, 10, 15, 25, and 40 cm above a hemisphere top. These profiles were measured at five cross-channel positions 45.5, 91.5, 137, 183, and 228.5 cm from the left sidewall, respectively. For the low flow conditions, measurements at all five cross-channel positions were made at six locations along the flume: 1.2, 3.0, 5.1, 7.0, 10.9, and 15.1 m upstream from the downstream end of the test section (hereafter, all streamwise positions are referenced by distance upstream from the

downstream end of the test section). Four additional velocity profiles were collected at the center channel position only at distances of 19.1, 23.0, 31.1, and 37.2 m in the test section. For the high flow condition, velocity profiles were collected at all five cross-channel positions at distances of 1.2, 3.0, 5.1, and 7.0 m in the test section. Center-position profiles were also collected at 10.9, 15.1, 19.1, 23.0, and 31.1 m. All measurements were made at sample rate of 50 Hz for 1 min. or longer with a SonTek 16 MHz MicroADV. This instrument has a sampling rate of up to 50 Hz and a velocity resolution of 0.01 cm/s up to 250 cm/s. Reported accuracy is 1% of measured velocity. The sampling volume is centered 4.67 cm below the probe tip and the sampling volume is 0.09 cc.

The ADV data were processed to remove spikes then analyzed for velocity profiles and turbulence characteristics (Appendix B). The turbulent Reynolds stresses were calculated from the ADV data as a shear velocity,

$$u^* = \sqrt{-\overline{u'w'}} \quad (4.3)$$

where,

$$\overline{u'w'} = \frac{\sum uw}{n-1} - \frac{\sum u \sum w}{n(n-1)} \quad (4.4)$$

and u is the instantaneous downstream velocity, w is the instantaneous vertical velocity, and n is the number of instantaneous measurements. Primes denote instantaneous deviations from the mean velocity $u' = u - \bar{u}$ and overbars represent time averages.

Suspended sediment sampling

Direct measurements of sediment concentration were made during each run segment by collecting samples via fifteen 3.18 mm i.d. stainless steel Pitot tubes. The tube inlets were positioned 5.17 m upstream from the downstream end of the test section in three cross-channel positions and at five elevations above the hemisphere tops. The sample tubes were connected to plastic tubing with outlets positioned outside the channel at an elevation such that the water velocity in the tube inlet matched the ambient stream velocity at that elevation in the channel. Three rakes of 5 tubes each were positioned 44,

136, and 227 cm from the left sidewall. Within each rake, tube inlets were positioned 1, 2, 6, 15, and 40 cm above the hemisphere tops. Samples were collected in 2 to 4 sample events in each run segment (Table 3.2). Sample durations typically ranged from 60 to 90 seconds, depending on the flow rate. Each sample was analyzed for suspended sediment concentration and selected samples were analyzed for grain size.

Measurement of bed topography and bed material sampling

Each run segment was concluded by shutting off the water supply and dropping a tailgate that completely stopped the flow in less than 30 s. This procedure was employed to stop transport as quickly as possible while preserving the bed configuration. The flume was then drained slowly while observing the bed to document minimal disturbance. This method was generally successful, and minor bed reworking was observed only in the downstream few meters of the test section. Once drained, the entire bed was photographed from above. The sand depth above the elevation of the base of the hemispheres was measured using a ruler at locations on a grid defined by 18 or 19 transverse positions and 34 streamwise positions at 1.2 m intervals (Figure 3.7). The transverse positions were at each interstitial gap between hemispheres. There are 18 gaps for even-numbered rows, which have a half-hemisphere on the edges of the channel and there are 19 gaps for odd-numbered rows, which have whole hemispheres on the edges of the channel. At each gap between hemispheres, a measurement was made in the interstitial space on the upstream and downstream side of the gap, forming a measurement pair. Measurements were made in this way to avoid bias towards interstitial spaces that are immediately downstream of either a hemisphere center or a gap between two hemispheres. The measurements were made in alternating odd and even-numbered rows to avoid bias in cross-stream position. A typical measurement set consisted of 630 measurement pairs, or 1260 individual measurements. The sand depth was measured to the nearest millimeter with a ruler constructed to fit in the interstitial spaces.

Experimental results

In the feed segment of each run, the channel aggraded throughout the length of the test section resulting in average bed thicknesses of approximately 2 cm (Run 5), 4 cm (Runs 1, 2, and 4), and 6 cm (Run 3). Deposition was always highest in an accumulation zone in the upstream 10 m where the hemispheres were largely buried (Figure 4.5). In most run segments, the spatial extent of sand coverage and the sand bed elevations decreased in the downstream direction. In Runs 1, 2, 3, and 5, sand stripes formed at the downstream end of the accumulation zone and extended throughout the rest of the test section. Following the feed segment of Run 4, the bed was covered by a mixture of sand stripes and isolated barchan dunes. The distribution of these bed forms and the conditions resulting in different bed conditions are described in Chapter 3.

During the non-feed run segments, the deposits in the accumulation zone slowly eroded. Some downstream migration of the deposit occurred, but the primary mechanism of erosion was entrainment into suspension (Chapter 3). The bed configuration also evolved during the evacuation run segments. In Runs 1, 2, and 5, sand stripes were the prevalent bed forms and the number of stripes decreased and the individual stripes became narrower as the sediment evacuated (Figure 4.5a). In Run 3, the stripes decreased in number and coalesced resulting in transitional sand stripe and barchan bed forms (Figure 4.5b). The mixed sand stripes and barchans that covered the bed following the first segment of Run 4, coalesced creating larger forms in the second segment. These bed forms then decreased in size and abundance in following segments (Figure 4.5c).



Run 1A



Run 1B



Run 1C



Run 1D

(a)



Run 3A



Run 3C

(b)



Run 4A



Run 4C

(c)

Figure 4.5. Photographs of bed at the conclusion of selected run segments (Table 3.2). In each image, the channel width is 2.74 m and the length is 40 m. The small white tabs along the top of each image are at 1 m intervals. Flow was from left to right.

Non-Uniform Sand routing Model

The proposed sand entrainment formulation was implemented in a morphodynamic numerical model designed to predict evolving sand bed elevations, grain size, and suspended sand concentrations under conditions of unsteady transport and nonuniform bed coverage. The main components of the numerical model include characterization of the vertical flow structure and bed stress, calculation of the sand entrainment rate for a full sand bed, application of a sand elevation correction function to account for partial sand cover, calculation of the vertical profile of suspended sediment concentrations, and conservation of sand mass to track the evolving sand bed coverage.

Characterization of streamflow and bed stress

The non-uniform transport experiments were conducted under conditions of steady uniform flow with constant fixed-bed roughness. We analyzed profiles of Reynolds stress, expressed as shear velocity normalized by depth-averaged velocity to examine the stress regime near the bed. The stress decreases linearly from the upper region down to approximately $0.10h$ above the hemispheres (Figure 4.6). From this height down to about $0.05h$, the mean shear stress is constant and equivalent to about $0.085U$. Closer to the bed, the measured Reynolds stress decreases. Voulgaris and Trowbridge (1998) reported that Reynolds stresses computed from ADV measurements within 3 cm of the bed deviate from expected flow characteristics while those computed above 3 cm were in good agreement. Expected flow characteristics were estimated with a statistical model using velocity records collected simultaneously by an ADV and a laser Doppler velocimeter. Other researchers have reported errors in ADV measurements near the bed resulting from shear within the sampling volume (Kim et al., 2000). Therefore, the Reynolds stresses measured within the short segment of constant stress are considered to be the most reliable estimate of average bed stress. Based on these observations, the bed stress for both flow conditions is approximated as a function of the depth-averaged velocity (Figure 4.6)

$$u_* = 0.085U . \tag{4.5}$$

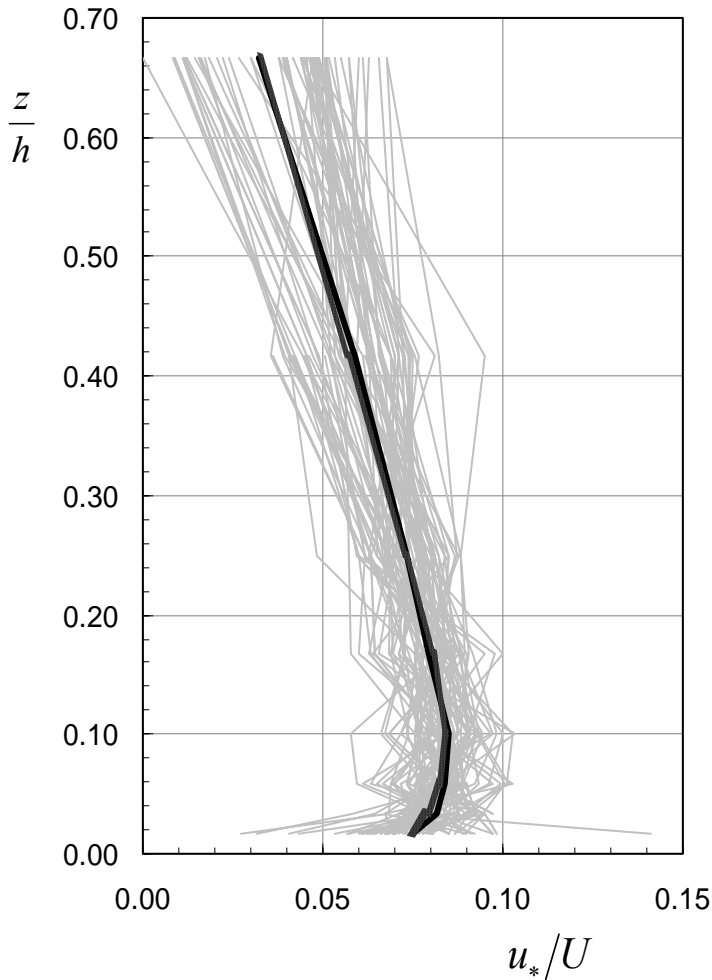


Figure 4.6. Plot showing normalized shear velocity u_*/U as function of normalized elevation above the bed z/h . The light gray lines show the individual measurements for all transverse and downstream positions at both low and high flow rates. The heavy shaded line is the average among all measurement positions for the high flow rate and the heavy black line is the average among all measurement positions for the low flow rate.

The nonuniform transport model requires specification of the velocity profile to compute the profile of suspended sediment concentrations. The velocity profile was observed to be consistent at all transverse and alongstream positions and a mean profile was used in the model (Figure 4.7). The profile is composed of separate log-linear segments for the lower 10% of the flow and the upper 90% of the flow. The two logarithmic profiles are joined smoothly with a linear fit:

$$\frac{u}{U} = \begin{cases} 0.077 \ln\left(\frac{z}{h}\right) + 0.997 & \left\{ \frac{z}{h} > 0.17 \right. \\ 0.185 \ln\left(\frac{z}{h}\right) + 1.240; & \left. 0.06 \leq \frac{z}{h} \leq 0.17. \right. \\ 1.165 \left(\frac{z}{h}\right) + 0.707 & \left. \frac{z}{h} < 0.06 \right. \end{cases} \quad (4.6)$$

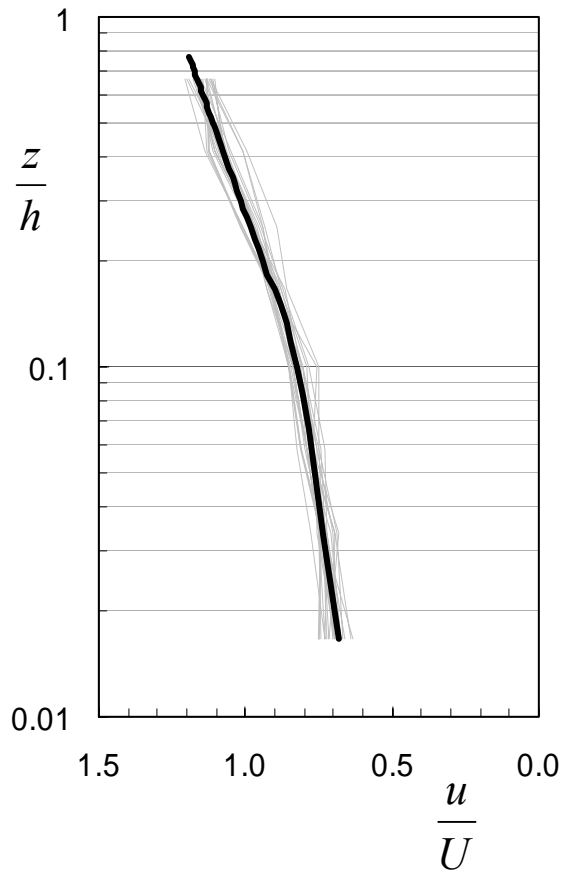


Figure 4.7. Plot showing velocity normalized by the mean velocity as a function of the normalized elevation above the bed. The light gray lines show the individual measurements for all transverse and downstream positions at both low and high flow rates. The heavy line is the average among all measurement positions for both flow rates.

The entrainment relation of Garcia and Parker (1991) is used to calculate the sand-bed entrainment rate. This relation was developed from laboratory and field data consisting of near-bed suspended sediment concentrations and estimates of grain stress derived by the Einstein stress decomposition (Einstein and Barbarossa, 1952) as

presented by Engelund and Hansen (1967). The skin friction model is based on an analogy between the flow of interest and a hypothetical flow that has the same slope and depth-averaged velocity but lacks the drag exerted by bedforms. The same analogy is considered here with the difference that the drag is exerted by the coarse immobile grains rather than bedforms. The depth-averaged velocity is related to the bed stress through a standard resistance relation

$$\frac{U}{u_*} = \frac{1}{k} \ln \left(\frac{11h}{k_s} \right), \quad (4.7)$$

where U is the depth-averaged velocity, h is the flow depth, k is the von Karmen constant, and k_s is the Nikuradse equivalent grain roughness associated with the total bed stress. By the analogy of the Einstein decomposition, a similar relation holds for the hypothetical flow:

$$\frac{U}{u'_*} = \frac{1}{k} \ln \left(\frac{11h'}{k'_s} \right), \quad (4.8)$$

where h' is the flow depth due to grain stress and k'_s is the grain stress roughness height. Here $k'_s = 3D_{50}$ is used. The slope S of the hypothetical flow is also the same as that of the flow in question, thus,

$$u_* = \sqrt{ghS}, \text{ and} \quad (4.9)$$

$$u'_* = \sqrt{gh'S}. \quad (4.10)$$

Combining equations (4.9) and (4.10),

$$\frac{u'_*}{u_*} = \sqrt{\frac{h'}{h}}. \quad (4.11)$$

Given the total stress and depth-averaged velocity, equations (4.8) and (4.11) can be solved iteratively for the grain stress. The grain stress cannot be assumed to apply at any particular point on the bed, but is taken to provide a consistent scaling between the flow velocity, depth, and stress producing sand entrainment.

Entrainment from a sand bed

The entrainment method presented here modifies the Garcia and Parker (1991) entrainment function with a sand-elevation correction function that is applied to the special case of coarse beds that are partially covered with fine sediment. The Garcia and Parker (1991) entrainment relation is

$$\hat{E}_{s,j} = \frac{A(\lambda Z_{m,j})^5}{1 + \frac{A}{0.3}(\lambda Z_{m,j})^5}, \quad (4.12)$$

where $A = 1.3 \times 10^{-7}$ is a constant, λ is a straining parameter related to the standard deviation of the grain size distribution and $Z_{m,j}$ is a similarity variable given by,

$$Z_{m,j} = \frac{u'_*}{w_{s,j}} R_{p,j}^{0.6} \left(\frac{D_j}{d_{50}} \right)^m, \quad (4.13)$$

where m is an exponent that represents the degree to which the mobility of grains of a given size is affected by its relationship to the median of the size distribution. Garcia and Parker (1991) use $m = 0.2$, which suppresses the effect on $Z_{m,j}$ of the ratio D_j/D_{50} . The grain Reynolds number is given by

$$R_{p,j} = \frac{\sqrt{(s-1)gD_j D_j}}{w_{s,j}}, \quad (4.14)$$

where s is the specific gravity of the sediment, g is the gravitational acceleration, and the particle settling velocity is calculated by the relation of Dietrich (1982).

Sand elevation correction function

The rate of entrainment calculated using equations (4.13) through (4.15) is modified as a function of the average sand bed elevation \hat{z}_s using a sand elevation correction function of the form proposed in Chapter 2:

$$\varepsilon = \left(1 + e^{-\xi(\hat{z}_s - Z^*)} \right)^{-\eta}. \quad (4.15)$$

The rate of entrainment is then calculated as

$$E_s = \varepsilon \hat{E}_s. \quad (4.16)$$

Model simulations were conducted with different values of the parameters ξ , Z^* , and η based on the results presented in Chapter 2 and Chapter 3, and fitted to the Main Channel observations (Figure 4.3).

Three sand elevation correction functions were tested in the numerical routing model, each with different values of the parameters ξ , Z^* , and η . One of these, SEC-1, is the sand elevation correction function that is based on the equilibrium transport experiments (Figure 4.3; Chapter 2). SEC-2 is the function presented in Chapter 3 that predicts the area of sand patches as a function of the average sand-bed elevation (Figure 4.8). It very closely matches the function for the area of exposed sand in a bed of hemispheres in closest packing arrangement with uniform sand distribution (Figure 4.3). Use of SEC-2 as a sand elevation correction indicates that net entrainment is derived exclusively from sand patches and that interstitial areas, which change more slowly in elevation, do not contribute to the net entrainment. Although this cannot be strictly valid (if the sand bed elevation in the interstitial areas is not changing in elevation, deposition by settling must be balanced by entrainment), it is possible that the entrainment rate from interstitial areas is significantly less than from the sand patches, such that it can be neglected. This implies low rates of deposition in the interstitial areas and, in turn, lateral variation in the near-bed suspended sand concentration, which was observed in the large channel experiments (Chapter 3). The third sand elevation correction function (SEC-3 in Figure 4.8) was developed after comparing modeled profiles of sand bed elevation with observed profiles, and is discussed below.

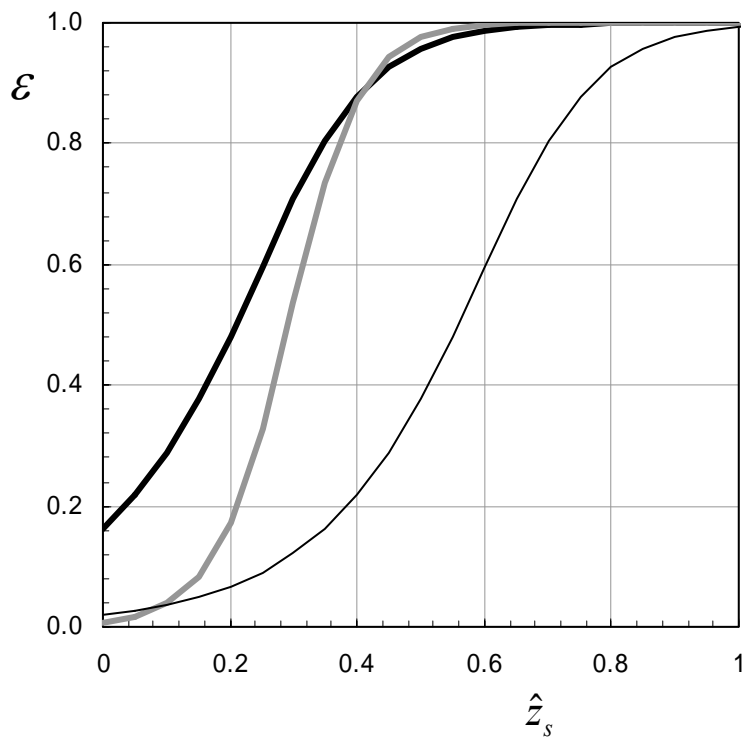


Figure 4.8. The sand elevation correction functions tested in the numerical transport and routing model. The function shown by the heavy black line is based on the data presented in Chapter 2 (SEC-1) ($\xi=12$, $Z^*=0.3$, and $\eta=0.5$). The function shown by the thin black line is based on the fraction of the bed covered by sand patches described in Chapter 3 (SEC-2) ($\xi=12$, $Z^*=0.65$, and $\eta=0.5$). The function shown by the heavy gray line is optimized using the model presented in this paper (SEC-3) ($\xi=18$, $Z^*=0.3$, and $\eta=0.9$).

Sand transport and bed sediment continuity

The representation of the vertical distribution of suspended sediment concentration is a critical aspect of accurately predicting the total suspended sediment flux. The governing equation for suspended sediment mass balance is the 2d form of the advection-diffusion equation,

$$\frac{\partial C}{\partial t} + u \frac{\partial C}{\partial x} - v_s \frac{\partial C}{\partial z} = \frac{\partial}{\partial z} \left(K_z \frac{\partial C}{\partial z} \right), \quad (4.17)$$

where C is suspended sediment concentration, x is the streamwise coordinate axis, z is the vertical coordinate axis, u is time-average streamwise velocity, and K_z is a coefficient of diffusion for suspended sediment. The vertical distribution of suspended sediment concentration may be obtained from equation (4.17) by representing the sediment diffusivity with an eddy diffusivity turbulence closure and integrating over the flow depth with appropriate boundary conditions. If conditions of uniform transport are assumed and a logarithmic velocity profile and linear stress distribution are used to define the eddy diffusivity, the Rouse profile for suspended sediment concentration is obtained:

$$\frac{C}{c_a} = \left[\frac{(h-z)/z}{(h-a)/a} \right]^{Ro}. \quad (4.18)$$

This solution applies the concentration boundary conditions, which are vanishing concentration at the free surface

$$C = 0 \Big|_{z=h}, \quad (4.19)$$

and specified concentration near the bed

$$C = c_a \Big|_{z=a}. \quad (4.20)$$

If the degree of disequilibrium is small, the concentration boundary condition may still be used, but the more general flux boundary condition is needed for nonuniform transport conditions (Parker, 1978):

$$K_z \frac{\partial C}{\partial z} = -w_s E_s. \quad (4.21)$$

The Rouse solution (Eq. 4.18) neglects downstream advection, which forces the requirement that the concentration profile is in equilibrium with the local boundary concentration. Stansby and Awang (1998) provide an analytical solution to the advection-diffusion equation that may be used to predict the adjustment for developing concentration profiles when clear flow abruptly encounters a sand-covered bed. Applied to our experiments, the adjustment time is about 24 s, corresponding to a distance of about 12 m. Because our experiments included a zone of about 5 m of nearly complete sand cover with decreasing cover downstream, this is probably an underestimate of the actual adjustment time. To permit prediction of changes in bed elevation for channel segments on the order of 1 to 2 m in length, we chose to implement a numerical solution to equation (4.18), thereby, retaining the term for downstream advection and employing the flux boundary condition (Eq. 4.21).

Exchange of sediment between the flow and the bed may be expressed by the equation for bed sediment mass continuity

$$(1 - \lambda_p) \frac{\partial z_s}{\partial t} = - \frac{\partial q_T}{\partial x}, \quad (4.22)$$

where λ_p is the porosity of sediment in the bed and q_T is the total streamwise sediment flux. In the laboratory experiments, flow strength and grain size were scaled such that the dominant mode of transport was by suspension. We also noted that sediment was redistributed from the accumulation zone at the upstream end of the test section by deflation, not bedform migration, further indicating suspension as the dominant mode of transport. For these reasons bedload transport was neglected and suspended load transport $q_s = q_T$ (Chapter 3).

Computational procedure

Equation (4.17) was solved numerically using an upwind finite-difference scheme based on the method presented by Patankar (1980). Matrix coefficients were solved for implicitly using an efficient tridiagonal algorithm. Sediment diffusivity K_z was approximated by the turbulent eddy viscosity K_E , which is related to the stress and the velocity gradient by

$$\tau = K_E \rho \left(\frac{\partial u}{\partial z} \right). \quad (4.23)$$

The bed stress is related to the total stress for a linear stress distribution according to

$$\tau = \tau_0 \left(\frac{h-z}{h} \right). \quad (4.24)$$

Equations (4.23) and (4.24) are combined to solve for K_E using the empirical bed stress (Eq. 4.5) and velocity profile (Eq. 4.6).

Zero concentration at the water surface was applied as the upper boundary condition. The flux near the bed was applied as the lower boundary condition. The flux at the bed is provided by the predicted entrainment rate (Eq. 4.12), with the spatially-averaged sand elevation correction (Eq. 4.15) applied when the average sand bed elevation is less than the bed roughness height. Changes in bed elevation are calculated from the divergence in the transport according to equation (4.22). The geometry and packing arrangement of the hemispheres are accounted for when sand bed elevation is calculated from changes in bed storage. The upstream boundary condition is the feed concentration during the feed segment of the run and zero concentration during subsequent segments. The initial conditions of the bed were no bed sediment for the simulations of Runs 1, 2, and 5. The initial conditions for simulations of Runs 3 and 4 included a 4.4 cm layer of evenly distributed sediment with a size distribution corresponding to that of the seeded bed.

Accurate prediction of fine sediment entrainment and transport in suspension requires a model that allows the bed grain size to evolve in concert with the transport (Rubin and Topping, 2001). Grain size evolution was included in the model by the use of multiple size fractions and conserving mass for each fraction. The grain size distribution was divided into seven classes based on the sedimentological ϕ scale, where $\phi = -\log_2 D$. The midpoint (on the logarithmic ϕ scale) of each size fraction is used as the representative size for that fraction. Each fraction is 0.5ϕ in size with midpoint values between 0.5ϕ (0.71 mm) and 3.5ϕ (0.088 mm). Each size fraction is treated independently in the model and grain size interactions are incorporated using the

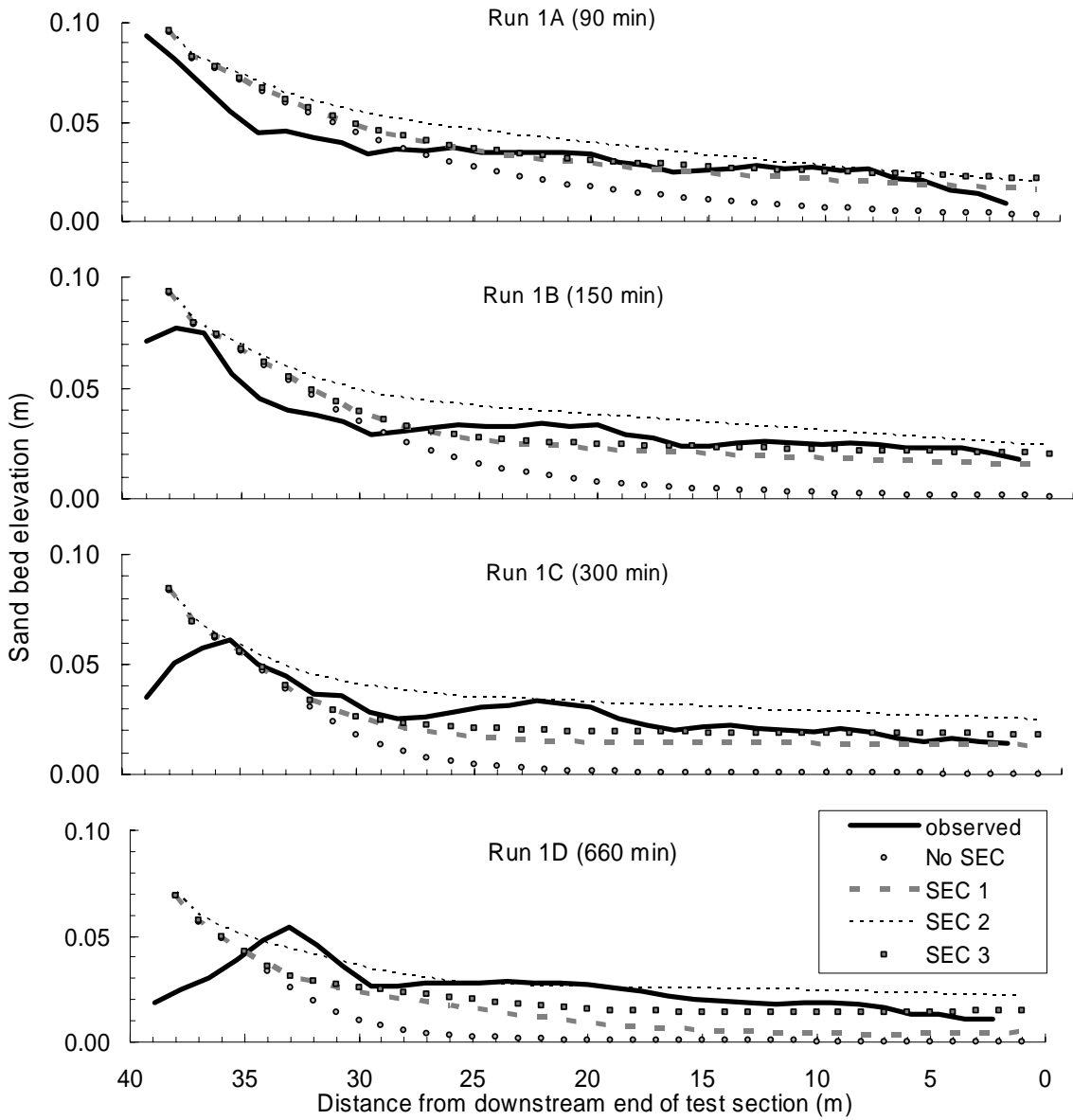
straining parameter λ and sorting parameter m of the original Garcia and Parker entrainment formulation.

Implementation of bed sediment continuity for mixed sizes requires consideration of the bed sediment mixing depth. Grains from within the mixing depth, or active layer, are eligible for entrainment in proportion to their presence in the grain size distribution. Particles in the substrate, beneath the active layer, are eligible for entrainment only after erosion has occurred and the bed elevation has changed. In Chapter 3, it was shown that the bed sediment was well-mixed to the depth of the bed roughness elements, which are of approximately the same scale as the bedforms. Because average bed elevations in these experiments rarely exceeded 4 cm and never exceeded 6 cm, the entire sediment bed was always within the active layer.

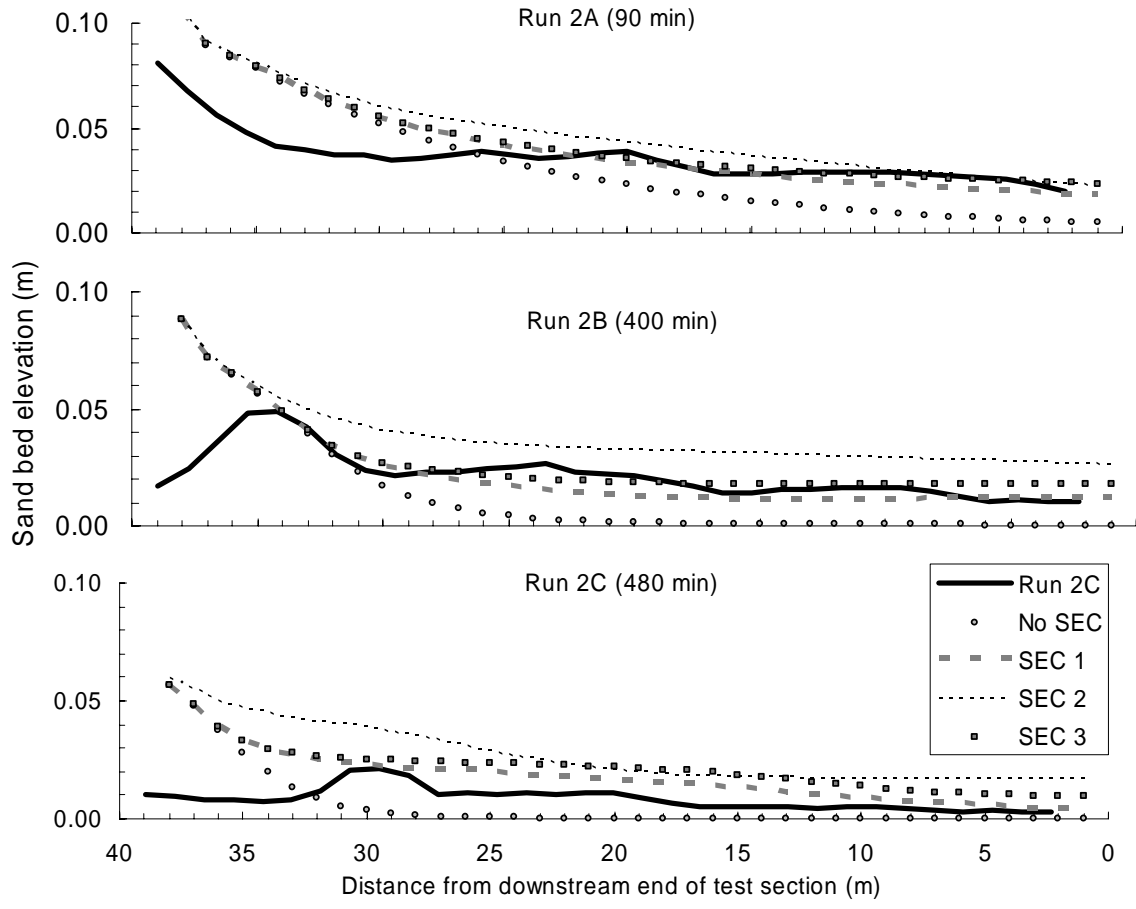
Comparison of numerical predictions and experimental observations

Numerical simulations were conducted for each of the five experimental runs using no sand elevation correction, SEC-1, and SEC-2 (Figure 4.9). For Run 1, the model predicted accumulation of about 10 cm of sand at the upstream end of the domain and decreasing sand elevation downstream (Figure 4.9a). Sand elevations in the central and downstream parts of the domain were highest using SEC-2 and lowest when no sand elevation correction was used. Elevations predicted using SEC-1 were slightly lower than those predicted using SEC-2. Following the feed segment of the simulation, the downstream thinning profile of predicted bed elevations was maintained as sand elevations decreased throughout the model domain. Using no sand elevation correction, sand evacuated most rapidly and was nearly exhausted from the downstream part of the domain after about 150 min of run time. Using a sand elevation correction, the model predicted that sand persisted throughout the channel for the entire run time (660 min). The model predicted a similar pattern for Run 2 (Figure 4.9b). Runs 3 and 4 included an initial sand thickness of 4.4 cm. This sand was coarser than the feed sediment (Figure 4.4) and less mobile. In Run 3, each simulation, regardless of sand elevation correction, predicted more than 5 cm (over the initial 4.4 cm bed thickness) of sand accumulation at

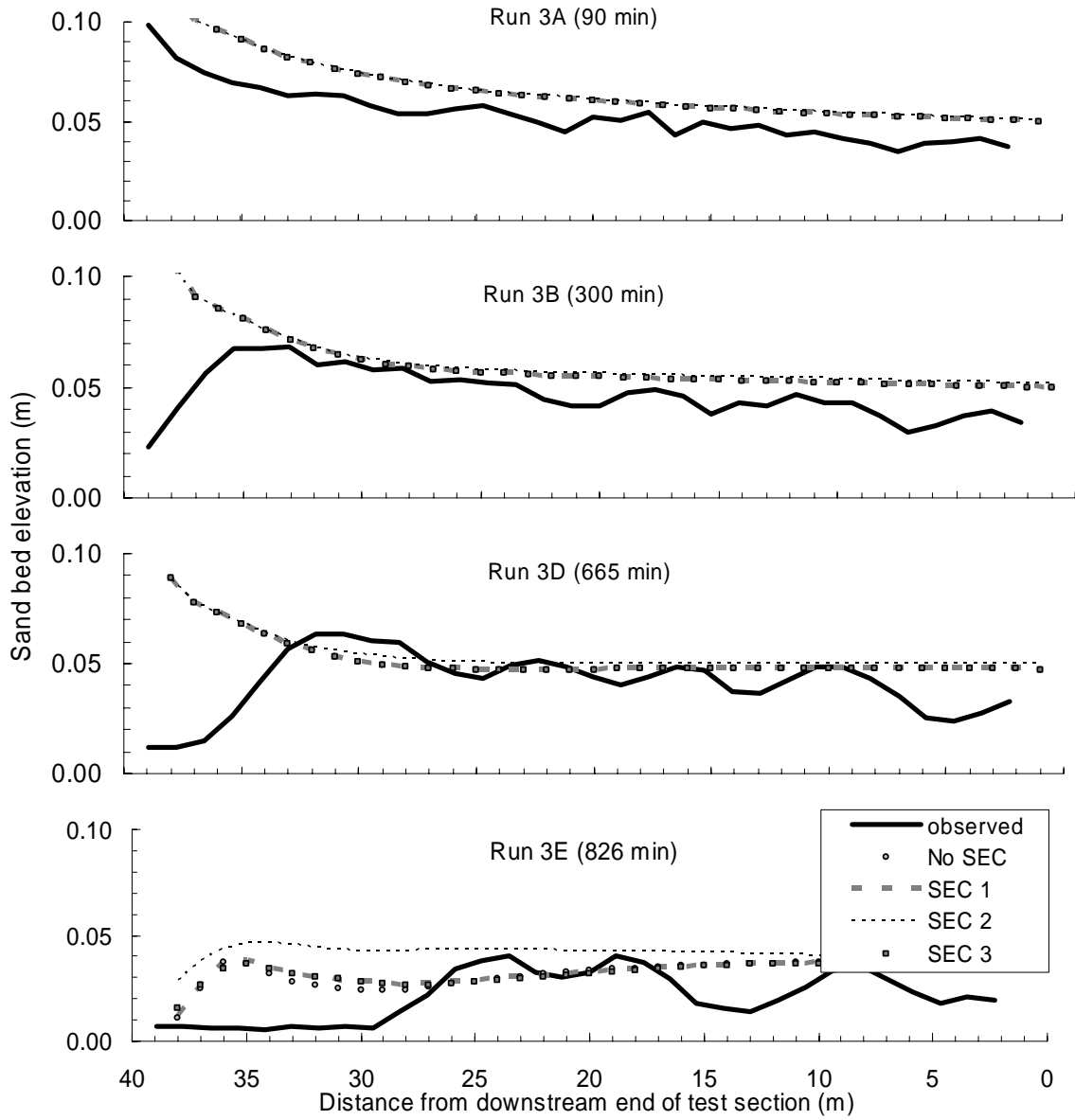
the upstream end (Figure 4.9c). The model predicted decreasing accumulation downstream.



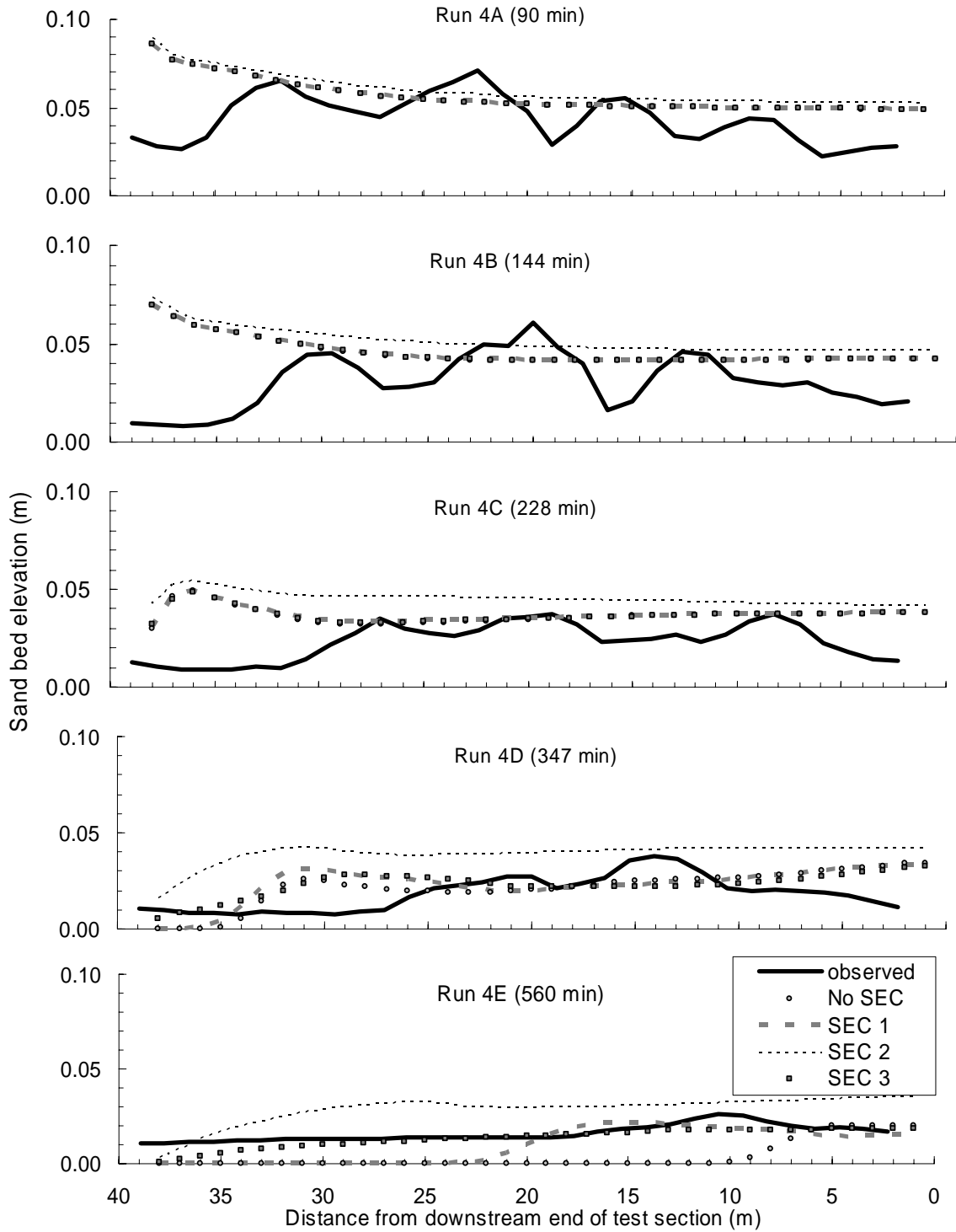
(a)



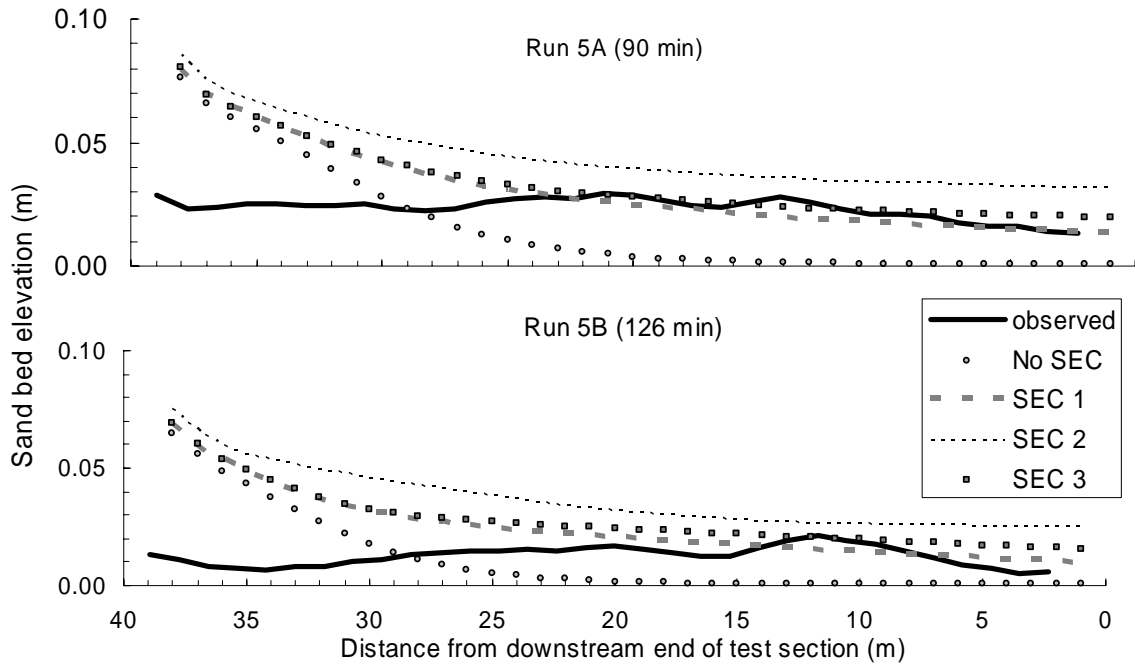
(b)



(c)



(d)



(e)

Figure 4.9. Plots of observed and predicted sand bed elevations. SEC-1 is the sand elevation correction proposed in Chapter 2. SEC-2 is the sand elevation correction based on distribution of sand patches described in Chapter 3. SEC 3 is the sand elevation correction that is adjusted to best fit the Main Channel observations.

The accumulated sediment was evacuated slowly from throughout the domain in each simulation until the final segment, in which the flow rate was increased. With the increased flow rate, the model predicted rapid evacuation of sand from the upstream end of the domain in each of the simulations, although the rate of evacuation was slightly less in the simulation using SEC-2. This evacuation of sediment from the upstream end resulted in a reversal of the predicted bed profile, with sand elevations increasing from the upstream to the downstream end of the domain. The simulation for Run 4 was similar to Run 3, but because the entire run was conducted at the higher flow rate, evacuation proceeded more rapidly (Figure 4.9d). Similar results were predicted for each SEC in the Run 4 simulations; until the final segments of the run when greater sand retention was predicted using SEC-2 and more rapid evacuation was predicted in the simulation that did not use a sand elevation correction. The same profile reversal that occurred in the simulations of Run 3 occurred in the simulations of Run 4. The simulations of Run 5,

also for the high flow rate, were similar to those predicted for Runs 1 and 2, but the model predicted less sediment accumulation and more rapid sediment evacuation (Figure 4.9e).

The bed elevations predicted by the numerical simulations were sensitive to the inclusion of the sand elevation correction function and less sensitive to different forms of the sand elevation correction function. For most of the simulations, bed elevations predicted using SEC-1 matched observed elevations quite well, but with somewhat higher rates of sand evacuation. With SEC-2, the model typically predicted rates of sand evacuation slower than observed. Without the sand elevation correction function, the model predicted that sand rapidly evacuated once the average bed elevation was below approximately $0.5r_b$. In Run 3, where the observed average bed elevation did not drop below $0.5r_b$, the simulated results with and without the sand elevation correction functions were similar. The difference between observed and predicted elevations tended to occur at the lower range of observed bed elevations in the case of predictions using SEC-1, while the differences when using SEC-2 tended to occur across a broader range of observed bed elevations. A third sand elevation correction function (SEC-3) was tested (Figure 4.8). This function is similar to SEC-1 at the upper range of bed elevations and transitions to meet SEC-2 at the lowest range of bed elevations. Thus, it predicts sand elevations similar to those predicted by SEC-1 for \hat{z}_s greater than about 0.3. At lower average sand elevations, this function results in decreased entrainment rates and higher sand elevations.

Observed and modeled mean bed elevations at the conclusion of each run segment are plotted in Figure 4.10. As described above, model predictions using SEC-2 over predict bed elevations and model predictions using SEC-1 tend to under predict bed elevations at the low range of the observations. SEC-2 was developed based on the hypothesis that all of the net entrainment into suspension occurs from the sand patches and that the sand in the interstitial spaces does not contribute to the entrainment. The function for the total area of sand as a function of the average sand elevation (Figure 4.3) was also tested in the numerical model and produced results very similar to those

produced using SEC-2. The behavior predicted using SEC-2 is consistent with the results presented in Chapter 2, indicating that observed entrainment rates are somewhat greater than would be expected if the entrainment was derived entirely from the sand patches. Thus, for some parts of the bed, sand entrainment rates must exceed the sand bed entrainment rate \hat{E}_s .

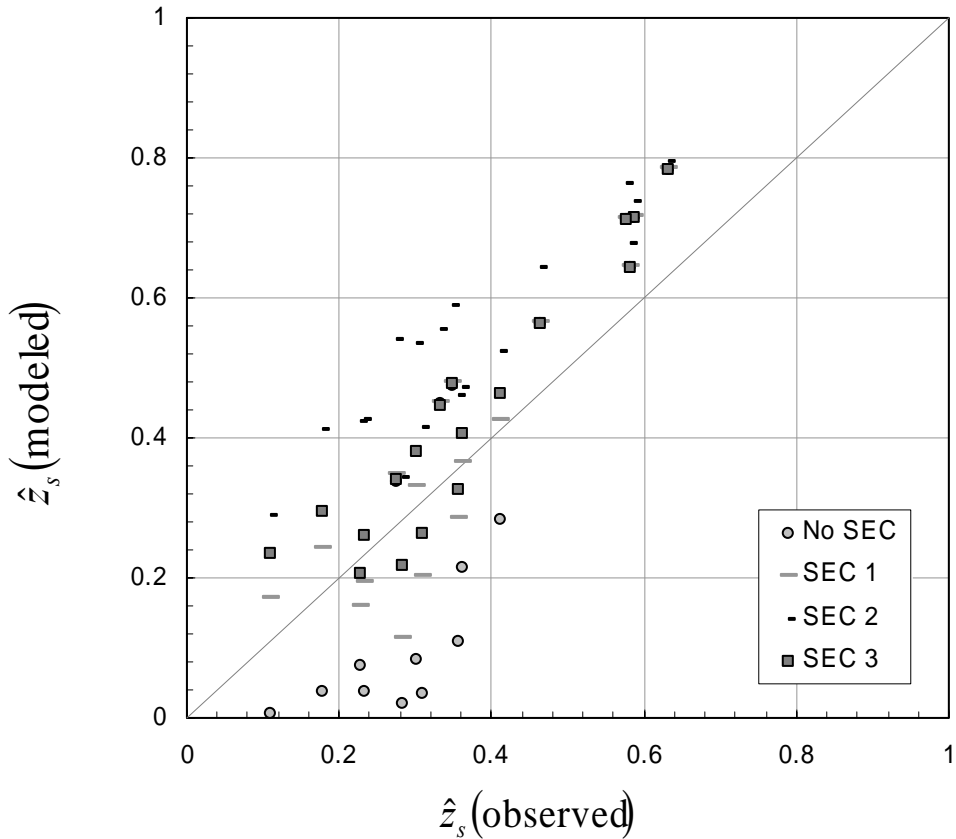


Figure 4.10. Average sand bed elevation at the end of each run segment predicted by the numerical model using the indicated sand elevation correction function according to the same notation used in Figure 4.8 and the average sand bed elevation observed in the Main Channel experiments.

The better performance of SEC-3 in the numerical model compared with SEC-1 may be the result of the greater area covered by sand patches in the wide-channel experiments. If entrainment rates are higher for some range of sand bed elevations in the interstitial areas, greater patch area would result in lower net entrainment.

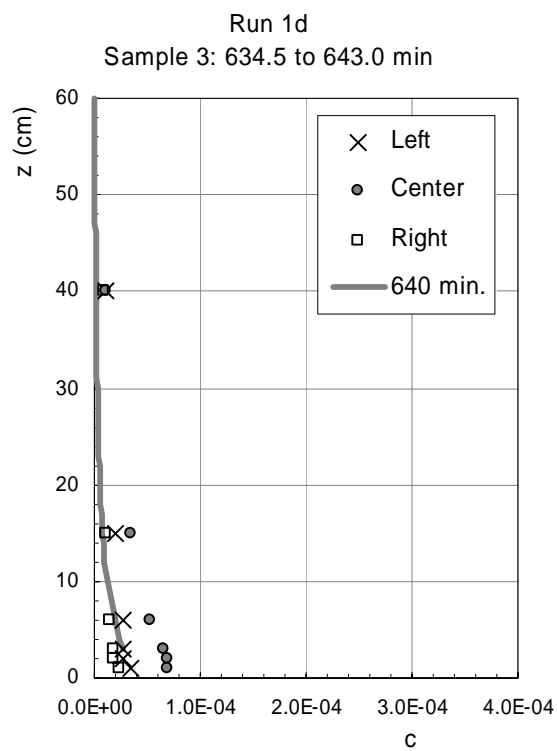
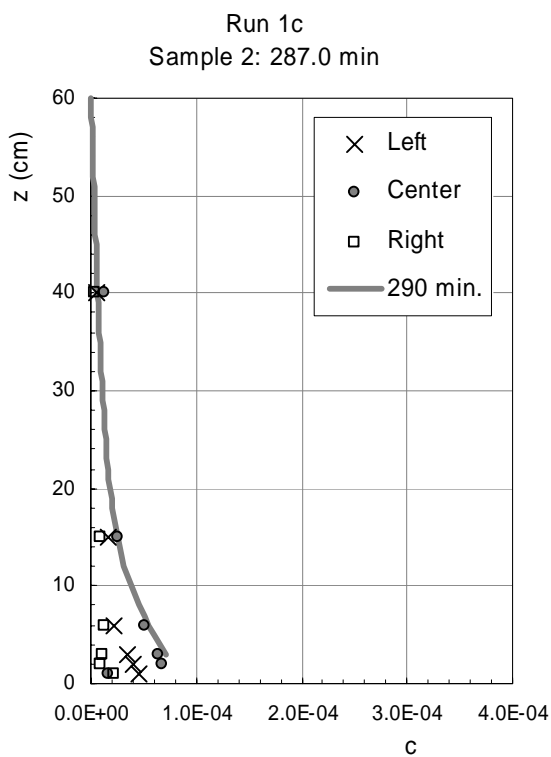
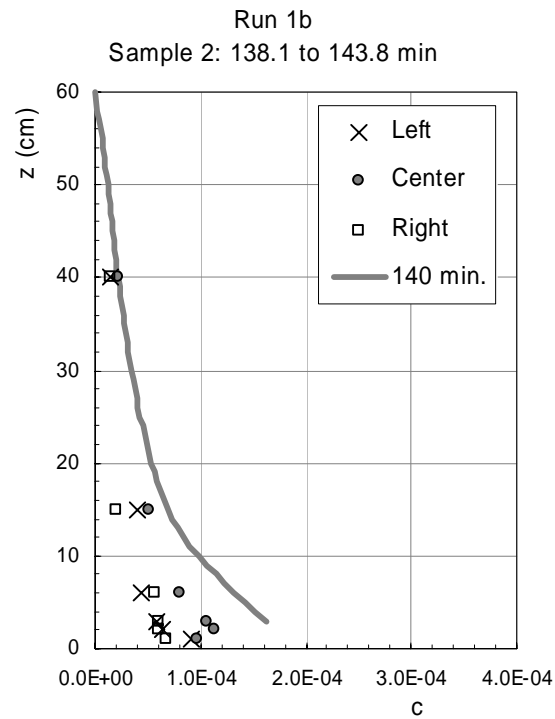
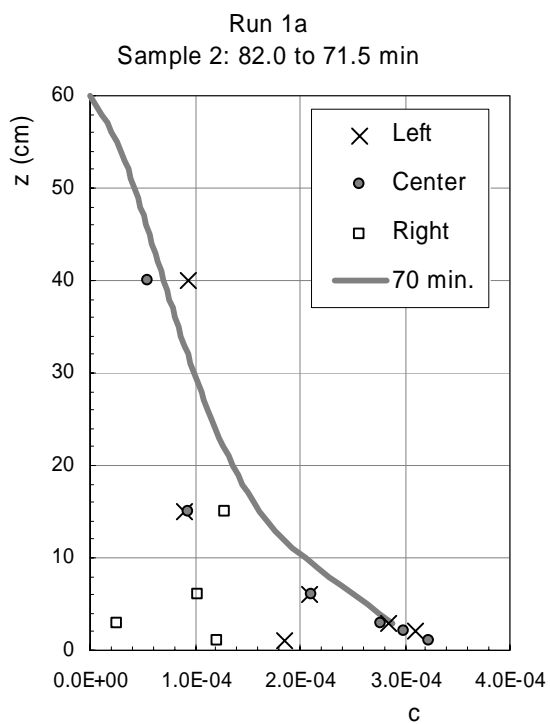
The greatest discrepancy between the observed and modeled bed elevations occurred in the upstream 5 m of the channel where predicted bed elevations tended to exceed the observed bed elevations (e.g. Figure 4.9a). This may be partially related to the existence of flow conditions in the beginning of the test section that were not included in the numerical model. The sediment feed apparatus was 2.5 m upstream from the test section and consisted of four evenly spaced vertical feed pipes with openings 16 cm above the bed. We placed turbulence generating structures in the channel to enhance the mixing of the feed sediment in the flow. The resulting flow conditions may have caused enhanced entrainment in this region that was not captured by the model. Matching observed bed elevations at the entrance of the test section is less important than matching the general pattern of bed elevations and matching bed elevations in the lower part of the test section.

Along most of the test section, simulated profiles of sand bed elevation replicated the shape of the observed profiles. In the early segments of each run, the modeled bed profiles indicate that sand thickness was greatest at the upstream end of the flume and decreased in the downstream direction, in agreement with the measured bed profiles. We observed that a downstream thinning profile was maintained as sediment was evacuated during the low flow evacuation segments. That behavior was replicated by the numerical model for the evacuation segments of Run 1 (1B-1D), Run 2 (2B), and Run 3 (3B-3D). In some run segments conducted at the high flow rate, the bed elevation profile reversed as sediment was evacuated most rapidly from the upstream end of the channel resulting in increasing sand depth in the downstream direction. That behavior was also captured by the numerical model.

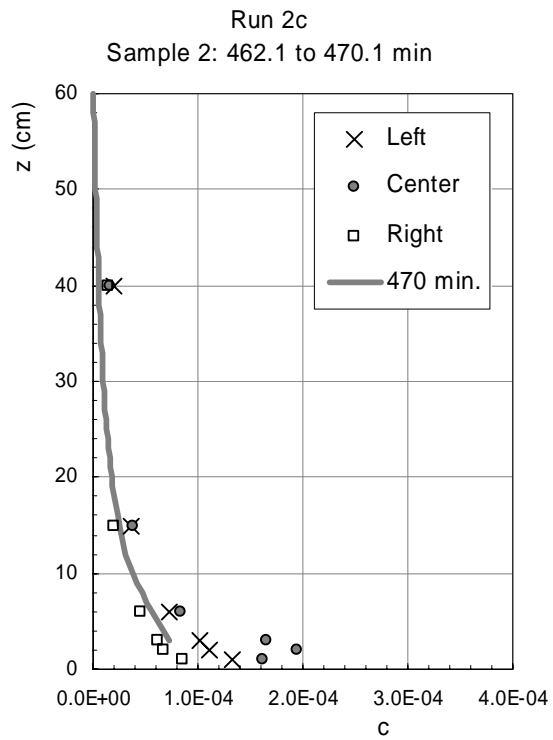
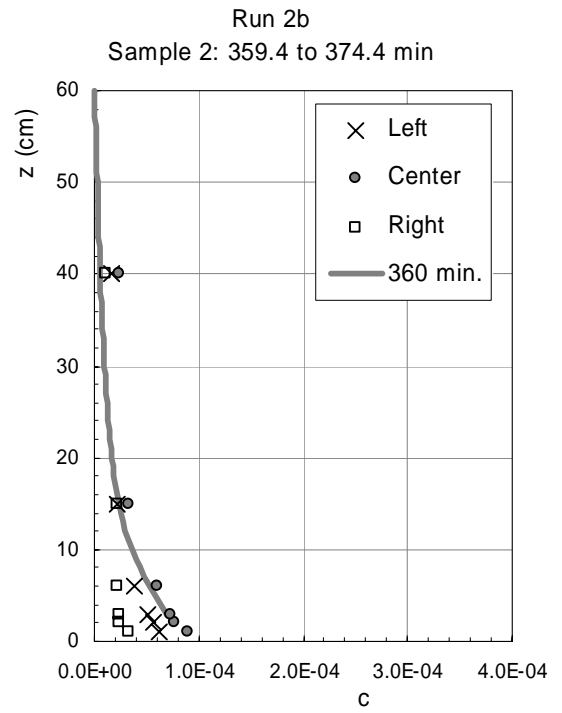
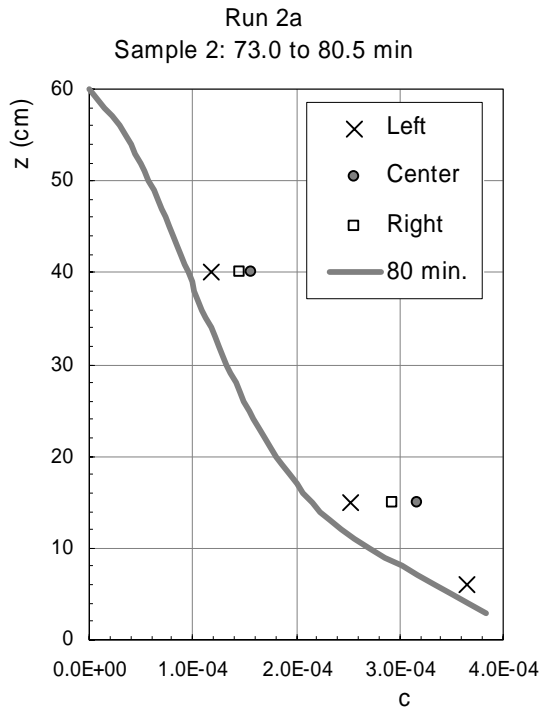
The performance of the coupled entrainment-transport model was also tested by comparing observed and simulated profiles of suspended sediment concentration. Suspended sediment samples were collected at one streamwise position and three cross-channel positions at irregular intervals during each run segment. The samples are compared with the modeled profile for the corresponding simulation time, rounded to the nearest 10 min. (Figure 4.11). In most cases, modeled concentrations are within the

range of variability of the measured concentrations. When the observed and modeled concentrations match near the bed, the rest of the profile tends to be in agreement, even though the shape of the profiles is variable. This indicates that the advection-diffusion component of the transport model is adequately predicting the concentration profiles, and that discrepancies between simulated and observed concentration are partially related to errors in the entrainment component. Where the predicted and observed profiles disagree, in some cases, the model over predicts concentrations (e.g. Run 1B); and in others, concentrations are significantly under predicted (e.g. Run 3A). The observations shown for Run 1B were collected as concentrations were decreasing following the feed segment of the run. In Run 3a, the sediment samples were collected as concentrations were increasing during the feed segment of the Run. Thus, the predicted concentrations lag behind the observations in both cases. In each case, the match between observed and predicted profiles improves in subsequent run segments.

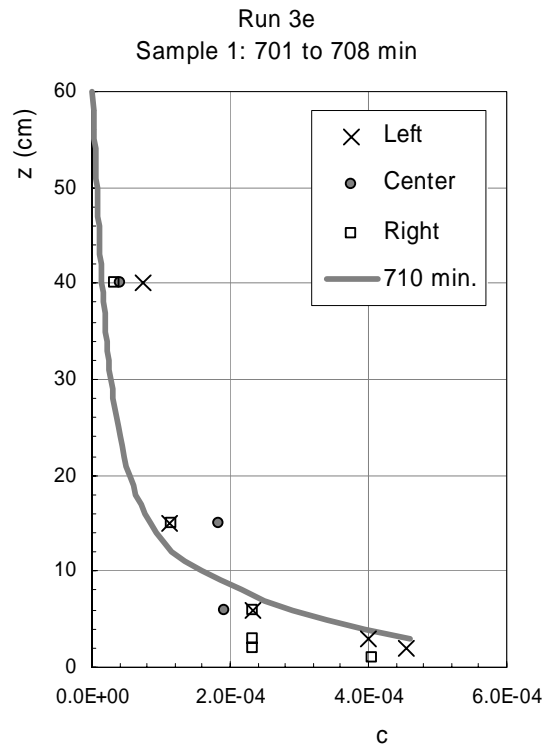
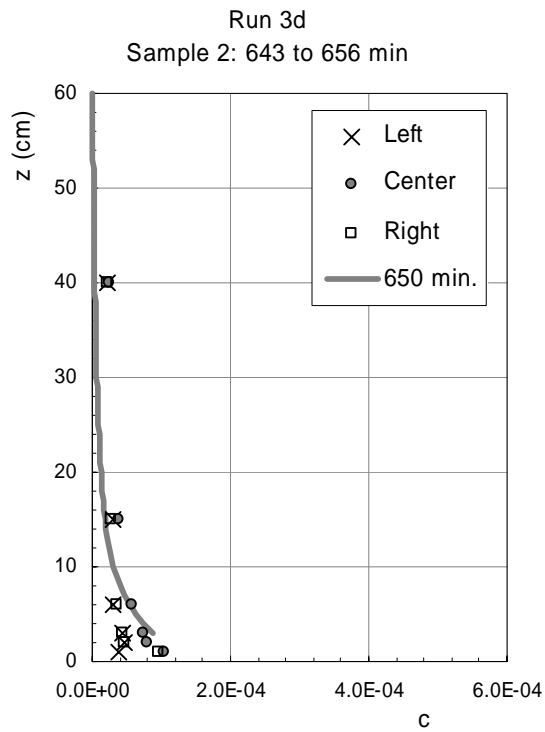
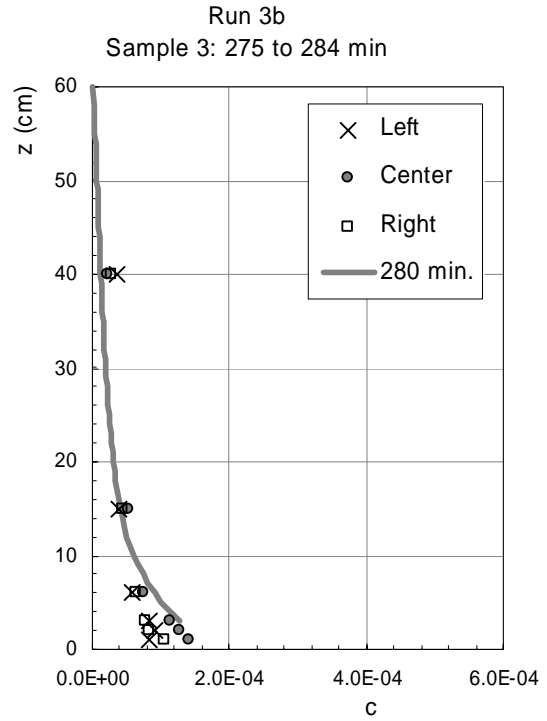
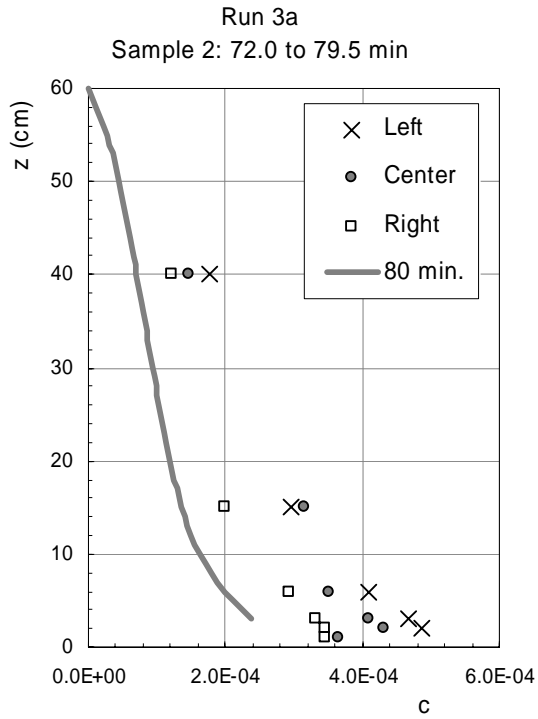
The numerical simulations also predicted the grain size of the bed surface. For most segments of Run 1 and Run 2, the observed and predicted median diameter of the bed material is similar and the observed gradual downstream trend of decreasing bed material size is replicated in the model results (Figure 4.12). A slight downstream coarsening observed in the bed following segment 2C (sampled at 479 min.) was not predicted by the model. This may be partly the result of coarse Mississippi River sand entering the channel during the high-flow segments. The quantity of the sand that entered the channel could not be measured and was not included in the numerical simulations. In the runs conducted with an initial bed of medium sand (Run 3 and Run 4), the bed coarsened downstream and the degree of coarsening decreased following the initial run segment. The bed coarsens downstream because the initial bed was coarser than the feed sediment, which preferentially accumulated at the upstream end of the test section during the feed segments. As the feed sediment was redistributed, the degree of coarsening decreased. The simulations capture this gradual coarsening in Run 3. The simulation results for Run 4 also show coarsening downstream, but the coarsening occurs in a single short step rather than gradually.



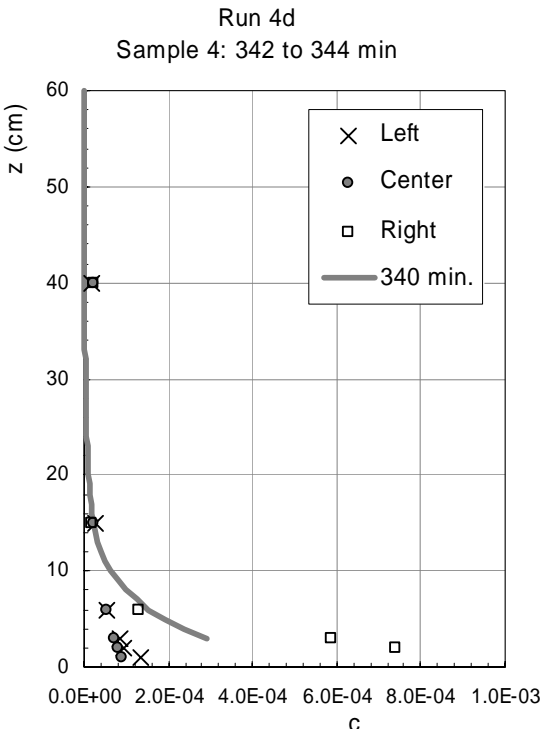
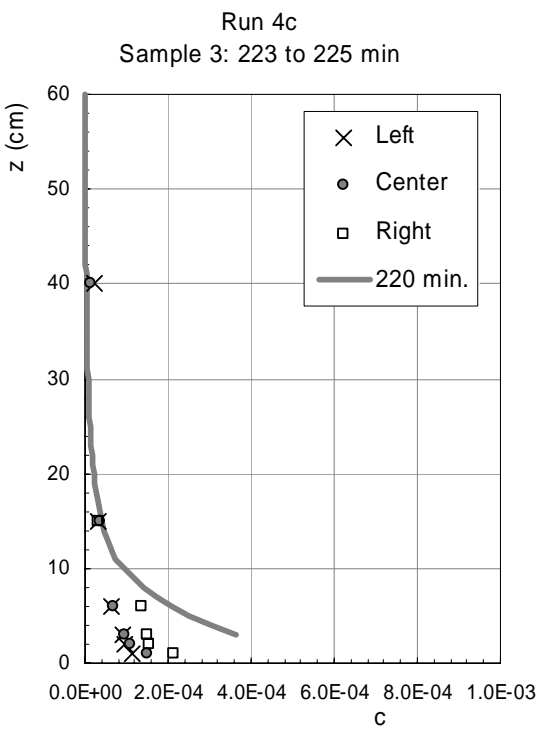
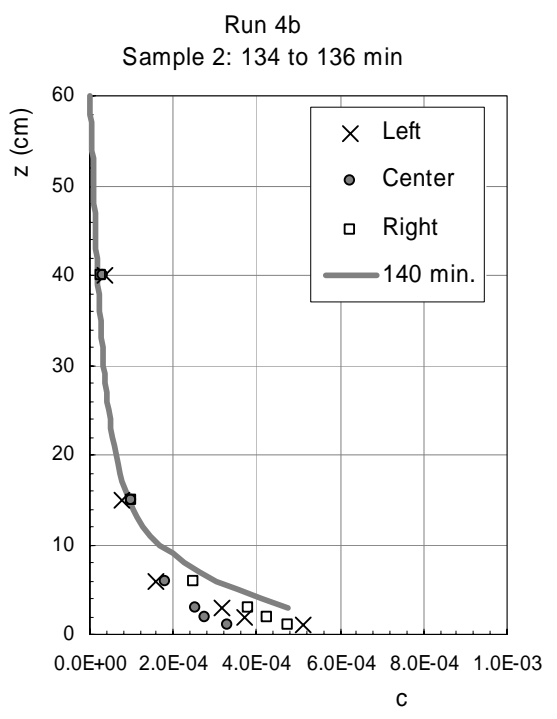
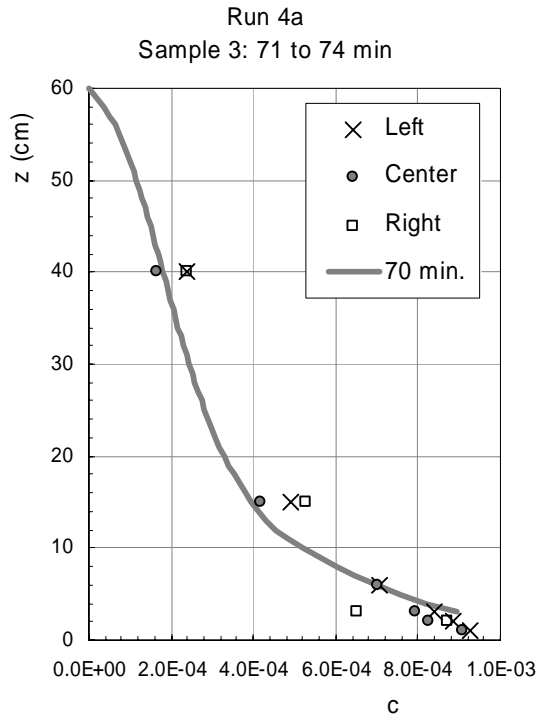
(a)



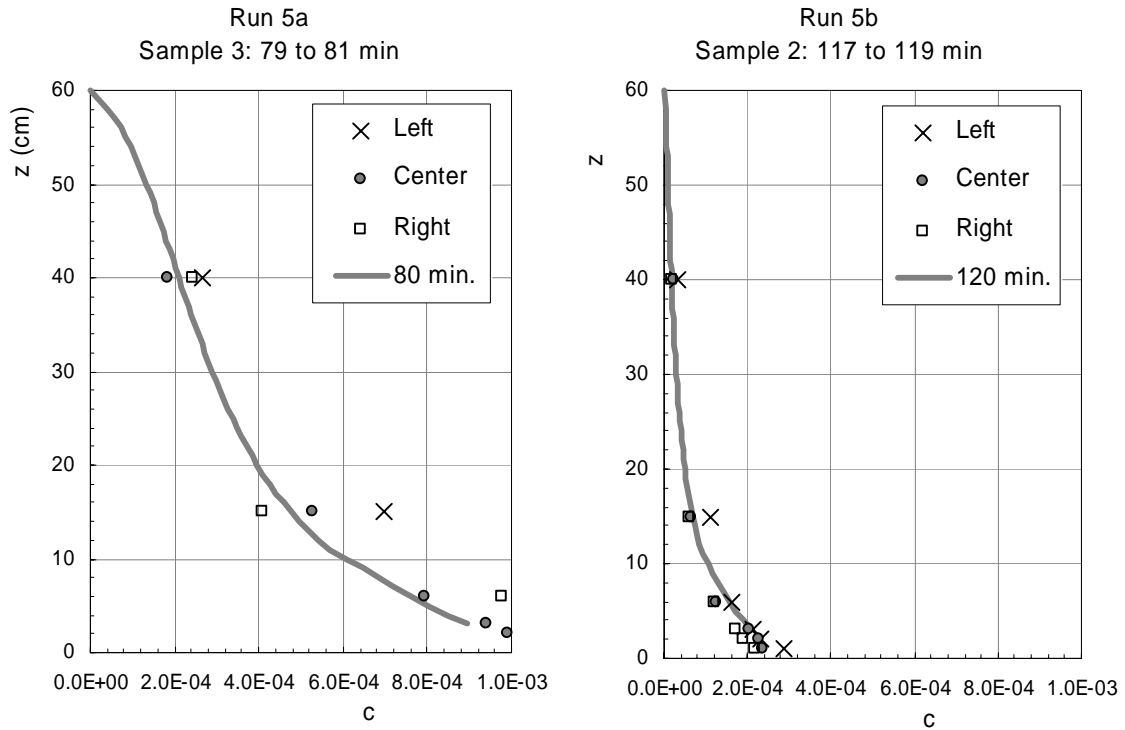
(b)



(c)

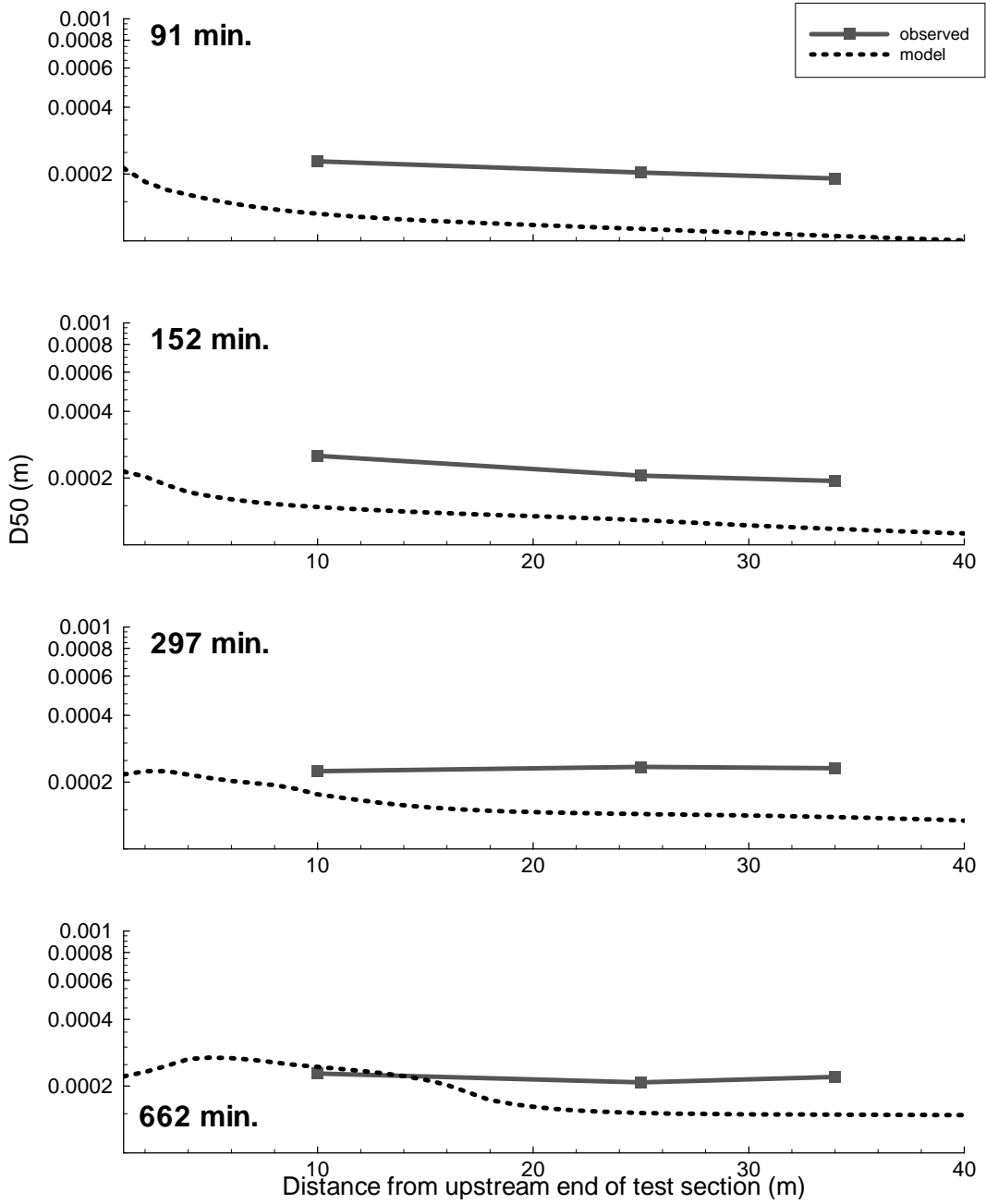


(d)

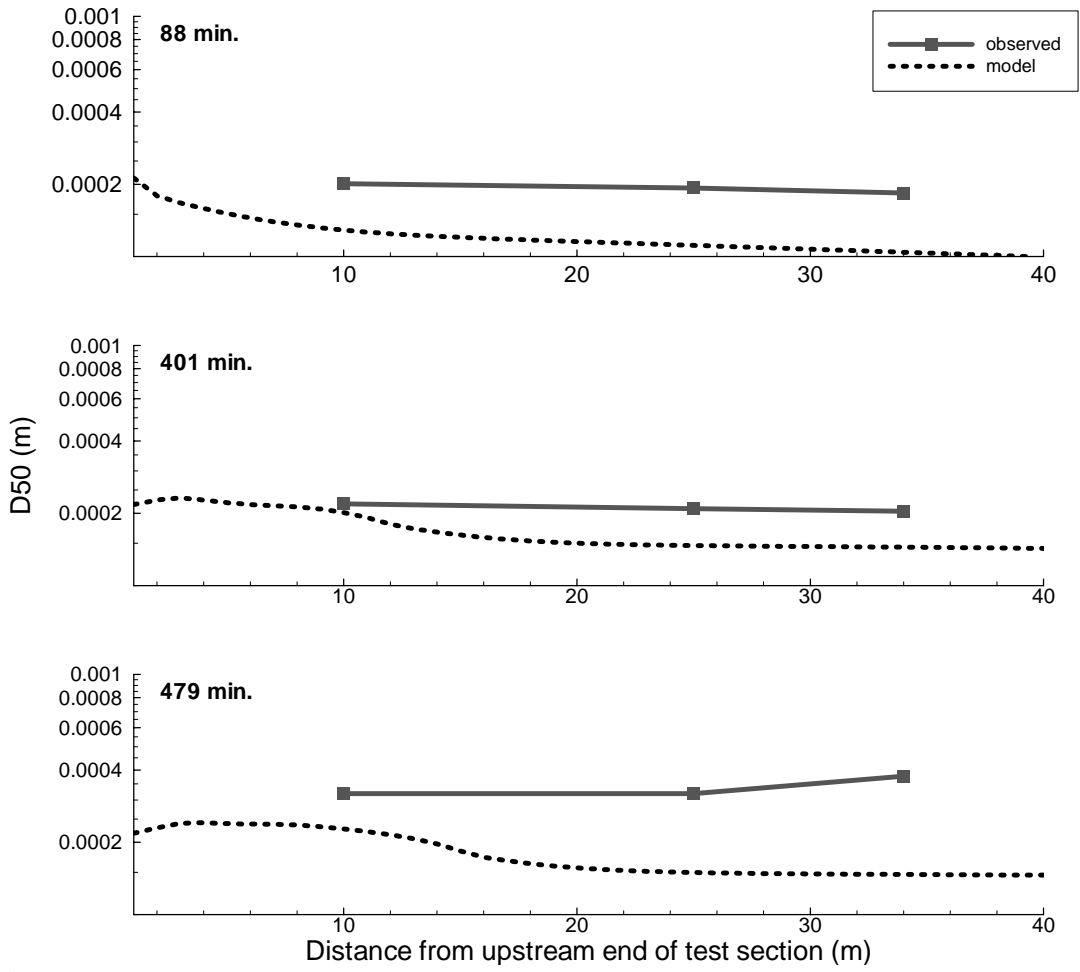


(e)

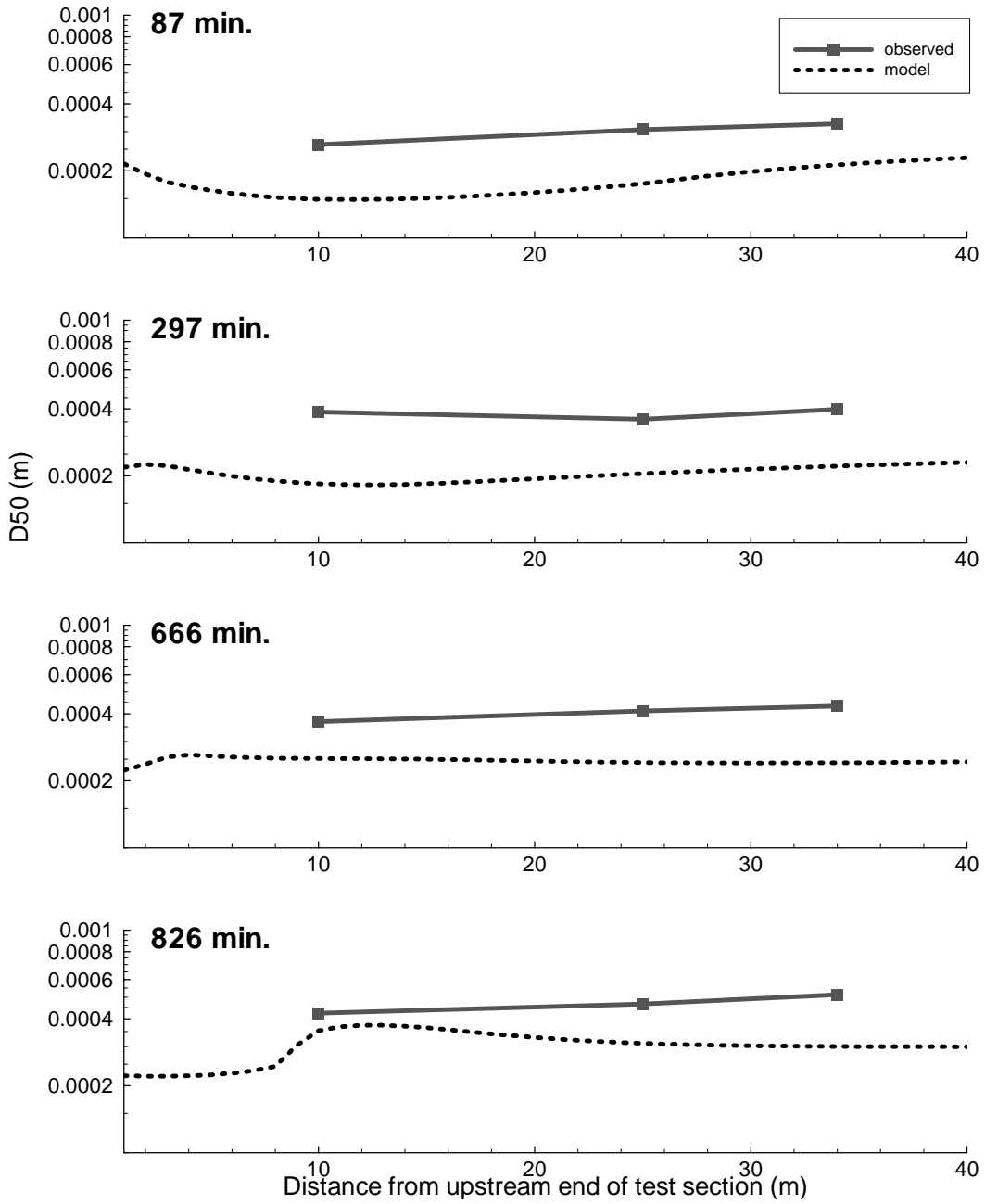
Figure 4.11. Profiles of modeled and observed concentration of suspended sediment. The observations include measurements from the left, center, and right sides of the channel. The time in the run during which the suspended sediment samples were collected is indicated above each plot. The modeled profile is shown by the heavy gray line and is a 10-min. average about the run time indicated in the legend in each plot. Concentrations are plotted in dimensionless units (volume of sediment per volume of liquid).



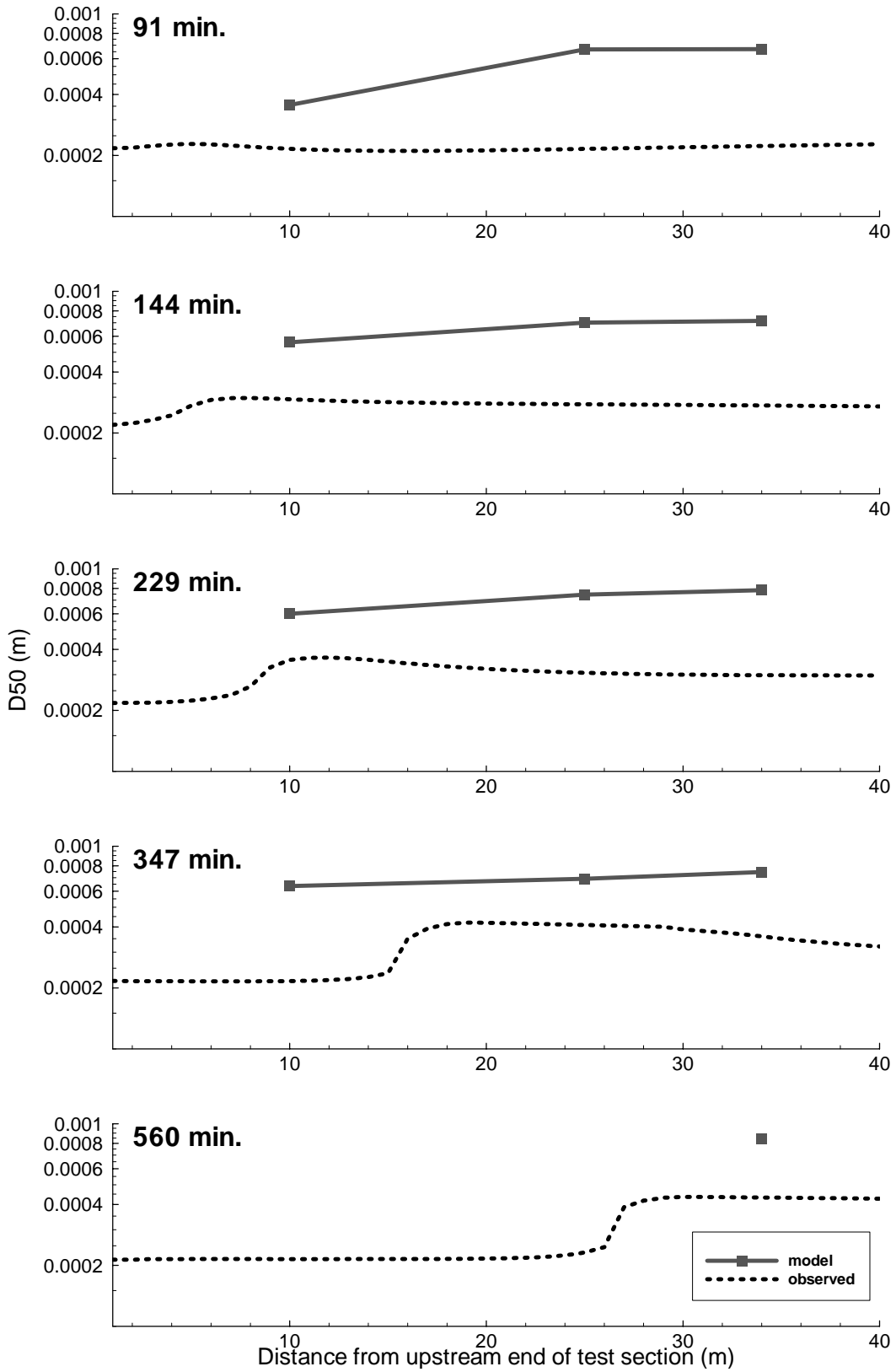
(a)



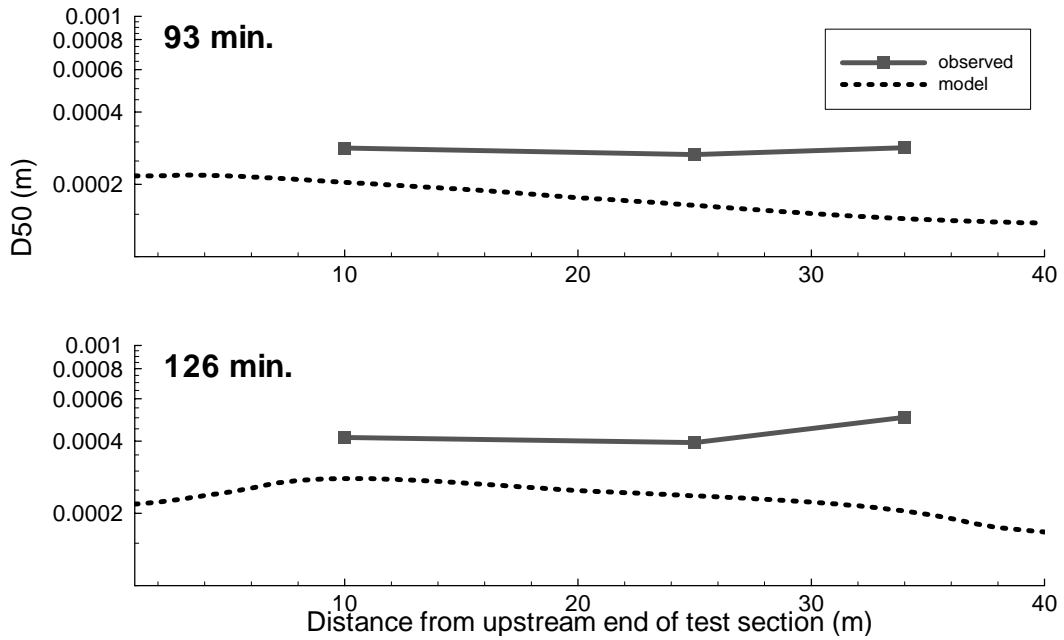
(b)



(c)



(d)



(e)

Figure 4.12. Plots of observed and modeled median grain size of the bed for Run1 (a), Run 2 (b), Run 3 (c), Run 4 (d), and Run 5 (e).

Coupling local and spatially-averaged sand entrainment

Thus far, our discussion has focused on spatially-averaged sand entrainment, which can be defined as the rate of sand entrainment averaged across local variations in bed sand cover. The sand elevation correction functions developed from the experimental data and tested in the numerical routing model are based on the spatially-averaged sand elevation. The process of sand entrainment from the bed, however, occurs locally. A value of spatially averaged \hat{z}_s consists of a mix of small values and values near one. While spatially-averaged entrainment is of practical importance, general understanding of entrainment from these bed conditions must include a consideration of local rates of sand entrainment.

The local entrainment rate E_{sL} can be integrated over the bed area A to find the spatially-averaged entrainment E_{sA} such that

$$E_{sA} = \frac{1}{A} \int_A E_{sL} dA. \quad (4.25)$$

The spatially-averaged sand elevation correction function was defined in equation (4.1).

The local sand elevation correction ε_L can be similarly defined as

$$\varepsilon_L = \frac{E_{sL}}{\hat{E}_s}, \quad (4.26)$$

where ε_L is a function of the local sand bed elevation,

$$\varepsilon_L = f(\hat{z}_{sL}), \quad (4.27)$$

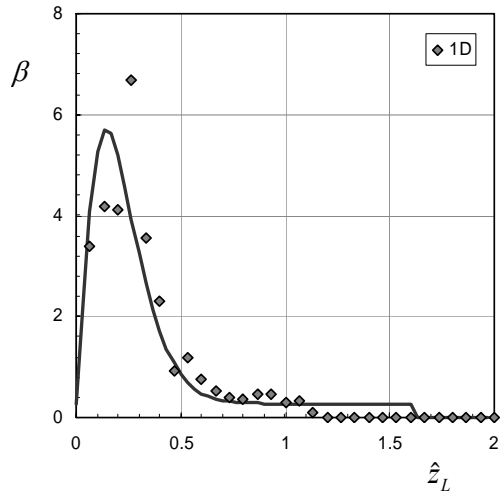
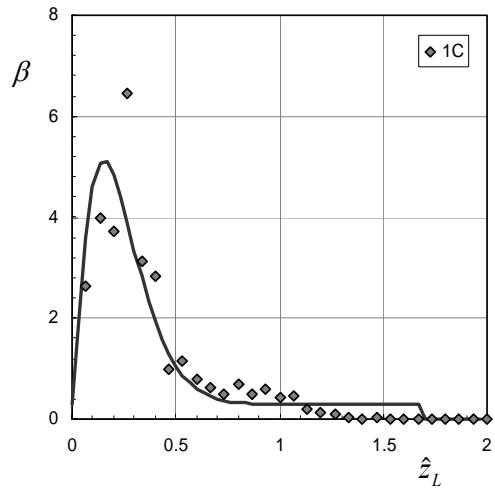
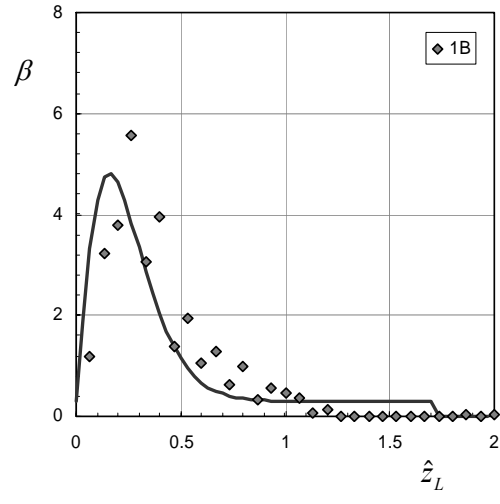
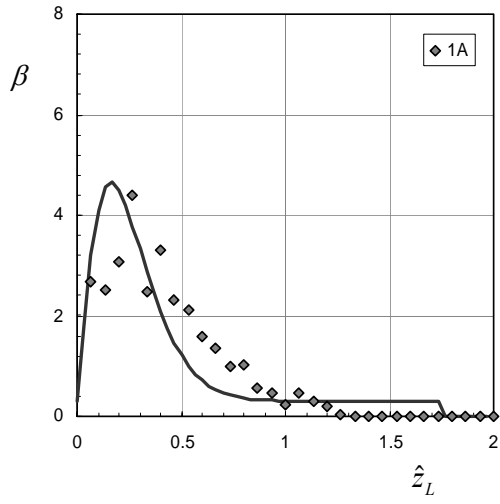
with the dimensionless local sand bed elevation given by

$$\hat{z}_{sL} = \frac{z_{sL}}{r_b}. \quad (4.28)$$

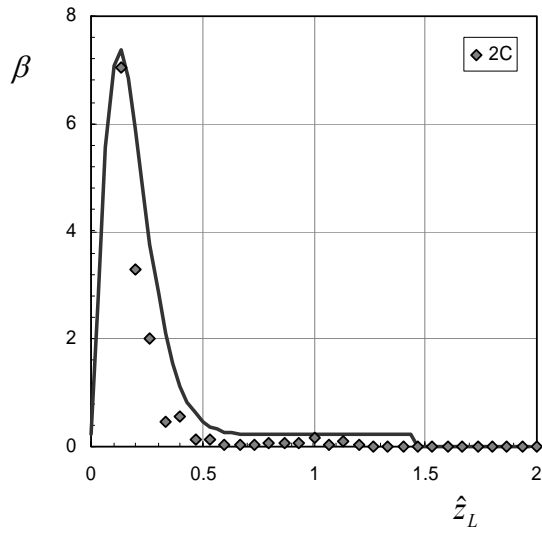
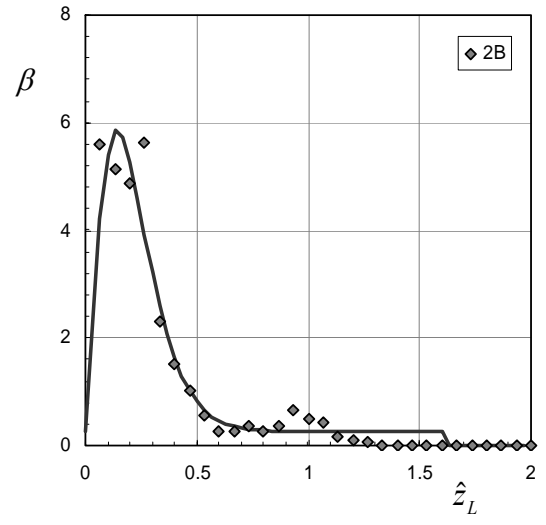
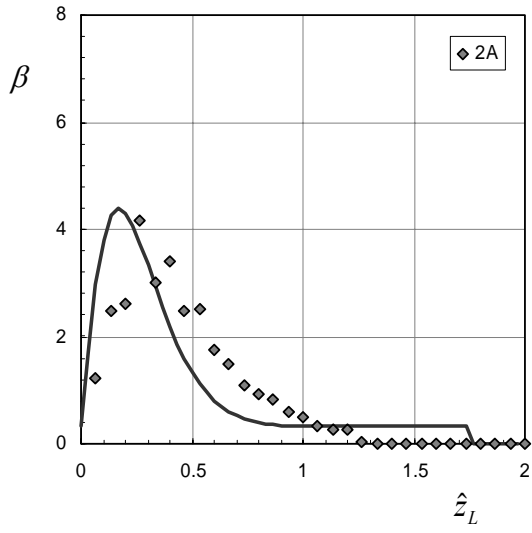
If a function for the local sand elevation correction and the distribution of local sand elevations are both specified, the spatially averaged sand entrainment rate and the form of the spatially averaged sand elevation correction function can be determined. We do not know the local entrainment function a priori, but we do have the empirically-determined spatially-averaged sand elevation correction function. Thus, the problem may be inverted and we can evaluate possible local entrainment functions. The experimental

observations are used to describe the distribution of sand bed elevations necessary to calculate local entrainment.

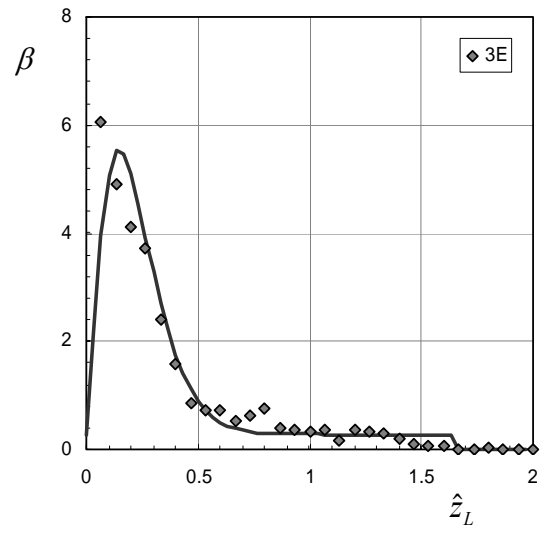
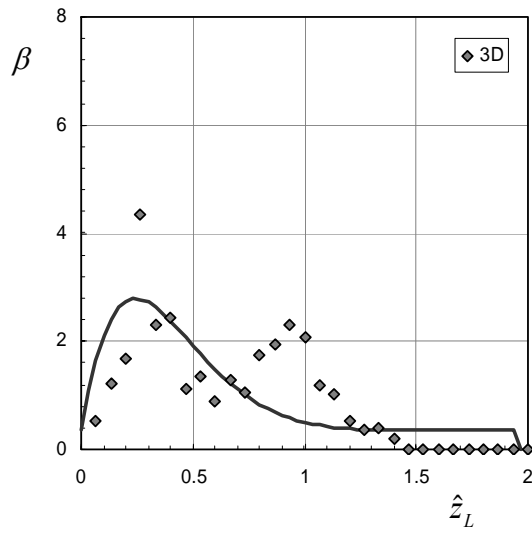
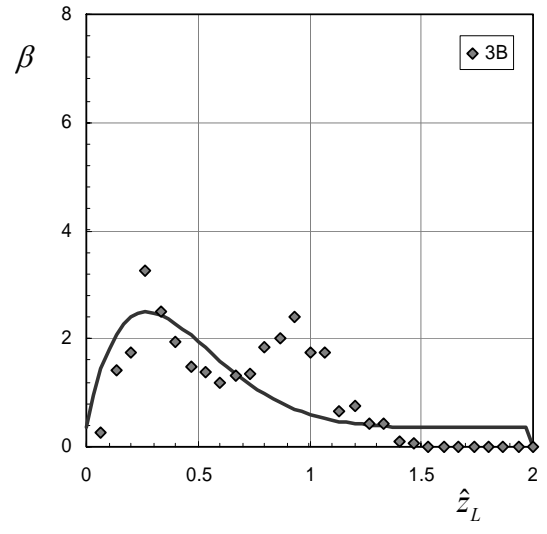
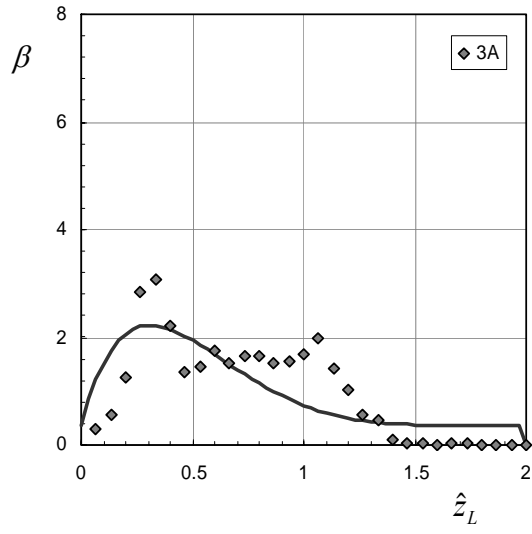
In order to evaluate different functions for ε_L , it is necessary to express the distribution of \hat{z}_{sL} in a compatible form. Figure 4.13 shows the measured distribution of sand bed elevations following each run segment, plotted as probability density functions. The corresponding mean bed elevation for each run segment is listed in Table 3.2. Because we are interested primarily in the entrainment from sand patches (barchans and sand stripes) and the interstitial storage spaces among the roughness elements, the measurements from the accumulation zone are excluded from these plots. The average bed elevation was always less than $0.6r_b$; in patches, the local elevation often exceeded the bed roughness height and occasionally approached $2r_b$.



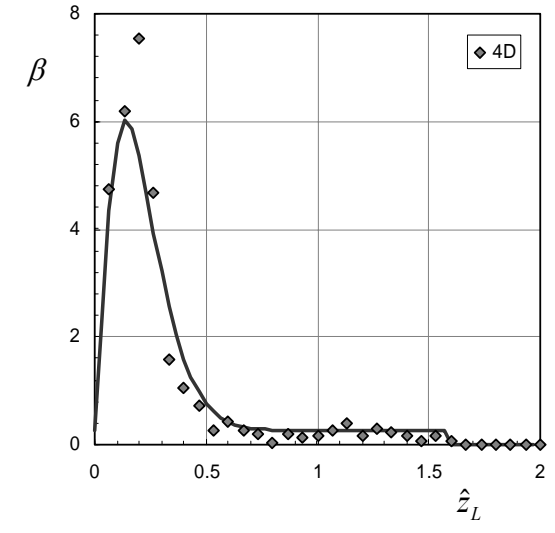
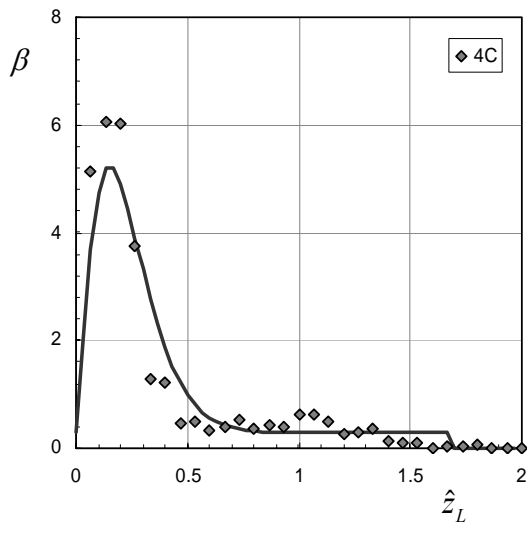
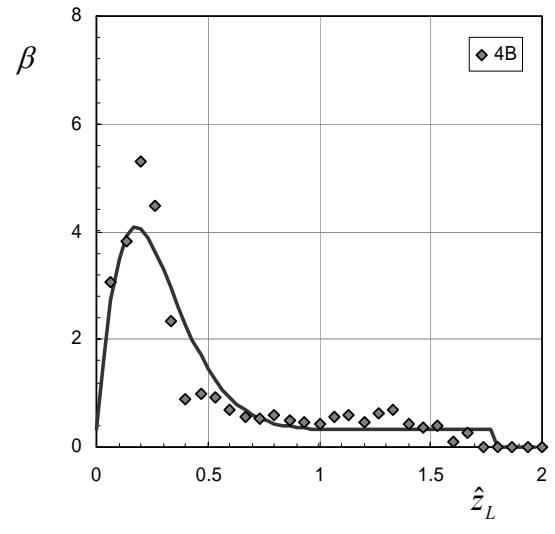
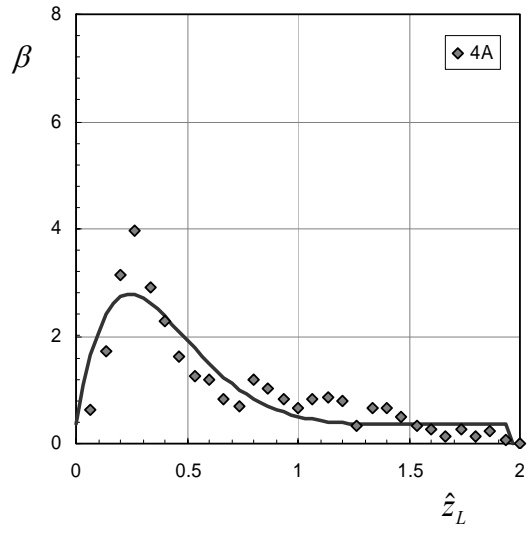
(a)



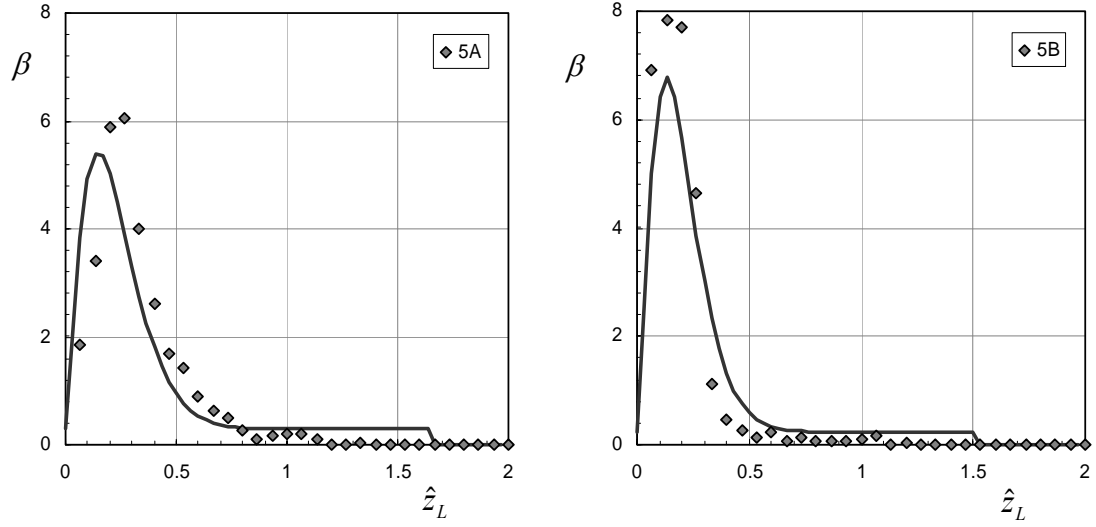
(b)



(c)



(d)



(e)

Figure 4.13. Plots of the bed elevation density functions for for Run1 (a), Run 2 (b), Run 3 (c), Run 4 (d), and Run 5 (e).

Despite the variety of average sand depths and bed configurations, the density functions are similar in shape. All are strongly asymmetrical and skewed to the left. Most have a broad shoulder on the right and drop abruptly to zero at some point. These density functions can be approximated with a modified beta distribution:

$$\beta(\chi) = \begin{cases} \frac{1}{f(a_\beta, b_\beta)} \chi^{a_\beta-1} (1-\chi)^{b_\beta-1} & (0 < \chi < 1), \end{cases} \quad (4.29)$$

where χ is the sand elevation normalized to the median diameter of the bed surface

$$\chi = 2\hat{z} \text{ and}$$

$$f(a_\beta, b_\beta) = \int_0^1 \chi^{a_\beta-1} (1-\chi)^{b_\beta-1} d\chi. \quad (4.30)$$

Two additional parameters are required to cause the function to asymptotically approach c_β rather than zero, and step to zero at a given value d_β .

$$\beta'(\chi) = \begin{cases} \frac{\frac{1}{f(a_\beta, b_\beta)} \chi^{a_\beta-1} (1-\chi)^{b_\beta-1} + c_\beta}{g(a_\beta, b_\beta, c_\beta, d_\beta)} & (0 < \chi < d_\beta), \\ 0 & (d_\beta \leq \chi < 1) \end{cases} \quad (4.31)$$

where

$$g(a_\beta, b_\beta, c_\beta, d_\beta) = \int_0^{d_\beta} \left(\frac{1}{f(a_\beta, b_\beta)} \chi^{a_\beta-1} (1-\chi)^{b_\beta-1} + c_\beta \right) d\chi. \quad (4.32)$$

The function $g(a_\beta, b_\beta, c_\beta, d_\beta)$ ensures that the beta distribution integrates to unity over the range $\chi = 0$ to $\chi = 1$.

Equations (4.29 – 4.32) were used to determine best fit values for the coefficients $a_\beta, b_\beta, c_\beta,$ and d_β for Run 4. Each of these coefficients was then evaluated as a function of the normalized mean bed elevation χ (Figure 4.14). The resulting linear relations for each coefficient were used to calculate the simulated distributions shown in Figure 4.12 compared with the observed distributions. The fit is best for Run 4, which was used to determine the coefficients, but is also satisfactory for the other runs.

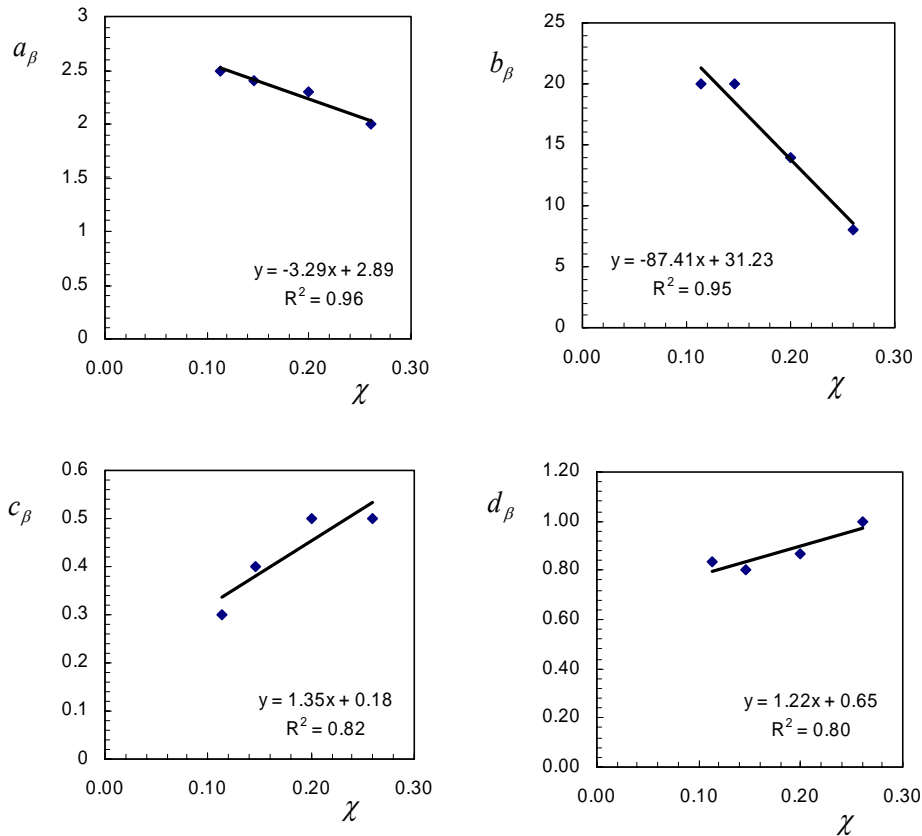


Figure 4.14. Plots using data from each segment of Run 4 that were used to determine relations for each of the parameters ($a_\beta, b_\beta, c_\beta,$ and d_β) in the modified beta distribution as a function of the sand bed elevation normalized by the bed sediment median diameter.

The beta coefficients are fitted for average bed elevations \hat{z}_s from 0 to 0.6. The experimental data do not include observations of mean bed elevation greater than this range. As the mean bed elevation approaches one, the frequency of low local elevations must decrease and the frequency of local elevations greater than one must increase. Entrainment from local elevations greater than or equal to one will be assumed to occur at the same rate as for a sand bed ($\varepsilon_L = 1$ for $\hat{z}_{sL} \geq 1$). Thus, we do not need to predict the distribution of local elevations greater than one. To predict the distribution of local elevations between $\hat{z}_s = 0.6$ and $\hat{z}_s = 1.0$, an additional constraint is introduced that forces the distributions to have near-zero occurrence of $\hat{z}_{sL} < 1$ for $\hat{z}_s = 1$. This is applied by linearly interpolating values for each of the coefficients between the values for \hat{z}_{sL} calculated at $\hat{z}_s = 0.6$ and the values that produce essentially no values of $\hat{z}_{sL} < 1$ for $\hat{z}_s = 1$. Those values are $a = 10$, $b = 0$, $c = 0$, and $d = 1$. Figure 4.15 shows simulated distributions of local sand bed elevation for several different spatially-averaged sand bed elevations. For beds with an average elevation less than about $0.5r_b$, the model predicts the distribution of local elevations to be skewed with the highest density of local elevations less than about $0.3r_b$. As the mean bed elevation increases from $0.5r_b$ to $1.0r_b$, the distribution shifts to the right.

Equations (4.29 – 4.32) with the coefficients given above provide a method for calculating the distribution of local sand elevations given the spatially-averaged sand bed elevation. The local sand elevation correction is determined at each bed elevation in the distribution by the local sand elevation correction function (Eq. 4.26). The spatially-averaged sand-elevation correction is then calculated by integrating the local correction over the bed elevation distribution (Eq. 4.25). For each average sand bed elevation with $\hat{z}_s < 1$, a portion of the bed is exposed roughness elements. These areas have no local entrainment and must be included in the integration to determine spatially-averaged sand elevation correction. The fraction of bed covered by sand was calculated for a bed of hemispheres arranged in closest packing. For this geometry the sand covered area A_s can be calculated by the following relation:

$$\frac{A_s}{A_b} = \frac{B - (\pi r_b^2 - z_s^2)n}{B}, \quad (4.33)$$

where A_b is the total area of the bed, B is the channel width, and n is the number of roughness elements per unit channel length. These steps are repeated to calculate the spatially-averaged sand elevation correction for mean bed elevations between zero and one to generate a function for the spatially-averaged sand elevation correction.

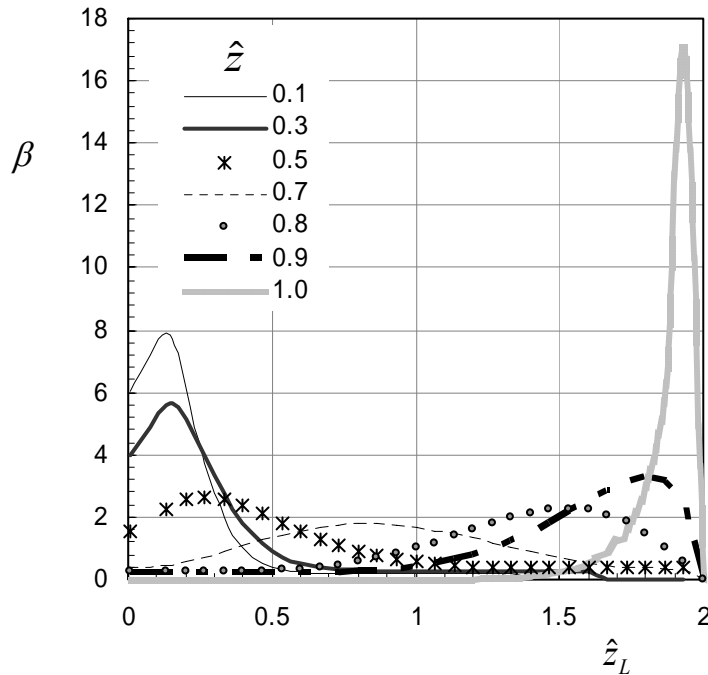


Figure 4.15. The modeled density functions of sand bed elevation shown for a range of average sand bed elevations between 0 and $2r_b$.

Because the experiments presented in Chapter 2 had limited bed form development and a more uniform distribution of sand bed elevations, the sand elevation correction function derived from those experiments is closer to a local sand elevation correction (LOSEC). That function (SEC-1) was used in the local entrainment model to predict a spatially averaged sand elevation correction (SASEC-1). SASEC-1 falls to the right of SEC-3 (Figure 4.16), the sand elevation correction that provided the best agreement between observed and predicted sand elevations using the sand routing model. Using no sand elevation correction ($\varepsilon_L = 1$ for all areas of the bed covered by sand and

$\varepsilon_L = 0$ elsewhere), the predicted spatially averaged sand elevation correction (SASEC-2) shifts only slightly to the left (Figure 4.16). The similarity arises because the decrease in the area of sand available for entrainment as the average sand elevation drops is a dominant factor in any sand elevation correction function. Thus, that formulation for local entrainment does not produce spatially averaged entrainment rates that match those observed experimentally.

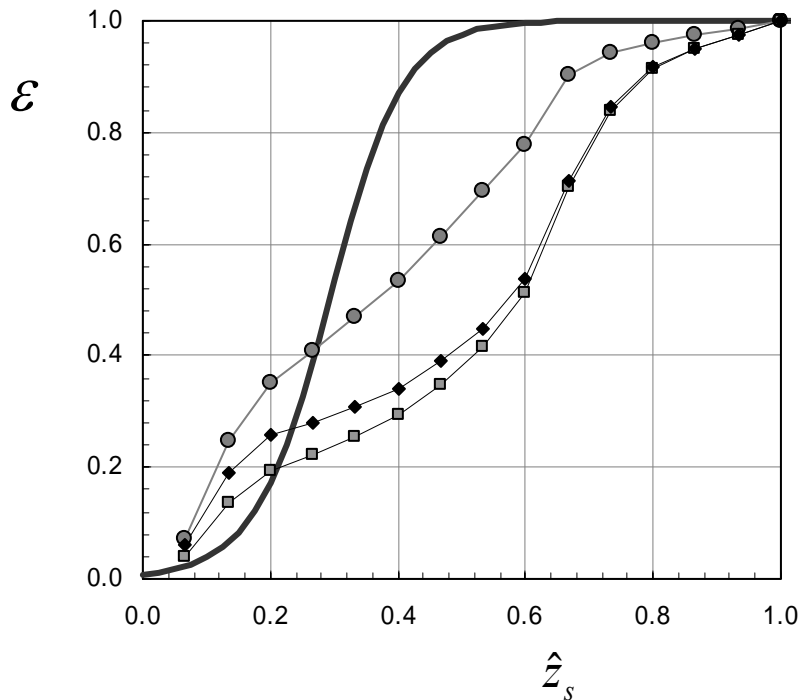


Figure 4.16. Plot showing SASEC-1 (squares), predicted using SEC-1 as the local sand elevation correction function; SASEC-2 (diamonds), predicted using no sand elevation correction function; and SASEC-3 (circles), predicted using a new local entrainment function (Figure 4.17). The solid line is SEC-3.

In order to develop a SASEC that is similar to the sand elevation correction fitted to the experimental observations in the wide channel (SEC-3), the local sand entrainment rate must exceed the full sand bed entrainment rate over some range of \hat{z}_s . A local sand elevation correction function (LOSEC) that rises steeply and peaks at some value of ε_L greater than one (Figure 4.17) produces a spatially averaged sand elevation correction that more closely matches SEC-3. The shape of the predicted spatially-averaged sand

elevation correction function (SASEC-3) is sensitive to the elevation at which the entrainment rate exceeds the full sand bed entrainment rate, but less sensitive to the magnitude by which the local entrainment rates exceeds the sand-bed entrainment rate. A function with a peak at $\hat{z}_{sL} = 0.4$ resulted in the SASEC with the closest match to SEC-3. The LOSEC shown in Figure 4.17 is made to pass through the equilibrium transport data at $\hat{z}_s < 0.25$. We suspect that sand entrainment observed at small values of \hat{z}_s will more closely approximate a LOSEC because the local sand elevations will be more accurately represented by the spatial average. The spatial average is likely to be a poor representation of local values of \hat{z}_s at $\hat{z}_s > 0.5$.

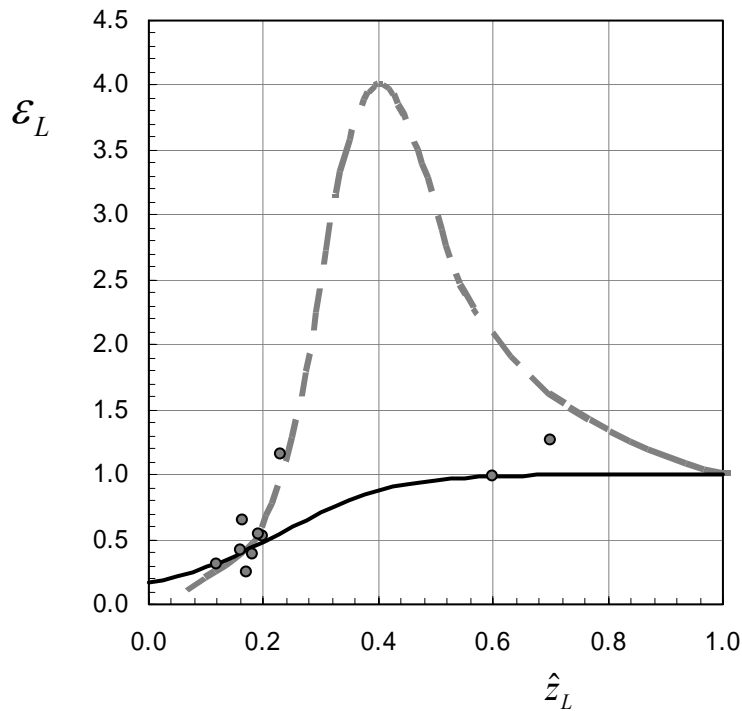


Figure 4.17. Plot showing the LOSEC function that has a peak in the local entrainment rate for elevations between $0.4r_b$ and $0.5r_b$. These functions were used to construct the predicted SASEC functions shown in Figure 4.16. The data points are for ε determined from the equilibrium transport experiments (Chapter 2).

Enhanced entrainment from bed elevations between about $0.5r_b$ and $1.0r_b$ is consistent with the distribution of sand bed elevations observed in these experiments and also consistent with the results presented in Chapter 2. Bed elevations of about $0.4r_b$ to

$0.5r_b$ mark the steep transition from the peak to the low shoulder of the bed elevation density functions (Figure 4.13). The frequency of bed elevations drops sharply over the range $0.2 r_b - 0.5r_b$. Accelerated entrainment of sand from elevations at and above this transition is one mechanism that would result in the observed distribution of local sand bed elevations. In the experiments presented in Chapter 2, we had great difficulty achieving combinations of flow and sediment feed rate that produced average bed elevations in the range $0.5r_b - 1.0r_b$. We did observe average bed elevations in this range in the main channel experiments, but only because the width of the channel allowed us to observe the segregation of the bed into bed forms and areas with sand cover less than about $0.5r_b$.

Other researchers have suggested similar patterns of entrainment based on different types of observations for conditions analogous to those considered here. Nickling and McKenna Neuman (1995) measured accelerated sand entrainment as immobile roughness elements became exposed in a deflating sand bed during aeolian transport. That observation is consistent with the form of the local sand elevation correction suggested here. Particle entrainment rates that are a function of the elevation of the sand surface relative to the height of immobile grains also explain the organization of sand patches, consistent with theories that have been proposed to explain the formation of sand stripes. McLean (1981) estimated bed stress from velocity profiles measured over sand stripes and the areas of rough bare bed between sand stripes. He reported lower stresses over the stripes than the adjacent rough bed, composed of 2 to 4 mm immobile grains. Lower stress, and relatively lower rates of entrainment, over the sand patches help to maintain the patches, whereas larger rates of entrainment from elevations less than the height of the immobile grains results in rapid deflation to a low sand bed elevation as those grains become exposed. Relatively large immobile grains, such as those used in these experiments, allow some interstitial storage of fine sediment below the region of accelerated entrainment.

Conclusions

When sand is transported in suspension over a coarse immobile bed, flow disturbance from the coarse grains alters sand entrainment rates. In order to model sand transport for these conditions, it is necessary to consider the sand bed elevation relative to the height of the immobile grains and the organization of the sand on the bed into patches. These effects can be included in a sand elevation correction function that is defined as the ratio of the rate of entrainment that occurs over a partially sand-covered bed to the rate of sand entrainment that would occur over a completely sand-covered bed. The sand elevation correction is defined as a function of the mean sand elevation scaled by the dimension of the coarse grains.

The sand elevation correction was tested against observations of transport and bed elevation change in a nonuniform transport field in a large flume with steady flow. Testing required a numerical model capable of predicting transport and bed morphodynamics under unsteady sediment supply and nonuniform bed storage. When sand entrainment is calculated at the same rate as for a full sand bed, sand evacuates from the bed too quickly. On the other hand, use of a sand elevation correction function that is based on the premise that all of the entrainment occurs from sand patches and that no entrainment occurs from interstitial spaces causes too great a restriction on the rate of particle entrainment and excessively slows sediment evacuation. The sand elevation correction function that provided the best fit to the experimental observations was one that produces greater entrainment than would occur if entrainment was derived only from sand patches, but somewhat less entrainment than suggested by the function derived from the data presented in Chapter 2.

The sand elevation correction predicts spatially averaged entrainment as a function of mean bed elevation. But because sand does not distribute evenly among large immobile grains, but organizes into patches, the local rate of sand entrainment must vary spatially. Correspondingly, there exists a local sand elevation correction that is different from the spatially-averaged sand elevation correction. Although we did not measure local entrainment directly, we were able to test different local sand elevation correction

functions according to local entrainment predicted for a known distribution of local sand bed elevations. In addition, the shape of the spatially-averaged sand elevation correction function provides some insight into the process of local entrainment in these bed conditions. The spatially-averaged sand entrainment rates that we observed indicates that local entrainment rates must exceed the full sand-bed entrainment rate for a range of local sand bed elevations between about 0.5 and 1.0 times the bed roughness height. Local rates of sand entrainment may exceed the rate that would occur over a sand bed by a factor of four or greater. Enhanced entrainment from this range of bed elevations is required to produce spatially-averaged rates of entrainment consistent with observed rates of entrainment. Accelerated particle entrainment from sand bed elevations below the height of immobile roughness elements is consistent with observations of aeolian transport among immobile roughness elements (Nickling and McKenna Neuman, 1995) and observations of near-bed stress distributions for beds with sand stripes (McLean, 1981).

REFERENCES

- Allen, J. R. L., 1968, Current Ripples: Their Relation to Patterns of Water and Sediment Motion: Amsterdam, North-Holland Publishing Company, 433 p.
- Allen, J. R. L., 1982, Sedimentary Structures: Their Character and Physical Basis: Amsterdam, Elsevier, 593 p.
- Best, J., 1996, The fluid dynamics of small-scale alluvial bedforms, *in* Carling, P. A., and Dawson, M. R., eds., *Advances in Fluvial Dynamics and Stratigraphy*, John Wiley & Sons Ltd., p. 67-125.
- Blom, A., 2003, A Vertical Sorting Model for Rivers With Non-uniform Sediment and Dunes: Veenendaal, the Netherlands, Universal Press, 267 p.
- Byrd, T. C., Furbish, D. J., and Warburton, J., 2000, Estimating depth-averaged velocities in rough channels: *Earth Surface Processes and Landforms*, v. 25, no. 2, p. 167-173.
- Carling, P. A., 1999, Subaqueous gravel dunes: *Journal of Sedimentary Research*, v. 69, p. 534-545.
- Carling, P. A., Williams, J. J., Golz, E., and Kelsey, A. D., 2000a, The morphodynamics of fluvial sand dunes in the River Rhine, near Mainz, Germany. I. Sedimentology and morphology: *Sedimentology*, v. 47, p. 227-252.
- , 2000b, The morphodynamics of fluvial sand dunes in the River Rhine, near Mainz, Germany. II. Hydrodynamics and sediment transport: *Sedimentology*, v. 47, p. 253-278.
- Celik, I., and Rodi, W., 1988, Modeling suspended sediment transport in nonequilibrium situations: *Journal of Hydraulic Engineering*, v. 114, no. 10, p. 1157-1191.
- Chiew, Y., and Parker, G., 1994, Incipient sediment motion on non-horizontal slopes: *Journal of Hydraulic Research*, v. 32, no. 5, p. 649-660.
- Chiew, Y. M., 1991, Bed features in nonuniform sediments: *Journal of Hydraulic Engineering*, v. 117, no. 1, p. 116-120.
- Colombini, M., 1993, Turbulence-driven secondary flows and formation of sand ridges: *Journal of Fluid Mechanics*, v. 254, p. 701-719.
- Colombini, M., and Parker, G., 1995, Longitudinal streaks: *Journal of Fluid Mechanics*, v. 304, p. 161-183.
- Cui, Y., Parker, G., Lisle, T. E., Gott, J., Hansler-Ball, M. E., Pizzuto, J. E., Allmendinger, N. E., and Reed, J. M., 2003, Sediment pulses in mountain rivers: 1. Experiments: *Water Resources Research*, v. 39, no. 9.
- Culbertson, J. K., 1967, Evidence of secondary circulation in an alluvial channel, U.S. Geological Survey Professional Paper 575-D, p. D214-D216.
- Dietrich, W. E., 1982, Settling velocity of natural particles: *Water Resources Research*, v. 18, no. 6, p. 1615-1626.
- Einstein, H. A., and Barbarossa, N. L., 1952, River channel roughness: *Transactions, American Society of Civil Engineers*, v. 117, p. 1121-1146.
- Einstein, H. A., and Chien, N., 1953, Transport of sediment mixtures with large ranges of grain sizes: University of California Institute of Engineering Research.
- Engelund, F., and Fredsoe, J., 1976, A sediment transport model for straight alluvial channels: *Nordic Hydrology*, v. 7, p. 293-306.

- Engelund, F., and Hansen, E., 1967, A monograph on sediment transport in alluvial streams: Copenhagen, Denmark, Teknisk Forlag.
- Garcia, M., and Parker, G., 1991, Entrainment of bed sediment into suspension: *Journal of Hydraulic Engineering*, v. 117, no. 4, p. 414-435.
- Grams, P. E., and Schmidt, J. C., 1999, Geomorphology of the Green River in the eastern Uinta Mountains, Dinosaur National Monument, Colorado and Utah, *in* Miller, A. J., and Gupta, A., eds., *Varieties of Fluvial Form*: Chichester, John Wiley & Sons Ltd, p. 81-111.
- Hirano, M., 1971, River bed degradation with armouring: *Transactions, Jap. Soc. Civ. Eng.*, v. 3, p. 194-195.
- Howard, A., and Dolan, R., 1981, Geomorphology of the Colorado River in the Grand Canyon: *Journal of Geology*, v. 89, no. 3, p. 269-298.
- Ikeda, S., 1981, Self-formed straight channels in sandy beds: *Journal of the Hydraulics Division, Proceedings of the American Society of Civil Engineers*, v. 107, p. 389-406.
- Itakura, T., and Kishi, T., 1980, Open channel flow with suspended sediments: *Journal of the Hydraulics Division, Proceedings of the American Society of Civil Engineers*, v. 106, no. HY8, p. 1325-1343.
- Kim, S. C., Friedrichs, C. T., Maa, J. P. Y., and Wright, L. D., 2000, Estimating Bottom Stress in Tidal Boundary Layer from Acoustic Doppler Velocimeter Data: *Journal of Hydraulic Engineering*, v. 126, no. 6, p. 399-406.
- Kleinhans, M. G., Wilbers, A. W. E., De Swaaf, A., and Van Den Berg, J. H., 2002, Sediment supply-limited bedforms in sand-gravel bed rivers: *Journal of Sedimentary Research*, v. 72, no. 5, p. 629-640.
- Larsen, I. J., Schmidt, J. C., and Martin, J. A., 2004, Debris-fan reworking during low-magnitude floods in the Green River canyons of the eastern Uinta Mountains, Colorado and Utah: *Geology*, v. 32, no. 4, p. 309-312.
- Lisle, T. E., and Lewis, J., 1992, Effects of sediment transport on survival of salmonid embryos in a natural stream: A simulation approach: *Can. J. Fish. Aquat. Sci.*, v. 49, p. 2337-2344.
- Lisle, T. E., Pizzuto, J. E., Ikeda, H., Iseya, F., and Kodama, Y., 1997, Evolution of a sediment wave in an experimental channel: *Water Resources Research*, v. 33, no. 8, p. 1971-1981.
- McCulloch, D. S., and Janda, R. J., 1964, Subaqueous river channel barchan dunes: *Journal of Sedimentary Petrology*, v. 34, p. 694.
- McLean, S. R., 1981, The role of non-uniform roughness in the formation of sand ribbons: *Marine Geology*, v. 42, p. 49-74.
- McLean, S. R., Wolfe, S. R., and Nelson, J. M., 1999, Predicting boundary shear stress and sediment transport over bed forms: *Journal of Hydraulic Engineering-Asce*, v. 125, no. 7, p. 725-736.
- Meade, R. H., Yuzyk, T. R., and Day, T. J., 1990, Movement and storage of sediment in rivers of the United States and Canada, *in* Wolman, M. G., and Riggs, H. C., eds., *Surface Water Hydrology: The Geology of North America*: Boulder, CO, Geological Society of America, p. 255-280.
- Middleton, G. V., and Southard, J. B., 1984, *Mechanics of Sediment Movement*, *in* Short Course No. 3, Providence, Rhode Island, p. 401.

- Nelson, J. M., Emmett, W. W., and Smith, J. D., 1991, Flow and sediment transport in rough channels, *in* Fifth Federal Interagency Sedimentation Conference, Las Vegas, Nevada.
- Nelson, J. M., Shreve, R. L., McLean, S. R., and Drake, T. G., 1995, Role of near-bed turbulence structure in bed load transport and bed form mechanics: *Water Resources Research*, v. 31, no. 8, p. 2071-2086.
- Nickling, W. G., and McKenna Neuman, C., 1995, Development of deflation lag surfaces: *Sedimentology*, v. 42, p. 403-414.
- Parker, G., 1978, Self-formed straight rivers with equilibrium banks and mobile bed. Part 2. the gravel river: *Journal of Fluid Mechanics*, v. 89, p. 127-146.
- Parker, G., and Anderson, A. G., 1977, Basic principles of river hydraulics: *Journal of the Hydraulics Division, Proceedings of the American Society of Civil Engineers*, v. 103, no. HY9, p. 1077-1087.
- Parker, G., Paola, C., and Leclair, S., 2000, Probabilistic Exner sediment continuity equation for mixtures with no active layer: *Journal of Hydraulic Engineering*, v. 126, no. 11, p. 818-826.
- Patankar, S. V., 1980, Numerical heat transfer and fluid flow, Series in computational and physical processes in mechanics and thermal sciences, Taylor & Francis, 197 p.
- Rouse, H., 1936, Modern conceptions of the mechanics of fluid turbulence: *Proceedings of the American Society of Civil Engineers*, p. 463-543.
- Rubin, D. M., and Topping, D. J., 2001, Quantifying the relative importance of flow regulation and grain size regulation of suspended sediment transport alpha and tracking changes in grain size of bed sediment beta: *Water Resources Research*, v. 37, no. 1, p. 133-146.
- Schmeeckle, M. W., and Nelson, J. M., 2003, Direct numerical simulation of bedload transport using a local, dynamic boundary condition: *Sedimentology*, v. 50, no. 2, p. 279-301.
- Schmidt, J. C., 1999, Summary and synthesis of geomorphic studies conducted during the 1996 controlled flood in Grand Canyon, *in* Webb, R. H., Schmidt, J. C., Valdez, R. A., and Marzolf, G. R., eds., *The 1996 Controlled Flood in Grand Canyon scientific experiment and management demonstration*, American Geophysical Union Monograph.
- Schmidt, J. C., and Rubin, D. M., 1995, Regulated streamflow, fine-grained deposits, and effective discharge in canyons with abundant debris fans, *in* Costa, J. E., Miller, A. J., Potter, K. W., and Wilcock, P. R., eds., *Natural and anthropogenic influences in fluvial geomorphology*, American Geophysical Union, p. 177-195.
- Smith, D. J., and McLean, S. R., 1977, Spatially averaged flow over a wavy surface: *Journal of Geophysical Research*, v. 82, no. 12, p. 1735-1746.
- Southard, J. B., 1991, Experimental determination of bed-form stability: *Annu. Rev. Earth Planet. Sci.*, v. 19, p. 423-455.
- Southard, J. B., and Boguchwal, A. L., 1990, Bed configuration in steady unidirectional water flows. Part 2. Synthesis of flume data: *Journal of Sedimentary Petrology*, v. 60, p. 658-679.
- Stansby, P. K., and Awang, M. A., 1998, Response time analysis of suspended sediment transport: *Journal of Hydraulic Research*, v. 36, no. 3, p. 327-338.

- Topping, D. J., 1997, Physics of flow, sediment transport, hydraulic geometry, and channel geomorphic adjustment during flash floods in an ephemeral river, the Paria River, Utah and Arizona [Ph.D. thesis]: University of Washington, 406 p.
- Topping, D. J., Rubin, D. M., and Vierra, L. E. J., 2000, Colorado River sediment transport 1. Natural sediment supply limitation and the influence of Glen Canyon Dam: *Water Resources Research*, v. 36, no. 2, p. 515-542.
- Trimble, S. W., 1997, Contribution of Stream Channel Erosion to Sediment Yield from an Urbanizing Watershed: *Science*, v. 278, no. 5342, p. 1442-1444.
- Van Den Berg, J. H., and Van Gelder, A., 1993, A new bedform stability diagram, with emphasis on the transition of ripples to plane bed in flows over fine sand and silt, *International Association of Sedimentologists, Special Publication 17*, p. 11-21.
- Vanoni, V. A., 1975, *Sedimentation Engineering*, American Society of Civil Engineers.
- van Rijn, L. C., 1984, Sediment transport, part II: Suspended load transport: *Journal of Hydraulic Engineering*, v. 110, no. 11, p. 1613-1641.
- Voulgaris, G., and Trowbridge, J. H., 1998, Evaluation of the Acoustic Doppler Velocimeter (ADV) for Turbulence Measurements: *Journal of Atmospheric and Oceanic Technology*, v. 15, no. 1, p. 272-289.
- Webb, R. H., Pringle, P. T., and Rink, G. R., 1989, Debris flows from tributaries of the Colorado River, Grand Canyon National Park, Arizona, Professional Paper 1492, U. S. Geological Survey, p. 39.
- Wiberg, P. L., and Smith, J. D., 1991, Velocity distribution and bed roughness in high-gradient streams: *Water Resources Research*, v. 27, no. 5, p. 825-838.
- Wiele, S. M., Graf, J. B., and Smith, J. D., 1996, Sand deposition in the Colorado River in the Grand Canyon from flooding of the Little Colorado River: *Water Resources Research*, v. 32, p. 3579-3596.
- Willgoose, G., Bras, R. L., and Rodriguez-Iturbe, I., 1990, A model of river basin evolution: *EOS, Transactions American Geophysical Union*, v. 71, no. 47, p. 1806-1807.
- Wolman, M. G., and Brush, L. M., 1961, Factors controlling the size and shape of stream channels in coarse noncohesive sands, Professional Paper 282-G, U.S. Geological Survey Professional Paper 282-G.
- Wright, S., and Parker, G., 2004, Flow resistance and suspended load in sand-bed rivers: simplified stratification model: *Journal of Hydraulic Engineering*, v. 130, no. 8, p. 796-805.

APPENDICES

Appendix A. Collection and Processing of Acoustic-Doppler Velocimeter Data from the Tilting Bed Experiments

For each of the flow rates used in the experiments conducted in the tilting-bed flume, a set of detailed velocity measurements was made with the acoustic-Doppler velocimeter (ADV). Velocity profiles were measured directly over a hemisphere in the center of the channel at the sediment sampling location and on the right side of the channel one row downstream from the sampling location. A third profile was collected over the gap between two spheres one row downstream from the sediment sampling location. For one flow rate, centerline velocity profiles were collected at 1-m intervals along the length of the flume to test for flow uniformity and secondary flow patterns. Each profile consisted of seven velocity measurements made 0.5, 1.0, 2.0, 5.0, 10.0, 20.0, and 30.0 cm above the height of the hemisphere tops. Individual velocity measurements were collected at a 25 Hz sampling rate for a period of one minute. The (SonTek 10-MHz ADV measured velocities in three orthogonal coordinates within a 0.2 cm³ sample volume.

The raw ADV data were processed to remove spikes and correct for instrument misalignment. Spikes in ADV data are caused by aliasing of the Doppler signal that may occur when the phase shift between the outgoing and incoming pulse lie outside the range between -180° and $+180^\circ$, causing ambiguity in the received signal. This situation can occur when the velocity exceeds the set velocity range or as a result of signal contamination from previous pulses reflected from complex bottom geometries. Because measured velocities never approached the limit of the sampling range (2.50 m/s), all of the spikes in the ADV records are likely due to the bottom geometry. These spikes were removed by a phase-space threshold despiking method described by Goring and Nikora (2002) and implemented in the WinADV software by Wahl (2000, 2003). Goring and Nikora (2002) found this method the most satisfactory in detecting anomalous spikes while leaving intact true spikes due to turbulent fluctuations in the velocity. Spikes detected by this method were removed from the record.

References

- Goring, D. G., and Nikora, V. I., 2002, Despiking acoustic doppler velocimeter data: Journal of Hydraulic Engineering, v. 128, no. 1, p. 117-126.
- Wahl, T. L., 2000, Analyzing ADV Data Using WinADV, in Joint Conference on Water Resources Engineering and Water Resources Planning and Management, Minneapolis, Minnesota.
- Wahl, T. L., 2003, Discussion of "Despiking acoustic doppler velocimeter data": Journal of Hydraulic Engineering, v. 129, no. 6.

Appendix B. Collection and Processing of Acoustic-Doppler Velocimeter Data from the Main Channel Experiments

Data collection

Full velocity profile measurements consisted of eight measurement positions located 1, 2, 3.5, 6, 10, 15, 25, and 40 cm above a hemisphere top. For the low flow conditions ($\sim 29 \text{ ft}^3/\text{s}$), profiles were collected at five cross-channel positions at six locations along the flume: 1.2, 3.0, 5.1, 7.0, 10.9, and 15.1 m upstream from the downstream end of the test section. The five cross-channel positions are 45.5, 91.5, 137, 183, and 228.5 cm from the left sidewall. These positions correspond with the positions of other instruments. Four additional velocity profiles were collected at the center channel position only at 19.1, 23.0, 31.1, and 37.2 m in the test section. All five profiles at $X = 5.1 \text{ m}$ were repeated. All measurements were made at sample rate of 50 Hz for 1 min or longer.

Prior to the above measurements, profiles consisting of measurements made for 3 minutes or longer were made at all five cross-channel positions at two locations: 5.1 and 7.0 m in the test section. These data were collected with the HorizonADV software, which I found incorrectly reported measurement elevations. Instead of the above elevations, these measurements were made at approximately: 0.6, 1.6, 3.1, 5.5, 9.4, 14.2, 23.9, and 38.5 cm above the hemisphere tops.

Velocity profiles for the high flow condition ($\sim 44 \text{ ft}^3/\text{s}$) were collected at all cross-channel positions at 1.2, 3.0, 5.1, and 7.0 m in the test section. Center-position profiles were also collected at 10.9, 15.1, 19.1, 23.0, and 31.1 m.

Table B1 lists the dates of ADV measurements and the corresponding discharges for each measurement. Flow in the main channel was not usually precisely the same from one run to the next, and also changed during the course of a long run when Mississippi river stage was not constant. For the runs conducted at the low flow rate, discharge ranged from 27.7 to 31.0 ft^3/s and for the high flow rate the discharge ranged from 44.0 to 46.3 ft^3/s . This variability and the official discharge for each ADV measurement are listed in Table B2.

All ADV data were collected with a SonTek 16 MHz MicroADV. This instrument has a sampling rate of up to 50 Hz and a velocity resolution of 0.01 cm/s up to 250 cm/s. Reported accuracy is 1% of measured velocity. The sampling volume is centered 4.67 cm below the probe tip and the sampling volume is 0.09 cc. The data were processed to remove spikes using the same methods described in Appendix A.

Velocity profiles

Figure B1 shows all the velocity profiles collected during the low flow ADV runs (excluding the 3-min data) and figure B2 shows the profiles collected during the high flow ADV runs. The profiles indicate a well-mixed area near the bed where the profiles are nearly vertical, up to 2 to 3.5 cm above the hemisphere tops. Velocities from 3.5 to 40 cm fit a log-linear relation.

Table B1. Summary of Main Channel ADV data.

| Date | Time | Q (ft ³ /s) | Run | X (m) | Y (cm) | Z (cm) | length (min) | Rate (hz) | # Files |
|--------|------------------|---------------------------|-----|----------|---------------------|--------|-----------------|--------------|------------|
| 5-May | | 29.8 | adv | 15.1 | 52, 137, 222 | 40 | 3 + | 50 | 4 |
| 5-May | | 29.8 | adv | 19.1 | 22,52,137,222 | 10,40 | 3 + | 50 | 12 |
| 5-May | | 29.8 | adv | 30.0 | 137 | 40 | 16 + | 50 | 1 |
| 6-May | | 29.8 | adv | 5.1 | all | all | 3 + | 50 | 40 |
| 6-May | | 29.8 | adv | 7.0 | all | all | 3 + | 50 | 42 |
| 10-May | | 28.4 | adv | 5.1 | all | all | 1 | 50 | 40 |
| 10-May | | 28.4 | adv | 7.0 | all | all | 1 | 50 | 40 |
| 10-May | | 28.4 | adv | 10.9 | all | all | 1 | 50 | 40 |
| 10-May | | 28.4 | adv | 15.1 | all | all | 1 | 50 | 40 |
| 10-May | | 28.4 | adv | 19.1 | 137 | all | 1 | 50 | 8 |
| 10-May | | 28.4 | adv | 23.0 | 137 | all | 1 | 50 | 8 |
| 10-May | | 28.4 | adv | 31.1 | 137 | all | 1 | 50 | 8 |
| 10-May | | 28.4 | adv | 37.2 | 137 | all | 1 | 50 | 8 |
| 11-May | | 28.4 | adv | 1.2 | all | all | 1 | 50 | 40 |
| 11-May | | 28.4 | adv | 3.0 | all | all | 1 | 50 | 40 |
| 11-May | | 28.4 | adv | 5.1 | all | all | 1 | 50 | 40 |
| 13-May | | 28.3 | 1A | 7.5 | 137 | 2 | 91.1 | 10 | 1 |
| 24-May | | 31.0 | 1D | 7.5 | 137 | 2 | 365 | 10 | 1 |
| 25-May | | 31.0 | 2A | 7.5 | 137 | 2 | 88.4 | 10 | 1 |
| 27-May | | 31.0 | 2B | 7.5 | 45.5, 137, 222.5 | siphon | 1 + | 50 | 15 |
| 27-May | | 31.0 | 2B | 7.4 | 137 | four | 8 + | 50 | 4 |
| 28-May | | 46.3 | 2C | 7.5 | 45.5, 137, 222.5 | siphon | 0.5 + | 50 | 16 |
| 1-Jun | | 29.5 | 3A | 7.5 | 137 | 2 | 89 | 10 | 1 |
| 4-Jun | | 29.5 | 3B | 7.5 | 137 | 2 | 208 | 10 | 1 |
| 8-Jun | | 28.0 | 3C | 7.5 | 137 | 2 | 128.3 | 10 | 1 |
| 9-Jun | | 28.0 | 3D | 7.5 | 137 | 2 | 240.3 | 10 | 1 |
| 10-Jun | | 42.7 | 3E | 7.5 | 137 | 2 | 160.5 | 10 | 1 |
| 15-Jun | | 43.9 | 4A | 7.5 | 137 | 2 | 91.3 | 10 | 1 |
| 16-Jun | | 45.1 | 4B | 7.5 | 137 | 2 | 53 | 10 | 1 |
| 17-Jun | | 44.3 | 4C | 7.5 | 137 | 2 | 84.5 | 10 | 1 |
| 18-Jun | | 44.0 | 4D | 7.5 | 137 | 2 | 118.5 | 10 | 1 |
| 21-Jun | | 43.4 | 4E | 7.5 | 137 | 2 | 212.5 | 10 | 1 |
| 22-Jun | | 43.5 | 5A | 7.5 | 137 | 2 | 92.5 | 10 | 1 |
| 23-Jun | | 43.0 | 5B | 7.5 | 137 | 2 | 33.5 | 10 | 1 |
| 24-Jun | 12:55 - 15:32 | 45.0 | adv | 1.2 | all | all | 1 | 50 | 40 |
| 24-Jun | 15:54 - 16:28 | 47.1 | adv | 3.0 | 42, 91.5 | all | 1 | 50 | 16 |
| 25-Jun | 8:40 - 9:50 | 44.9 | adv | 3.0 | 137, 183, 222.5 | all | 1 | 50 | 24 |
| 25-Jun | 10:13 - 12:24 | 43.3 | adv | 5.1 | all | all | 2 | 50 | 40 |
| 25-Jun | 13:07 - 14:35 | 43.2 | adv | 7.0 | all | all | 1 | 50 | 40 |
| 25-Jun | 14:53 - 16:23 | 43.2 | adv | 10.9 | 42, 91.5, 137 | all | 1 | 50 | 28 |
| 28-Jun | 10:27 - 10:42 | 45.0 | adv | 10.9 | 137 | all | 1 | 50 | 8 |

| | | | | | | | | | |
|--------|---------------|------|-----|------|-----|-----|---|----|----|
| 28-Jun | 10:55 - 11:34 | 45.0 | adv | 15.1 | 137 | all | 1 | 50 | 8 |
| 28-Jun | 11:42 - 11:56 | 45.0 | adv | 19.1 | 137 | all | 1 | 50 | 8 |
| 28-Jun | 12:39 - 12:53 | 45.0 | adv | 23.0 | 137 | all | 1 | 50 | 8 |
| 28-Jun | 12:59 - 13:12 | 45.0 | adv | 31.1 | 137 | all | 1 | 50 | 8 |
| 28-Jun | 13:31 - 13:58 | 45.0 | adv | 7.4 | 137 | Gap | 2 | 50 | 11 |
| 28-Jun | 13:55 - 16:29 | 45.0 | adv | 5.1 | all | all | 1 | 50 | 40 |
| 28-Jun | 14:16 - 14:36 | 45.0 | adv | 7.3 | 137 | Gap | 2 | 50 | 11 |
| 29-Jun | 8:22 - 8:52 | 28.9 | adv | 7.4 | 137 | Gap | 2 | 50 | 11 |
| 29-Jun | 8:58 - 9:27 | 28.9 | adv | 7.3 | 137 | Gap | 2 | 50 | 11 |

Run indicates whether the measurement was made during an experimental run segment or during a dedicated run for collecting ADV data. X is the distance from downstream end of test section; Y is the distance from left sidewall; Z is the elevation above the plane defined by the tops of the hemispheres. All refers to Y positions of 45.5, 91.5, 137, 183, and 228.5 cm, and Z positions of 1, 2, 3.5, 6, 10, 15, 25, and 40 cm, respectively. Siphon refers to Z positions of 1, 2, 6, 15, and 40 cm. Gap refers to all z positions and the additional z positions of 0, -1, and -3 cm. Length is the duration of ADV sample time and rate is the rate of ADV data collection.

Table B2. Variability of discharge among ADV and experimental runs.

| Discharge Variability | | Q (ft³/s) | | | |
|------------------------------|----------------------------|-----------------------------|------------|--------------|--|
| Event | AVG | Max | Min | Range | |
| ADV Low Flow (pre-runs) | 28.7 | 29.8 | 28.0 | 1.8 | |
| Low Flow Runs | 29.0 | 31.0 | 27.7 | 3.3 | |
| High Flow Runs | 44.0 | 46.3 | 42.7 | 3.6 | |
| ADV High Flow (post-runs) | 44.7 | 47.1 | 43.2 | 4.0 | |
| ADV Low Flow (post-runs) | 28.9 | 29.0 | 28.7 | 0.4 | |
| | | | | | |
| | Q (m³/s) | | | | |
| Event | AVG | Max | Min | Range | |
| ADV Low Flow (pre-runs) | 0.81 | 0.84 | 0.79 | 0.05 | |
| Low Flow Runs | 0.82 | 0.88 | 0.78 | 0.09 | |
| High Flow Runs | 1.25 | 1.31 | 1.21 | 0.10 | |
| ADV High Flow (post-runs) | 1.27 | 1.33 | 1.22 | 0.11 | |
| ADV Low Flow (post-runs) | 0.82 | 0.82 | 0.81 | 0.01 | |
| | | | | | |
| | U (m/s) | | | | |
| Event | AVG | Max | Min | Range | |
| ADV Low Flow (pre-runs) | 0.49 | 0.51 | 0.48 | 0.03 | |
| Low Flow Runs | 0.50 | 0.53 | 0.48 | 0.06 | |
| High Flow Runs | 0.76 | 0.80 | 0.74 | 0.06 | |
| ADV High Flow (post-runs) | 0.77 | 0.81 | 0.74 | 0.07 | |
| ADV Low Flow (post-runs) | 0.50 | 0.50 | 0.49 | 0.01 | |

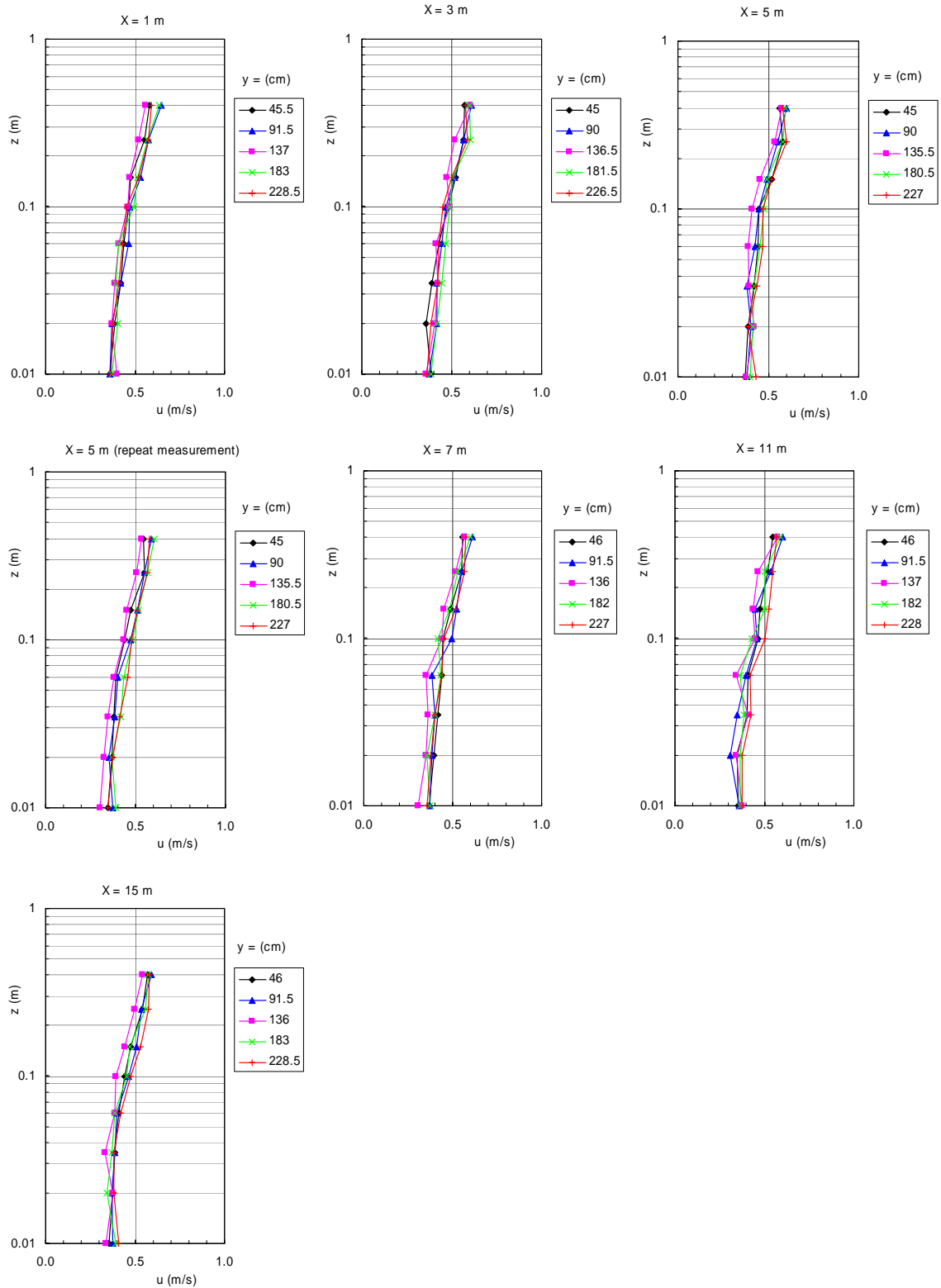


Figure B1. Velocity profiles for low flow conditions.

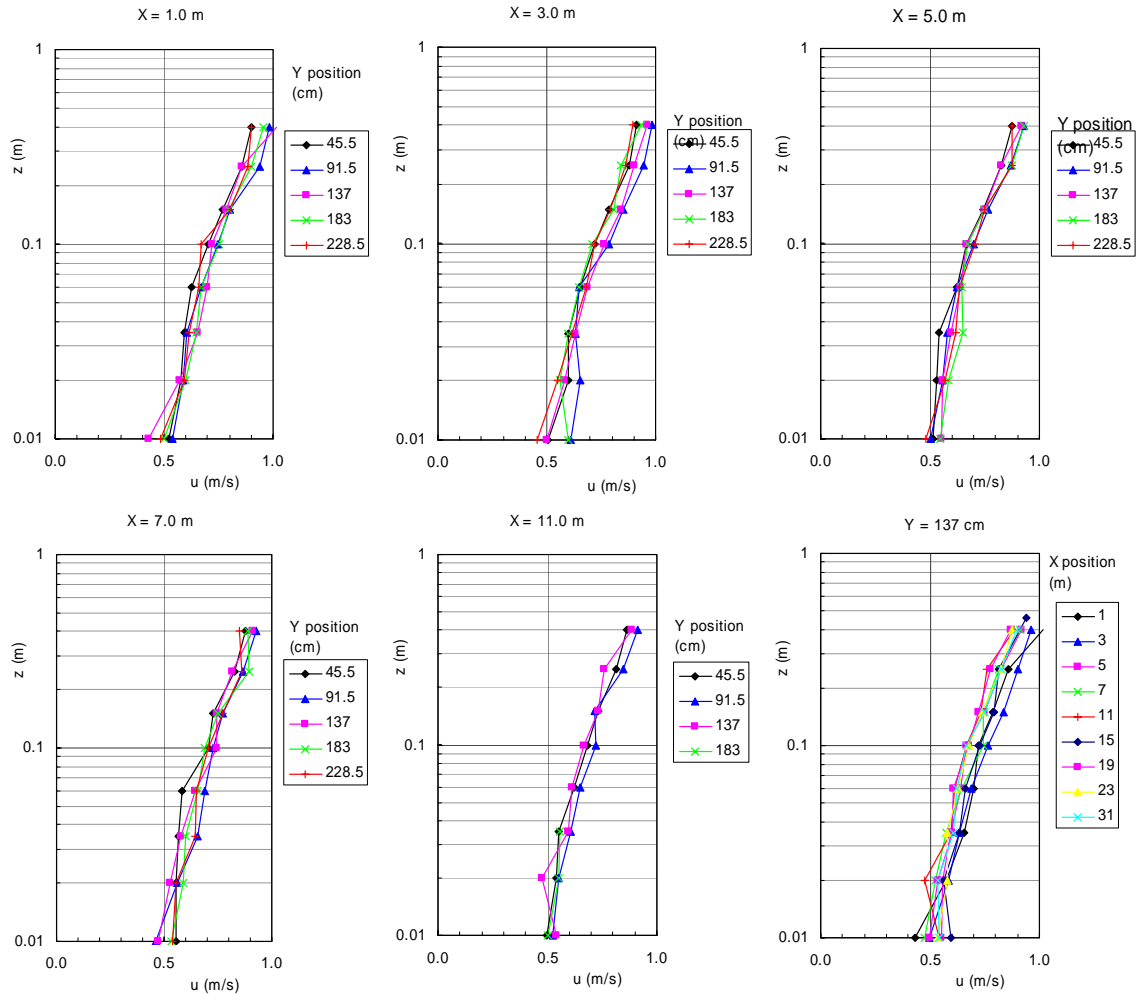


Figure B2. Velocity profiles for high flow conditions.

Appendix C. Bed sediment grain size from Main Channel experiments.

Sample identifications are given in Table C1 and the grain size distribution for each sample is given in Tables C2-C6. ID is the run segment and sample number. X is distance from downstream end of test section, in meters. Y is distance from the left side of the channel, in meters. Facies indicates samples from patches (includes sand stripes and barchan dunes), non-patches (spaces between coarse grains). Type indicates whether a surface sample (upper 0.5 cm), sub-surface (0.5 to 2 cm below the surface), rest (2 cm below the surface to the bottom), or all (entire bed thickness). Z is the elevation of the top of the sample above the channel bottom (for core samples only).

[these data tables are available in the original copy of this dissertation, in electronic form on the accompanying CD, or from the author, upon request]

Appendix D. Grain size of suspended sediment samples.

Grain size distributions are given in Table D1. Each sample in this table is a composite of samples collected at three cross-channel positions for the elevation of 2 cm above the hemispheres. The ID lists the Run segment and the sample event. The corresponding run time for each event is listed in Table D2. All data are for sand fraction and exclude particles finer than 0.062 mm.

[these data tables are available in the original copy of this dissertation, in electronic form on the accompanying CD, or from the author, upon request]

Appendix E. Sampling of Suspended Sediment in Main Channel Experiments

Suspended sediment sampling and data analysis

Direct measurements of sediment concentration were made during each run segment by collecting water samples through isokinetic siphon sampling tubes. The tube inlets were positioned 5.17 m upstream from the downstream end of the test section (22.17 m from downstream end of flume) in three cross-channel positions and at five elevations above the hemisphere tops. The inlets were positioned directly above hemisphere tops. The three cross-channel positions were 44, 136, and 227 cm from the left sidewall. The tube inlets were positioned 1, 2, 6, 15, and 40 cm above the hemisphere tops.

The samples were collected by two different methods. In the standard (std) method (Table E1), a siphon in each tube was started with a syringe and let run for a period of time. The samples were then collected at the indicated time for the indicated duration by placing a tray containing the sample collection jars under the tube outlets. Usually all rakes were sampled simultaneously. This method was used in runs 1a-1c and 3e-5b, for a total of 415 out of the 725 individual samples collected.

The other main sampling method was the “purge and draw” method (P&D). In this method the siphon in each tube was started shortly before each sample was collected, then each tube was purged shortly before the sample was collected. Tubes were allowed to run 30-60 s before sample was collected (30 s is minimum time for water added in purge to drain back out). Samples were collected for indicated period, usually one rake at a time. Collection cups were removed at end of sample period and plugs were inserted in tube ends. Following sample, a specified amount of water was drawn out of tubes and added to sample (usually 55 cc). For some of the P&D samples, the syringe was then cleaned out, adding a specified amount of tap water (usually 10 cc). This method was used in runs 1d-3e, for a total of 305 individual samples.

Sample Processing

Following sample collection, each labeled sample container was capped until ready for analysis. For analysis, the cap was removed and the total weight of the jar and

contents was recorded. The samples were then placed in a drying oven at low temperature and allowed to evaporate until only dry sand remained in the jar. The jar and sand were weighed, then the sand and jar were each weighed separately. The sand was retained for grain-size analysis. Four variations of this method were used throughout the experiments, because there were some errors in sample processing. Method A was the standard and preferred method.

Table E1. Methods of suspended sample data collection.

| Method | Description | Number |
|--------|--|--------|
| A | Jar with water and sand, dry jar with sand, and empty jar weighed to 0.01 g. Sand only weighed to 0.0001 g with precision balance. 662 samples | 662 |
| B | Jar with water and sand weighed to 0.01 g. Sand only weighed to 0.0001 g with precision balance. (can't double check sand weight). 20 samples | 20 |
| C | Jar with water and sand, dry jar with sand, and empty jar weighed to 0.01 g. No measurement of sand only. 7 samples | 7 |
| D | Jar with water and sand, dry jar with sand, and empty jar weighed to 0.1 g. No measurement of sand only. 36 samples | 36 |

The concentration of sand in each sample (in mg/l) was then calculated as the sand weight divided by the water volume. The concentrations measured at each elevation were then integrated over the flow depth to determine the mean concentration for the channel (each rake was treated as though it represented the full channel width). The mean concentrations for the three rakes were then averaged to determine the mean concentration for the sample event, which consists of 15 individual samples. The final concentrations are listed in Table E2, omitting all poor and questionable data.

[Table E2 is available in the original copy of this dissertation, in electronic form on the accompanying CD, or from the author, upon request]

Sand concentration from LISST instruments

Data Collection

The LISST uses laser transmission data to measure sediment concentrations and grain size in a small fixed sample volume. The LISST-100 (L-100) was mounted in the center of the channel (136.5 cm from left wall). The instrument was positioned over an interstitial space, sampling 11-16 cm from the top of the hemispheres. For Run 3C only the L-100 was located 27 m upstream from the downstream end of the test section, mounted at the same elevation relative to hemisphere tops. For all other runs the L-100 was mounted 3 m upstream from the downstream end of the test section. The L-100 provides as output total volume conc (uL/L), sand volume conc (uL/L), and sand mean diameter (um).

The LISST-25X (L-25X) also uses laser transmission data to measure sediment concentrations and grain size in a small fixed sample volume. Two L-25X units were used. One was mounted 44 cm from the left wall (left) and the other was mounted 227 m from the left wall (right). These instruments were also mounted above interstitial spaces, with sample volumes measuring from 4 to 5 cm above the tops of the hemispheres. For Run 3C only the L-25X units were located 27 m upstream from the downstream end of the test section. For all other runs the instruments were mounted 3 m upstream from the downstream end of the test section. The L-25X provides as output total volume conc (uL/L), total mean diameter (um), transmission, sand volume conc (uL/L), and sand mean diameter (um).

Data Processing

All three LISST instruments were configured to store measurements at 15 s intervals throughout each run segment. There were a few periods when data were not collected because of instrument error, battery failure, or human error. During the periods

that the instrument were running, there were frequent periods during which bad data were collected, resulting mainly from organic material collecting in the instrument sampling chamber. This was monitored during runs, and the sampling chambers were cleaned whenever this problem was identified.

The data from each of the LISST units was processed by removing upward and downward spikes. Spikes were identified by constructing a 10-min moving average and comparing each individual measurement to this average. Values greater than the moving average by a factor of 1.25 and less than the moving average by a factor of 0.70 were removed from the data. After the extreme values were removed, a 10-min moving average was then applied to the filtered data. This provides a reasonable looking time series of concentration for most of the run segments.

For comparison with concentrations measured by siphon, the 10-min average of the filtered concentrations were extracted for times corresponding to the time that siphon samples were collected.

Results

The time series of filtered data with 10-min average concentrations from each of the LISST instruments for runs 1, 2, and 5 are shown in Figure E1. During Runs 3 and 4, the instruments fouled repeatedly, resulting in poor data quality. The concentrations determined by suspended sediment sample at 6 cm are also shown in each plot. The vertical line in each plot marks the transition between run segments.

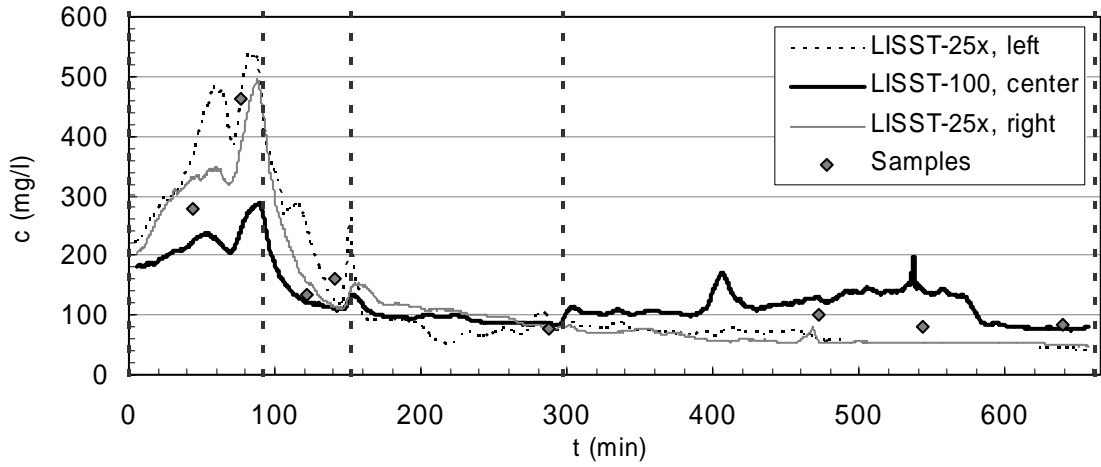


Figure E1a. Run 1 suspended sediment concentrations from LISST instruments.

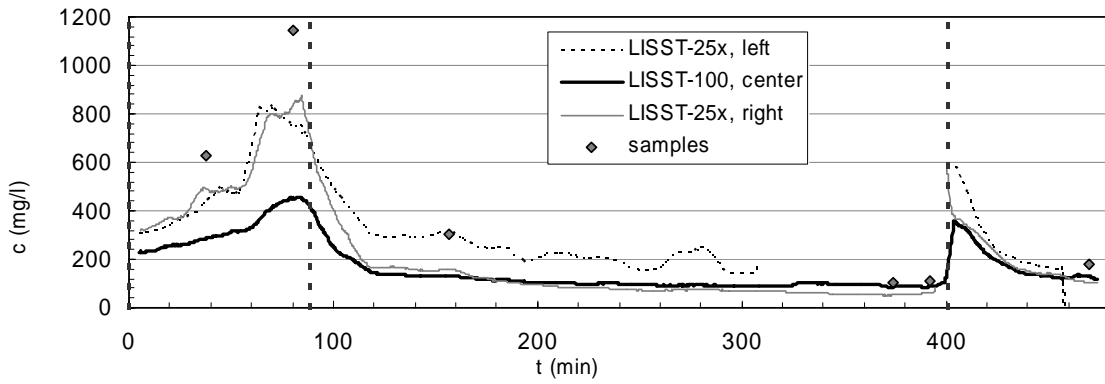


Figure E1b. Run 2 suspended sediment concentrations from LISST instruments.

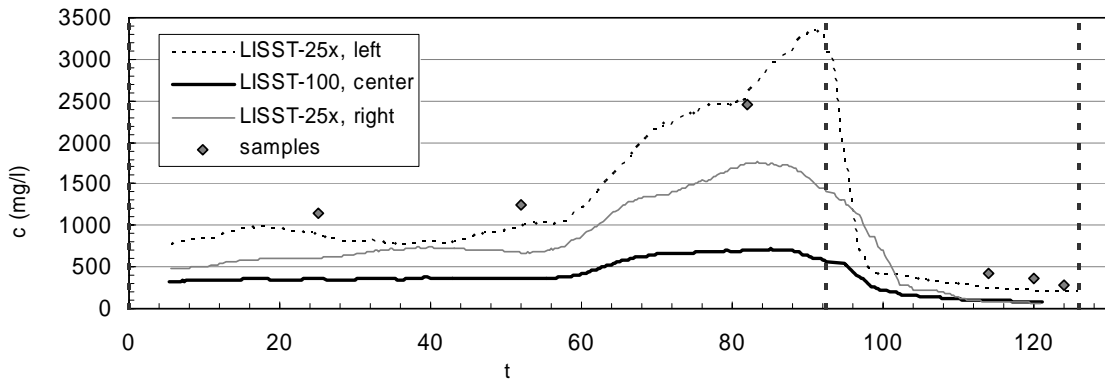


Figure E1c. Run 5 suspended sediment concentrations from LISST instruments.

Appendix F. Profiles of Bed Topography from Main Channel Experiments

This appendix contains plots of all channel cross-section profiles of measured sand bed elevations from the Main Channel experiments. The dashed line indicates the elevation of the hemisphere tops. Each plot contains the average of all measurements made in the 4.7 m bed segment that is centered 17.1 m upstream from the downstream end of the test section. The axes indicate distance from left sidewall y , and elevation above the bed at the base of the hemispheres z .

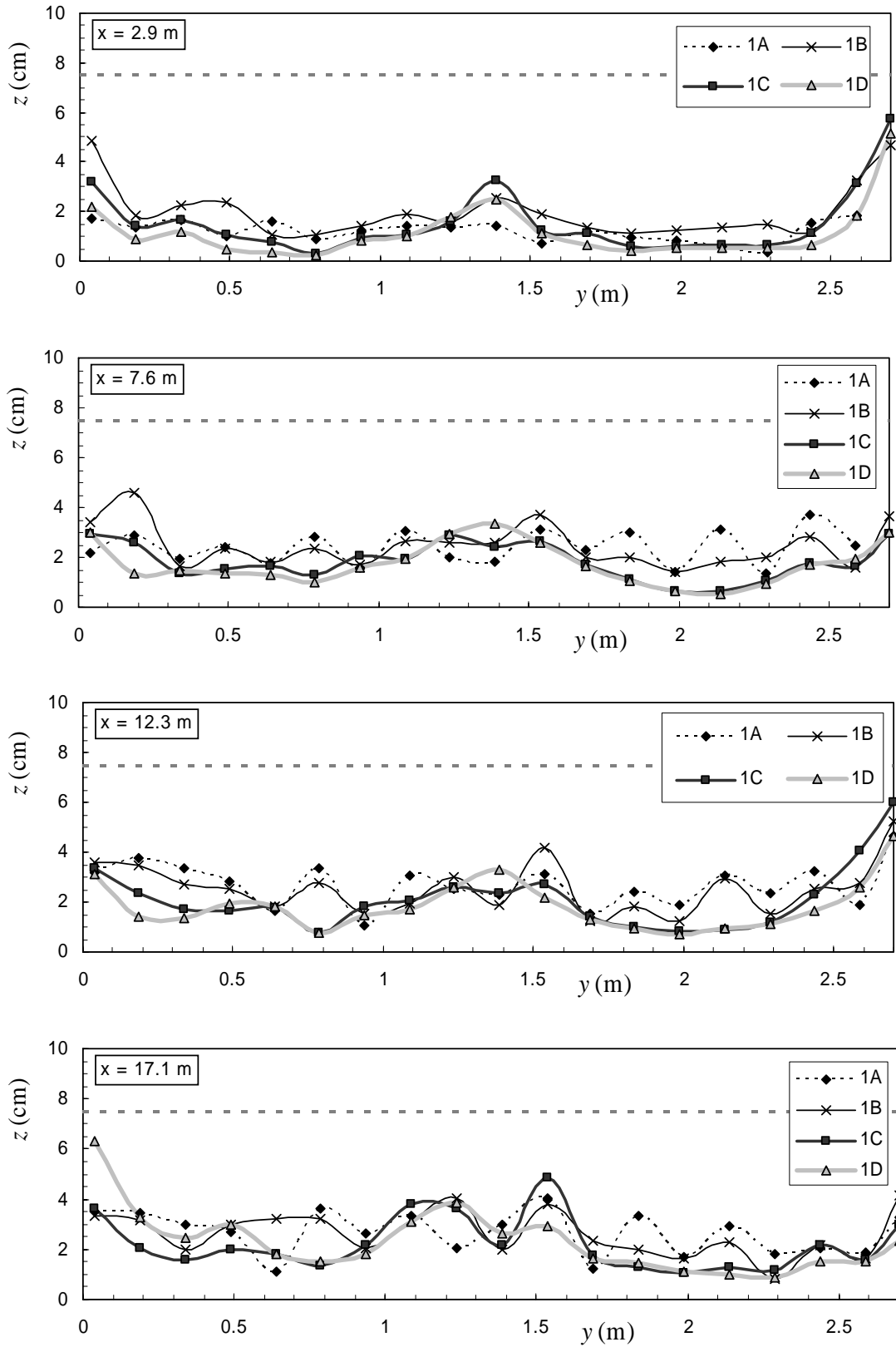


Figure F1. Profile of bed topography, Run 1.

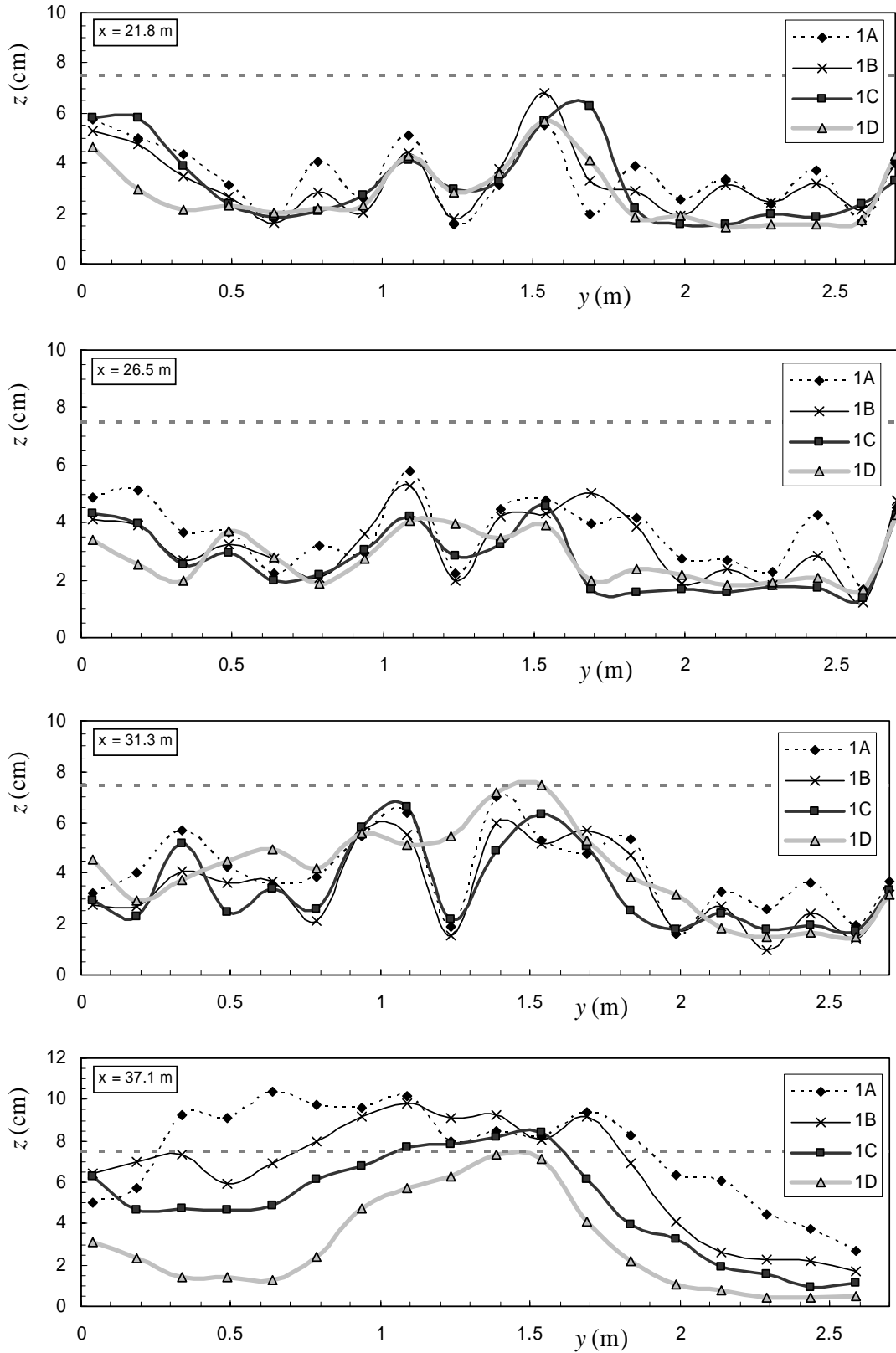


Figure F1 (continued). Profile of bed topography, Run 1.

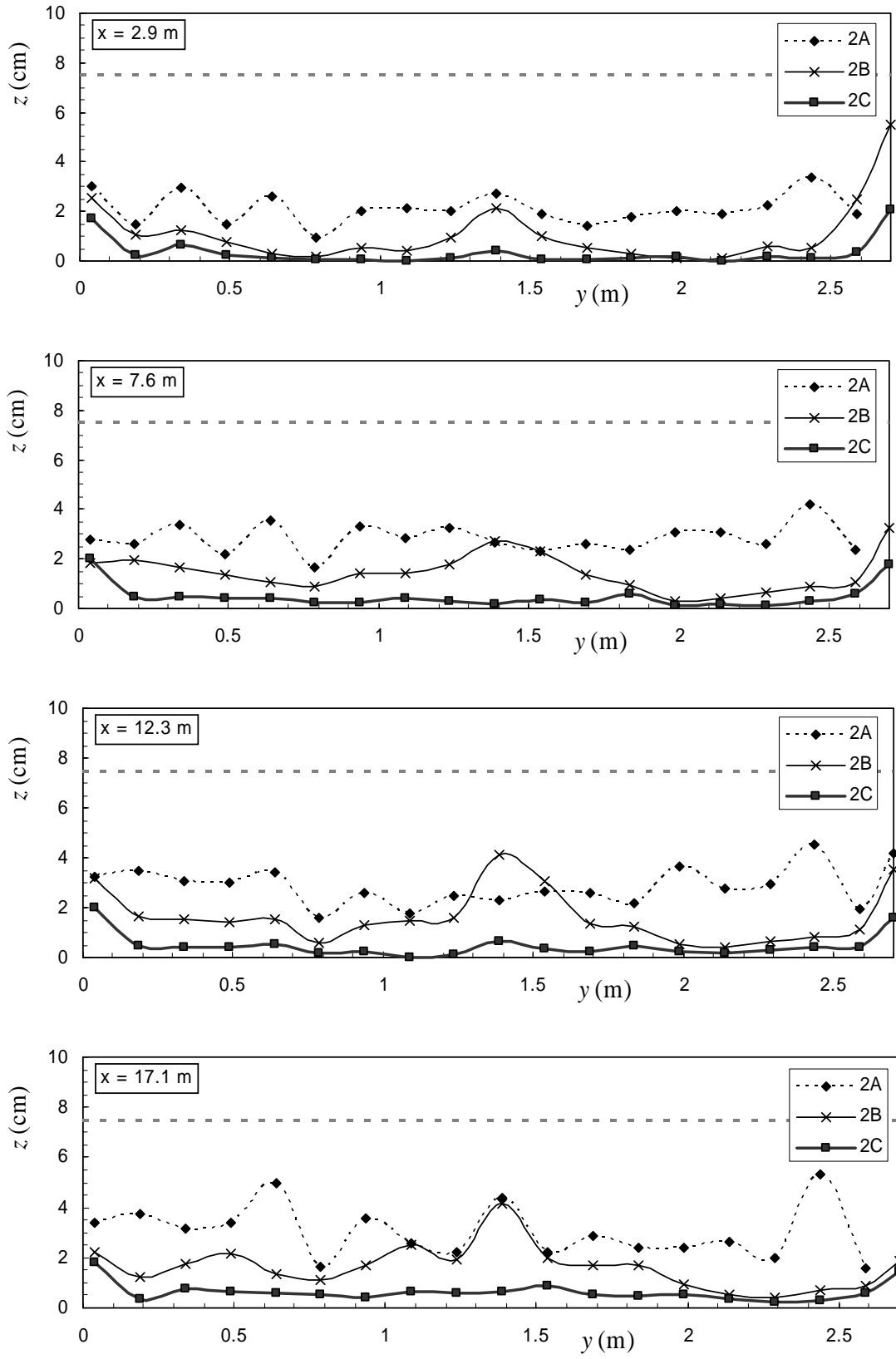


Figure F2. Profile of bed topography, Run 2.

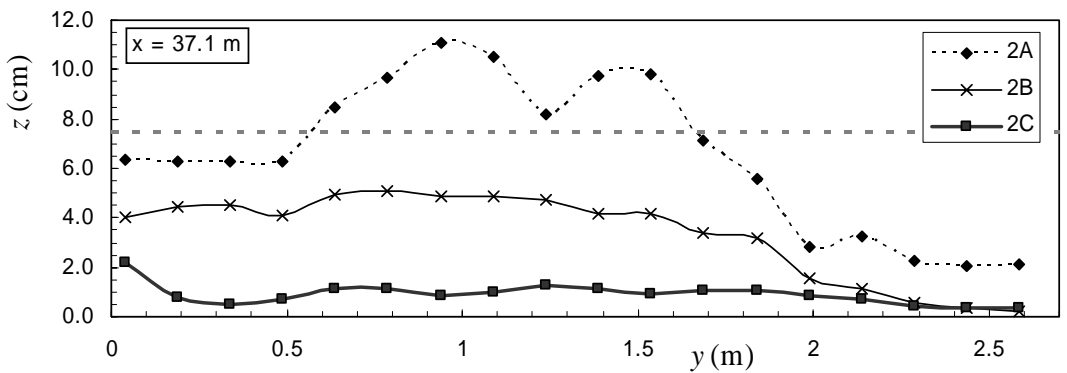
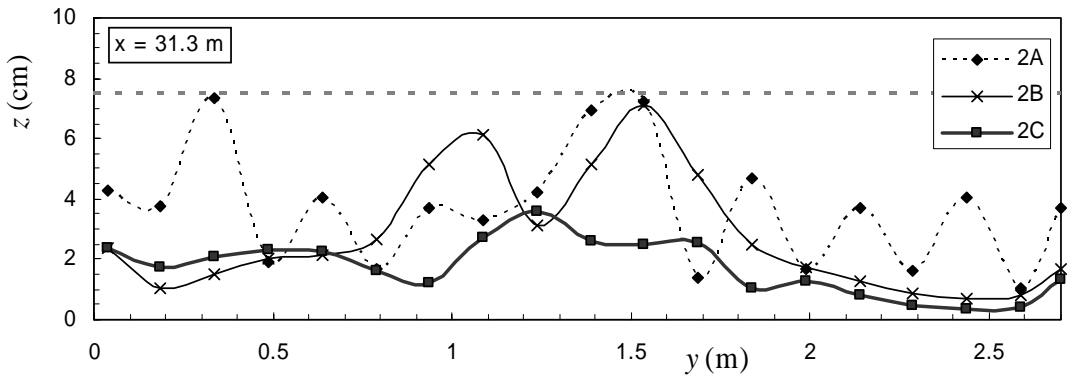
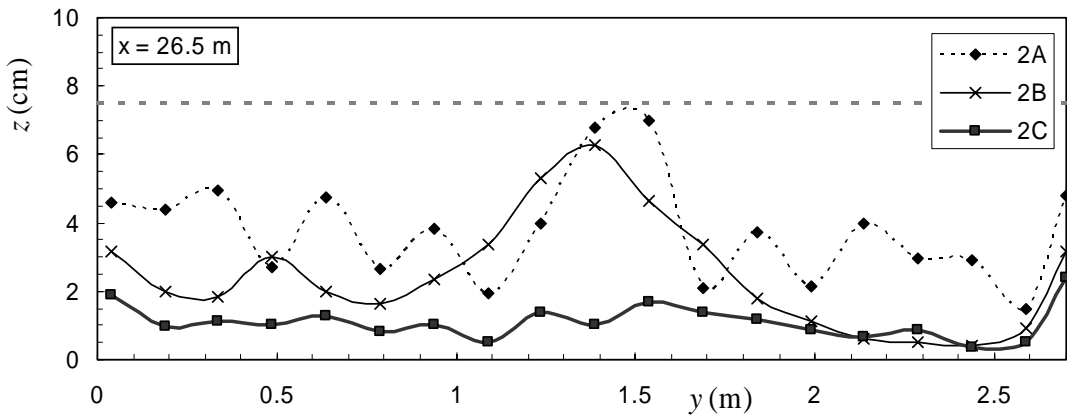
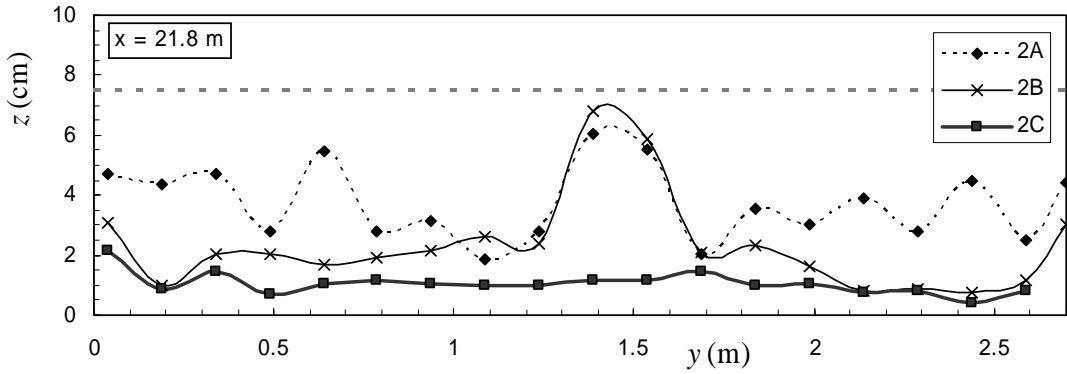


Figure F2 (continued). Profile of bed topography, Run 2.

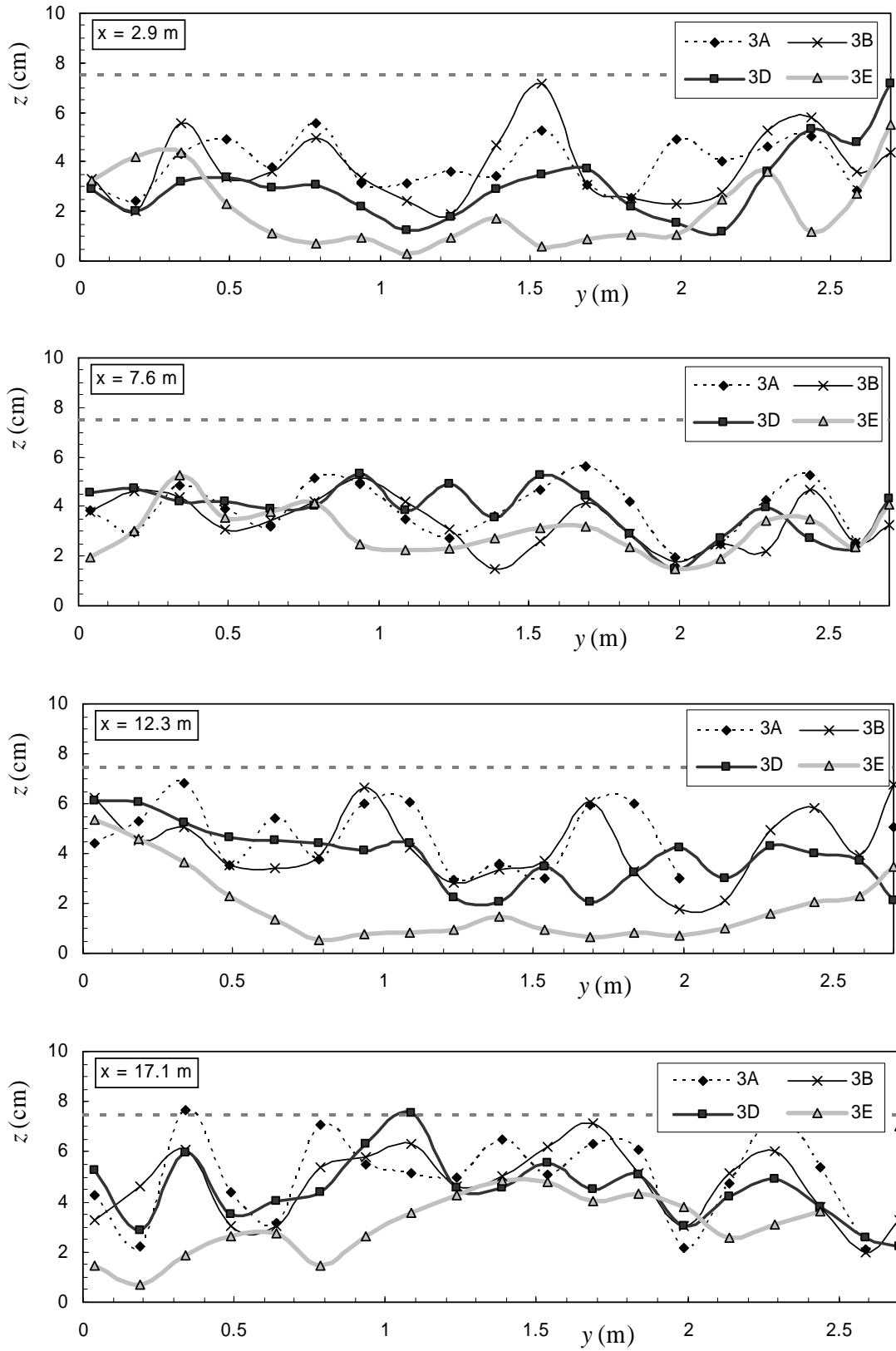


Figure F3. Profile of bed topography, Run 3.

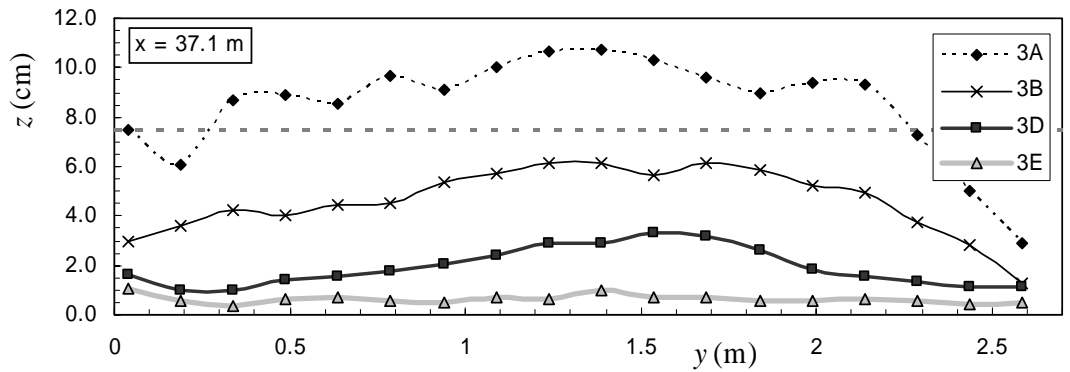
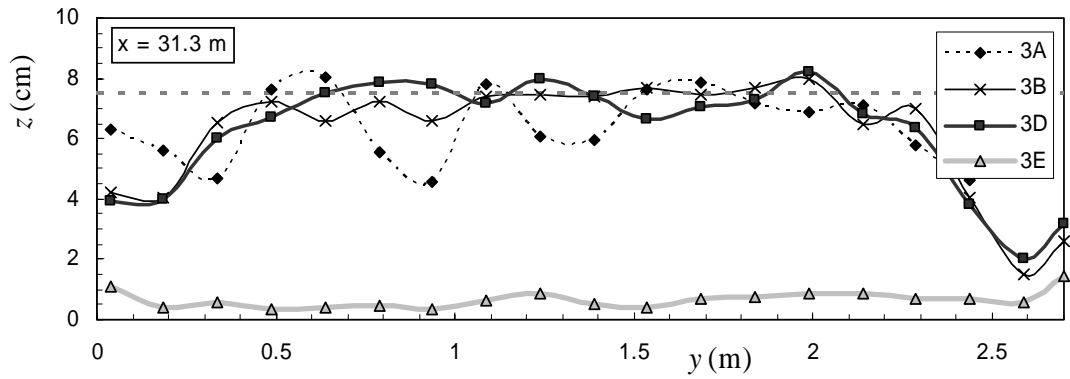
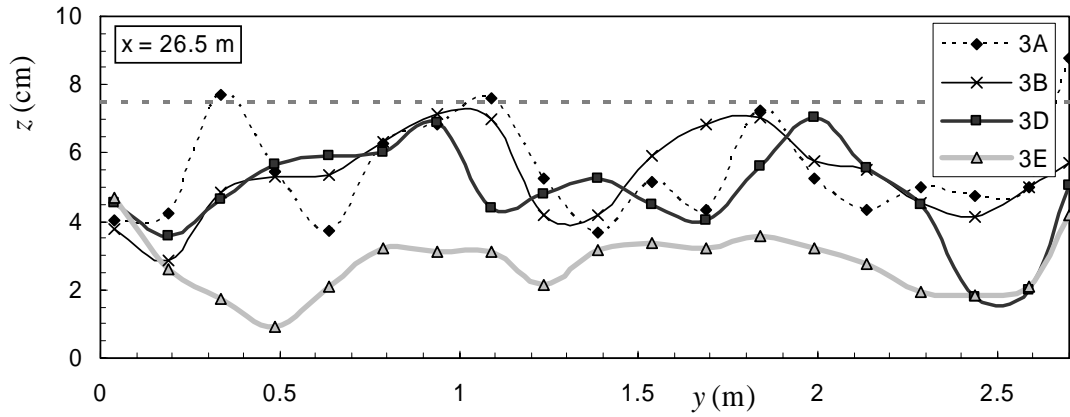
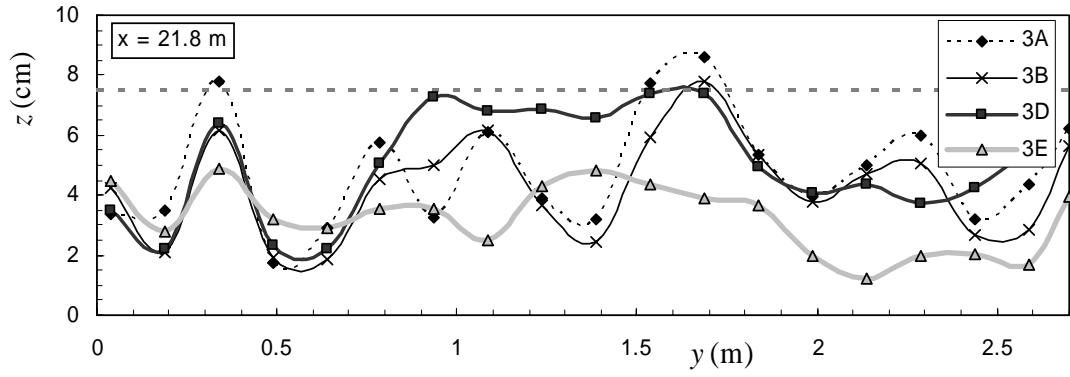


Figure F3 (continued). Profile of bed topography, Run 3.

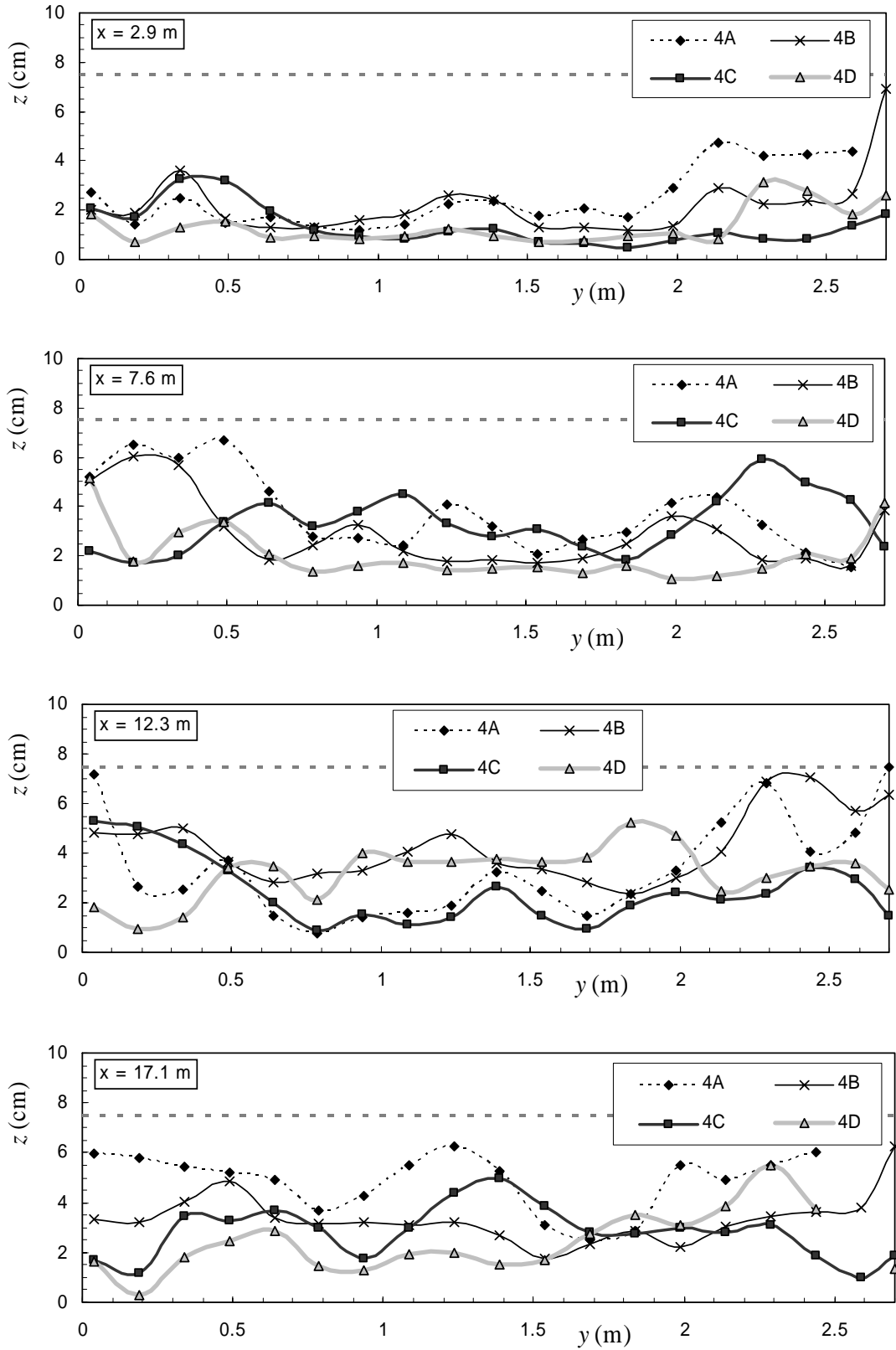


Figure F4. Profile of bed topography, Run 4.

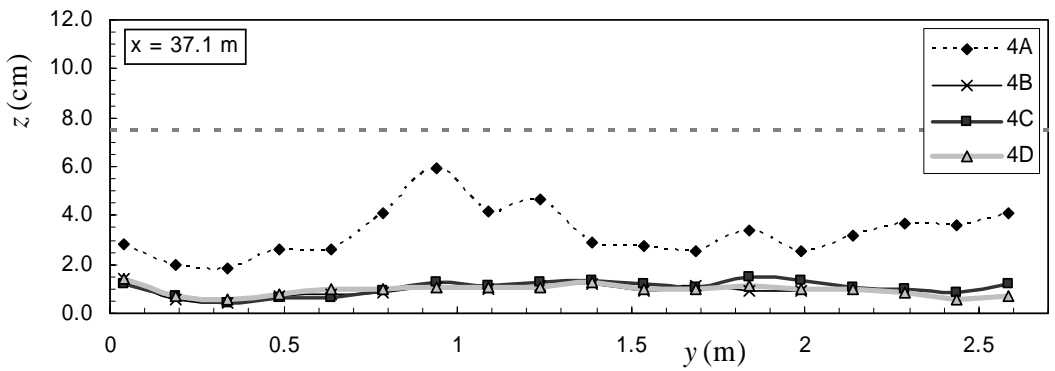
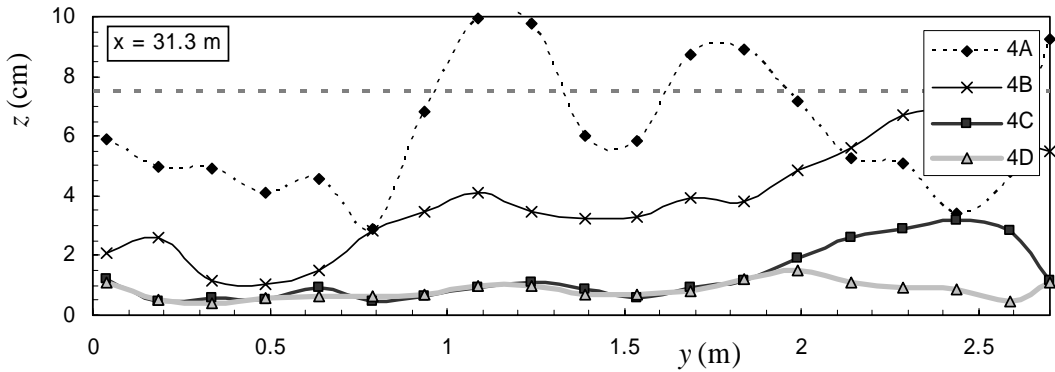
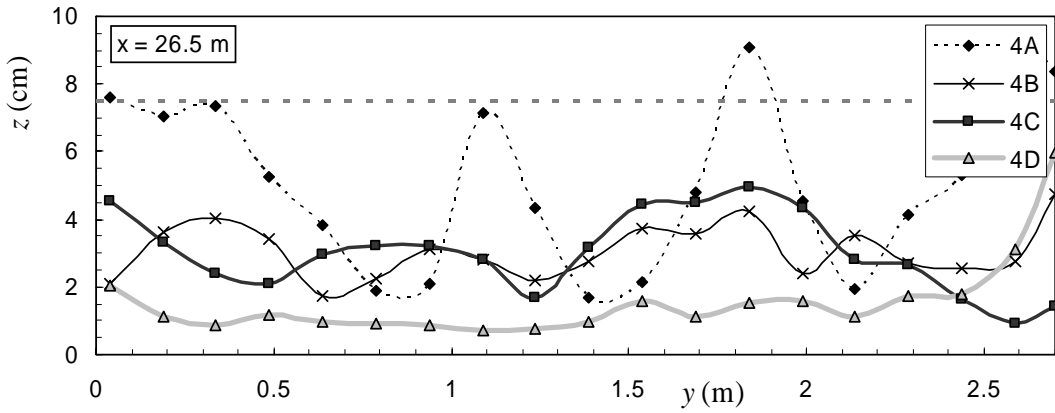
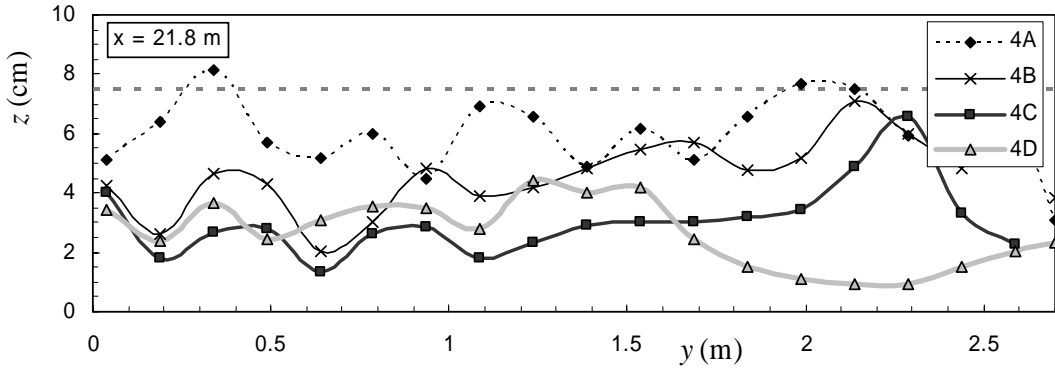


Figure F4 (continued). Profile of bed topography, Run 4.

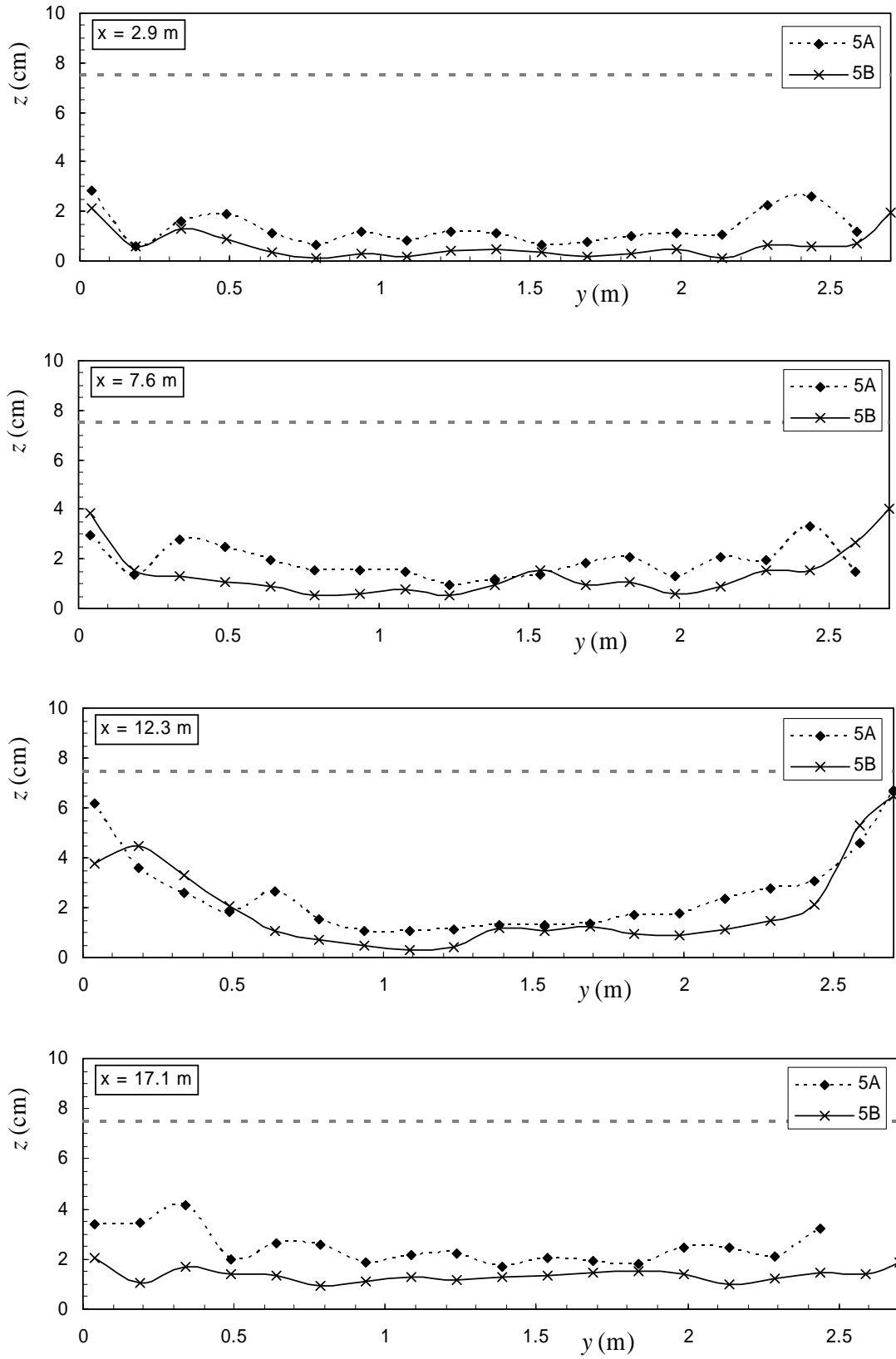


Figure F5. Profile of bed topography, Run 5.

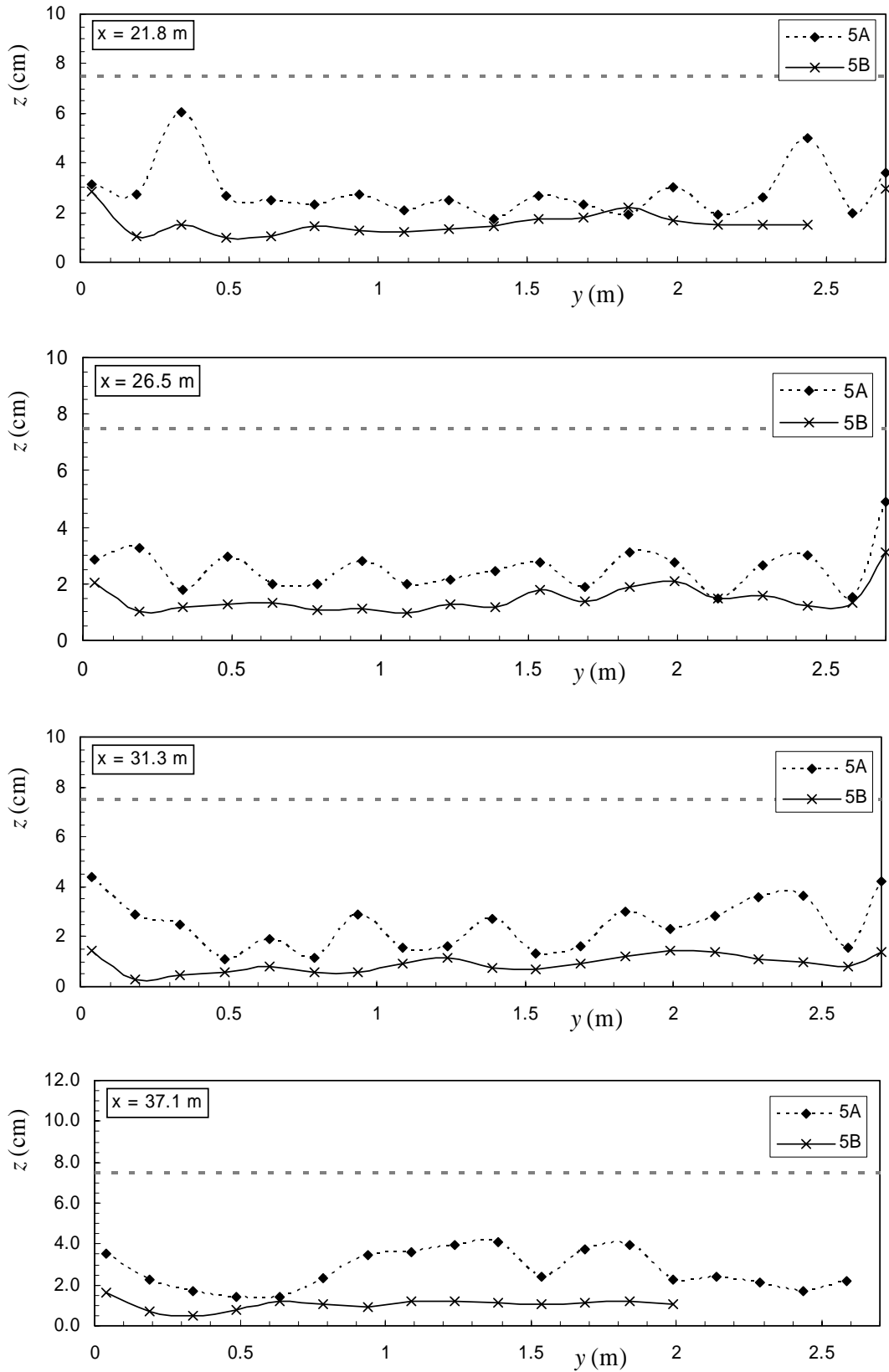


Figure F5 (continued). Profile of bed topography, Run 5.

VITA

Name: Paul Edward Grams

Born: January 16, 1968
Minnetonka, Minnesota

Education: Hopkins High School, 1986
Minnetonka, Minnesota

B.A., Geology, 1991
Middlebury College
Middlebury, Vermont

M.S., Geology, 1997
Utah State University
Logan, Utah

Ph.D., Geography and Environmental Engineering, 2005
The Johns Hopkins University
Baltimore, Maryland